Stony Brook University

Quantum Effects in Condensed Matter Systems in Three, Two, and One Dimensions

A Dissertation Presented

by

Sriram Ganeshan

to

The Graduate School

in Partial Fulfillment of the Requirements

for the Degree of

Doctor of Philosophy

in

Physics

Stony Brook University

August 2012

Stony Brook University

The Graduate School

Sriram Ganeshan

We, the dissertation committee for the above candidate for the Doctor of Philosophy degree, hereby recommend acceptance of this dissertation.

Maria Victoria Fernández-Serra – Dissertation Advisor
Assistant Professor, Department of Physics and Astronomy

Adam C. Durst- – Co-Advisor
Doctor, Photon Research Associates Inc.

Dominik Schneble – Chairperson of Defense
Associate Professor, Department of Physics and Astronomy

Philip B. Allen – Committee Member
Professor, Department of Physics and Astronomy

José M. Soler Torroja – Outside Member
Professor, Department Física de la Materia Condensada
Universidad Autónoma de Madrid.

This dissertation is accepted by the Graduate School.

Charles Taber
Interim Dean of the Graduate School

Abstract of the Dissertation

Quantum Effects in Condensed Matter Systems in Three, Two, and One Dimensions

by

Sriram Ganeshan

Doctor of Philosophy

in

Physics

Stony Brook University

2012

The quantum nature of matter not only results in exotic properties of strongly correlated condensed matter systems, but is also responsible for remarkable properties of ubiquitous systems like water. In this thesis, we study the role of quantum effects in diverse condensed matter systems. In the first part of the thesis, we develop a computationally inexpensive alternative method to the path integral (PI) formalism that is capable of including vibrational zero-point quantum effects in classical molecular dynamics (MD) simulations. Our idea is based on the concept of thermostats, used for temperature control in MD. We combine Nose-Hoover (NH) and Generalized Langevin thermostats (GLE) to equilibrate different dynamical modes to their zero point temperature. We applied our thermostat (NGLE) to a flexible liquid water force field, and structural properties are in good agreement with PIMD with frac-

tion of its computation time. Our NGLE is simple and involves much less parameters to optimize than in standard GLE without NH. We also used NGLE to gain deeper insight into the structure of water by probing how different modes are correlated to one another.

In the second part of the thesis, we study how quantum interference affects transport in vortex state of d-wave superconductors. The order parameter (gap) in high-Tc cuprate superconductors exhibits d-wave symmetry. Near each of four gap nodes, quasiparticles behave like massless relativistic particles. In this work, we consider low-temperature thermal transport in the 2D cuprate plane, and we study the scattering of these quasiparticles from magnetic vortices. We calculate the exact differential scattering cross section of massless Dirac quasiparticles scattered due to the regularized Berry phase effect of vortices, and we show that it is the dominant scattering contribution in the longitudinal transport.

Next, we considered quantum interferometers made of 1D edge states of Fractional Quantum Hall (FQH) System. FQH states exhibit some of the most striking effects of strong electronic correlations. These correlations also lead to a novel dynamics at the edges of FQH systems, modeled by 1D chiral Luttinger liquid which is the conformal field theory of free chiral Bosons. Tunneling is modeled by sum of two Boundary Sine-Gordon terms. In this work, we show that by properly including compactness of chiral Bosons in path integral, we can construct a local theory of two point tunneling that can describe both weak and strong (quasiparticle) tunneling regimes. Our work also provides formal insight into how compactness influences chiral Boson propagators.

To my family.

Contents

List of Figures

List of Tables

Acknowledgements

First and foremost I would like to express my greatest gratitude to my thesis advisor Dr. Marivi Fernández-Serra. I would write further, with the knowledge that in this acknowledgment I would not be able to do justice to Marivi's contribution to my career. I am fortunate to have her as my mentor due to many reasons.

She agreed to supervise and fund me at a very important transition phase of my PhD. She worked hard to educate me knowing that I lacked the necessary background or knowledge to work in computational physics. I appreciate her efforts to go out of her way to accommodate my interests while choosing a project. The best part of my interaction with her was the freedom to voice my rubbish ideas. She would correct me in a way that would educate me rather than embarrass me. She even encouraged my crazy idea to write a full fledged molecular dynamics code in Mathematica. Eventually I ended up learning all the nuts and bolts of MD and most importantly why it is not such a good idea to do it in Mathematica. It is solely her contribution that my ideas have become somewhat less ridiculous. My fragilities in computational physics are due to my own ignorance.

Besides being a very good scientist and an amazing mentor, she is the most humble and excellent human being. She supported my pursuit to gain experience in different areas of condensed matter theory. Her encouragement and freedom to complete my pending projects at the time I joined her resulted in two publications that turned out to be important for my career. Although some part of this thesis is not based on the work with her, but 'literally' no part of this thesis would have been possible without her support. Marivi has set a very high standard in her role as a mentor. It would be a challenge for

me to emulate her, if and when I get an opportunity to mentor my students.

Besides my advisor I am fortunate to have worked closely with Prof. A. G. Abanov. There has not been a single instance when I would go to his office to discuss and he would not receive me. There had been times when we would discuss for 3-4 hours every day. I have always been at least two (or more) steps behind him and he would be really patient with me. He has never treated me any different from his own graduate students. I sincerely thank him for this opportunity to work with him. I have benefitted a lot from his guidance and because of him I am less intimidated by theoretical physics.

I would also like to thank my first advisor Dr. Adam Durst. It was a real pleasure to work with him. He made sure that my transition was smooth when he left Stony Brook. I appreciate his efforts to help me publish the work that I started with him. I will always have high regards for him.

I thank all the eminent faculty members from whom I took courses. Many courses directly benefitted my research and the classroom time was a joyful experience. I thank Professors Peter van Nieuwenhuizen, Barry McCoy, Robert Shrock, Alexander Abanov, Ismail Zahed and K. K. Likharev. I have also enjoyed numerous fruitful discussions with Prof. D. Averin. I thank Dr. Nikolai Sinitsyn for the opportunity to collaborate with him at Los Alamos National Lab through July 2011. I also thank Pat Peiliker and Pernille Jensen for making sure that I got my paychecks on time. I thank Prof. R. Rajaraman, Deepak Kumar and Shankar P. Das for motivating me towards theoretical research while I was in JNU (India).

I thank my fellow group members Betül Pamuk, Luana Pedroza and Adrien Poissier for their help with my computer inefficacy, numerous discussions and most importantly their company which made my work place enjoyable. I sincerely thank my friends Chee Sheng Fong, Manas Kulkarni, Marija Kotur, Prerit Jaiswal, Michael Assis and Heli Vora for their company. I am fortunate to have known them and they would be friends for life.

This section would be incomplete without mentioning the most important people in my life. My late mother Lakshmi has been the chief architect of who I am today. It was her will and passion to see us well educated that developed my interest towards studies. I still remember her enthusiasm to prepare us for

exams as if her whole life depended on it. Although she passed away when I was 11, I subconsciously retained her ambition and drive towards education. I am sure she would have been really happy and proud to read this. My father Ganeshan made lot of sacrifices to provide us with a stable environment to study. He turned down many opportunities to grow in his career so that I was not displaced. I will always be indebted to him for what he has done for me. I thank him for staying close to me despite our physical distance. I cannot end this section without mentioning my beloved uncle Chandrasekaran who has been with me since I was 2 years old. After my mother, he really took good care of all of us. His constant positive words of encouragement lifted me when I was down. His words made me believe in myself. I can say for sure that because of him I have a 'never say die attitude' in my life. I am grateful to my aunt Swathantra for being with me for months during my preparation for important public exams that eventually helped me get admission in good undergraduate college. I would also like to thank my grandpa Subramanian for his love and care. I also thank my brother Suresh for his financial and moral support in the time of need. I am really fortunate to have been part of family with such wonderful selfless people.

Last but not the least, I thank Divya for standing by me, my passion, my goals and bearing with all the uncertainties associated with my career. She has kept me going through all the ups and downs not only in my PhD but since my undergraduate days. No matter what (or however incorrect) she believes that I am the 'best'. I simply believe her!

Publications

This thesis is mainly based on the following publications:

1. Sriram Ganeshan, M. Kulkarni, and Adam C. Durst, "Quasiparticle scattering from vortices in d-wave superconductors. II. Berry phase contribution" Phys. Rev. B 84, 064503 (2011)

2. M. Kulkarni, Sriram Ganeshan, and Adam C. Durst, "Quasiparticle scattering from vortices in d-wave superconductors. I. Superflow contribution" Phys. Rev. B 84, 064502 (2011)

3. Sriram Ganeshan and N. A. Sinitsyn, " Fluctuation Relations for Current Components in mesoscopic Electric Circuits" Phys. Rev. B 84, 245405 (2011)

4. Adrien Poissier, Sriram Ganeshan, and M. V. Fernandez-Serra, "The role of hydrogen bonding in water-metal interactions" Phys. Chem. Chem. Phys., 3375-3384 (2011).

5. Sriram Ganeshan, R. Ramirez, M. V. Fernandez-Serra "Quantum zero point effects using modified Nose-Hoover thermostats" arXiv:1208.1928v1, To be submitted in JCP.

Additional work completed in the duration of the author's PhD career:

1. Sriram Ganeshan, Alexander G. Abanov, Dmitri V. Averin " Compact chiral bosons and strong tunneling behavior of FQH interferometer" To be submitted in PRL.

Chapter 1

Introduction

1.1 Quantum effects in condensed matter systems

The advent of quantum mechanics in the early 20th century has revolutionized the way we understand matter. One of the main successes of quantum physics was the explanation of microscopic properties of matter. By the first half of the 20th century, quantum physics provided a firm foundation towards understanding "conventional solid state" and "soft matter" systems. Most of the new physics (such as diamagnetism, low temperature specific heat) was built on the quantum nature of independent particles (electrons) subjected to the Pauli exclusion principle. Amazingly, the quantum mechanical treatment of electrons even at the crude level (ignoring Coulomb interactions) resulted in the successful explanation of many previously puzzling problems. The discovery of superconductivity by Kamerlingh Onnes was the first instance where properties of many-electron systems differed drastically from their individual constituents. The discovery of subtle collective effect responsible for superconductivity had to wait for development of field theoretical methods. With the success of BCS theory (Bardeen, Cooper, Schrieffer 1957), the second half of the 20th century saw a new paradigm in the form of Condensed Matter (CM) that metamorphosed into a branch of physics in itself. CM is the study of the physical properties of many-particle systems under the influence of pre-

sumably known interactions. In many instances, a quantum description at the atomic or molecular scale can be formulated based on the independent-electron approximation with a mean field treatment of interactions (such as in Density Functional Theory). In this sense, a distinction is made between quantum condensed-matter systems that can be studied within the mean field approximation (weakly correlated) and strongly correlated systems for which a mean field description may or may not exist. Many properties of weakly correlated systems (such as phase transitions) can in general already be understood by effective classical models. However, an exception being low temperature phase transitions like the order-disorder transition in hexagonal ice ($\rightarrow$ ice XI). The reason why a classical description works in some cases is the existence of (broken) symmetries and conservation laws which are independent of the underlying classical or quantum nature of the system. In the case of water, a classical description looks sufficient, but it turns out that quantum mechanics plays a vital role in determining many of its microscopic and macroscopic properties. In this thesis we study quantum effects in diverse condensed matter systems. The manifestation of Quantum effects is completely different in all these systems. The first chapter of this thesis deals with how quantum zero point (QZP) effects determine the microscopic structure of liquid water at room temperature. In the second and third chapter of this thesis we study quantum interference effects in strongly correlated electron systems like cuprate superconductors and quantum Hall state.

1.2 Quantum effects in 3-D: Liquid water

Molecules like water have vibrational modes with zero point energy well above room temperature. As a consequence, classical molecular dynamics simulations of their liquids largely underestimate the kinetic energy of the ions, which translates into an underestimation of covalent interatomic distances. Zero point effects can be recovered using path integral molecular dynamics simulations, but these are computationally expensive, making their combination with ab initio molecular dynamics simulations a challenge. As an alternative to path integral methods, from a computationally simple perspec-

tive, one would envision the design of a thermostat capable of equilibrating and maintaining the different vibrational modes at their corresponding zero point temperatures. Recently, Ceriotti et al. [Phys. Rev. Lett. 102, 020601 (2009)] introduced a framework to use a custom-tailored Langevin equation with correlated-noise that can be used to include quantum fluctuations in classical molecular-dynamics simulations. The parameters when tailored appropriately allow the effective simulation of nuclear quantum effects through a purely classical dynamics. One of the interesting applications of these thermostats is that, such a framework can be used to selectively damp normal modes whose frequency falls within a prescribed, narrow range using GLE with delta-like memory kernels [2]. In this work we use a modified delta-like memory kernel that samples canonical distribution and apply it in combination with Nose-Hoover(NH) [3, 4] thermostat. We call it Nose GLE thermostating scheme or NGLE. We apply NGLE to a flexible force field model [5](q-TIP4P/F), a model that is explicitly fitted with the lack of zero- point ionic vibrations. In this work we show that it is possible to use the generalized Langevin equation (non-Markovian dynamics) with suppressed noise in combination with NH thermostats to achieve an efficient zero-point temperature of independent modes. We address the question of whether thermostating each mode to its zero point temperature is enough to simulate nuclear quantum effects in water. We use the NGLE thermostating scheme with GLE strongly coupled to the intermolecular modes and almost no coupling to the intramolecular modes. We set the GLE temperature (enforced by generalized fluctuation dissipation relation) very low compared to high NH temperature. Our method is a powerful tool to understand the quantum mechanical role of each mode towards the overall structure of liquid water. The structure of liquid water obtained using NGLE is in good agreement with PIMD (Path Integral Molecular Dynamics) simulations. We also provide detailed analysis of the dynamical properties of modes at their zero-point temperature using mode-decomposed spectral density and clearly demonstrate the competing quantum effects or the competing anharmonicities that govern the structural and dynamical properties of liquid water.

1.3 Quantum effects in 2-D: d-wave superconductors

In this work we consider quantum interference effects in a strongly correlated electron system. My research in this field is focused towards understanding the low energy excitation of cuprates (YBCO) in the overdoped regime. Experiments [6] have now established that the order parameter (gap) in the high-Tc cuprate superconductors exhibits d-wave symmetry, vanishing at four nodal points on the Fermi surface. Near each of these four gap nodes, quasiparticles are easily excited and behave more like massless relativistic particles than electrons in a metal. The thermal Hall conductivity provides the most direct measure of low temperature quasiparticle transport in a $d-wave$ superconductor. In the vortex state, low-temperature transport properties, such as the longitudinal thermal conductivity and the thermal Hall conductivity [7, 8], can be explained by studying the scattering of these quasiparticles from magnetic vortices.

The massless relativistic quasiparticles satisfy Bogoliubov de-Gennes (BdG) equations. Within the linearized approximation, the BdG equation reduces to a massless Dirac equation in 2+1 D. Dirac quasiparticles are scattered from magnetic vortices via a combination of two basic mechanisms: effective potential scattering due to the superflow swirling about the vortices, and Aharonov-Bohm scattering due to the Berry phase acquired by a quasiparticle upon circling a vortex. We perform a singular-gauge transformation that encodes the Berry phase effect in the form of an antiperiodic boundary condition on the wave function spinor. This is the key for isolating these two scattering contributions. We consider the Berry phase contribution (without superflow), which results in branch cuts between neighboring vortices across which the quasiparticle wave function changes sign. Here, the simplest problem that captures the physics is that of scattering from a single finite branch cut that stretches between two vortices. Elliptical coordinates are natural for this two-center problem and we proceed by separating the massless Dirac equation in elliptical coordinates. The separated second order equations take the form of the (little

known) Whittaker-Hill equations (WHE), which we solve to obtain radial and angular eigenfunctions. Working within this non-trivial elliptical geometry, we constructed exact formulae for the differential scattering cross section due to the Berry phase. This enables us to directly compare the Berry phase and superflow transport cross sections. Our results shows that the Berry phase effect dominates the scattering process for the strong magnetic field and low temperature regime. This is an important result in the context of quasiparticle transport physics, as it clearly quantifies the effect of two different mechanisms in an analytically exact framework. Our work not only helps understanding the Berry phase and the superflow effect on quasiparticle scattering but also provides a general framework to solve relativistic scattering problems (like two center scatterers) in elliptical coordinate systems. The mathematics of scattering involving WHE was developed originally in this work. For example, an exact relativistic plane wave expansion form in terms of the eigenfunctions of WHE was discovered and solutions in the asymptotic limit for the full wave function were also written for the first time.

1.4 Quantum effects in 1-D: Fractional Quantum Hall Edge

In this work our fundamental motivation is the physics of the fractional quantum Hall (FQH) states, which exhibit some of the most striking effects of strong electronic correlations. These are perhaps most evident in the unusual fractionally charged FQH quasiparticles that obey fractional statistics. These correlations also lead to a novel dynamics at the edges of FQH systems which is that of one dimensional chiral Luttinger liquids(χLL). My goal in this project was to describe and analyze a device, the two point-contact interferometer, between two FQH droplets of arbitrary filling factors ν_1 and ν_2, in both weak and strong tunneling regimes. Interferometers can be classified in two categories based on their geometry, 1) Mach Zehnder interferometer (MZI)-When the tunneling occurs between the edges of same chirality. 2) Fabry-Perot interferometer (FPI)- When the tunneling occurs between the edges of two different droplets of opposite chirality. Through rotation of fields, we have managed to

unify the action of both interferometer geometries for arbitrary filling factors with single parameter a ($a = \pm(\nu_1 \pm \nu_2)/(\nu_1+\nu_2)$ for FPI and $a = \pm 1$ for MZI). Sign of the parameter a represents the direction of propagation with $a = 0$ being the non-chiral case. The point contact tunneling for the intereferometer is described by sum of two boundary Sine-Gordon terms. Bosonic fields are free everywhere except at the point of tunneling. We proceed by integrating out free part of the fields except at points of tunneling and obtain two point Caldeira-Leggett (CL) action. $a = 0$ is the simplest case of FPI when the field theory of two counterpropagating chiral fields of same filling factors can be reduced to effective non-chiral bosonic field theory. This case has been studied for both weak and strong tunneling regimes [9]. For different filling factors ($a \neq 0$), the two-point CL action has non-local terms in the different point correlators. In the strong tunneling regime this issue manifests itself into non-causal and chirality violating currents for the non-perturbative instanton calculation. In strong tunneling regime this is the result of an ambiguity in the inverse of Green's function with non-local terms. Thus, it is important that this ambiguity be taken care of before taking the strong tunneling limit. In this work we show that by taking compactness of chiral bosons in path integral formalism, we can resolve this ambiguity and get physical results in the strong tunneling regime. Compactness plays a vital role in non-chiral field theory and is an important component of Kosterlitz-Thouless transition (see Ref. ([10])). We give general expressions for currents in both weak and strong tunneling limits for general interferometer geometries. We obtain electron periodicity with adiabatic variations of flux in both weak and strong tunneling limits.

1.5 Additional project I: Fluctuation theorems in mesoscopic systems far from equilibrium

Transport in the quantum regime is inherently probabilistic. Hence non-thermal current fluctuations contain information about the nature of the underlying transport mechanism. However, the complete information on the

statistics of transport can only be obtained from all correlators of the current. This was noted by Levitov and Lesovik [11] who obtained the famous determinant formula for the generating function for non interacting systems, and coined the term full counting statistics (FCS). FCS is therefore of fundamental interest, which can be used to calculate non-equilibrium particle transfer statistics in terms of a generating function. From the symmetries and analytical properties of generating function one can extract universal laws in non-equilibrium systems also known as '*fluctuation theorems*'. In application to electric circuits, fluctuation theorems predict that the probability distribution P[q] of observing a charge q passed between two lead contacts with a voltage difference V satisfies the law: $P[q]/P[-q] = e^{Fq},\ F = V/k_BT$. Surprisingly, recent experimental work [12] has shown that the FTs can fail in an electric circuit, but could be salvaged under the experimental conditions of Ref. ([12]) if the parameter F is suitably renormalized by a factor 10^{-1}. Motivated by this new experimental result we discovered new class of fluctuation relations called *Fluctuation Relations for Current Components*(FRCCs) [13]. Unlike standard fluctuation theorems, FRCCs were discovered by us from the seemingly trivial fact that to know statistics of particle currents, it is sufficient to know only statistics of single particle geometric trajectories while the information about time moments, at which particles make transitions along such trajectories, is irrelevant. FRCCs have a similar structure as standard FTs but the parameter F is a function of system parameters. In spite of this, we show that FRCCs are universal in the sense that they do not depend on some basic types of electron interactions and importantly are robust against quantum coherence effects.

1.6 Additional project II: Electrostatic interaction between a water molecule and an ideal metal surface

In this work [14] we studied the hydrogen bond interaction between water molecules adsorbed on a $Pd - \langle 111 \rangle$ surface, a nucleator of two dimensional ordered water arrays at low temperatures, using density functional theory

calculations. We analyzed the role of the exchange and correlation density functional in the characterization of both the hydrogen bond and the water-metal interaction. We found that the choice of this potential is critical in determining the cohesive energy of water-metal complexes. We show that the interaction between water molecules and the metal surface is as sensitive to the density functional choice as hydrogen bonds between water molecules are. The reason for this is that the two interactions are very similar in nature. We make a detailed analogy between the water-water bond in the water dimer and the water-Pd bond at the $Pd - \langle 111 \rangle$ surface. Our results show a strong similarity between these two interactions and based on this we describe the water-Pd bond as a hydrogen bond type interaction.

My main contribution to this work was to analytically calculate the electrostatic energy between the water molecule and metal surface using full charge distribution deduced from the wave function obtained from Density Functional Theory (DFT) using SIESTA. We also compute this electrostatic energy as a function of the orientation of the single water molecule, with respect to the metal plane using method of images. We were able to identify vertical alignment (with Hydrogen atoms facing up) as the most stable configuration of the water molecule under the constraint of electrostatic interactions with the metal surface. We also have shown that the full charge distribution provides a much more complex interaction energy landscape as compared to the point charge model, where the lone pairs of the oxygen contribute to minimize the interaction energy for an intermediate alignment.

Chapter 2

Quantum effects in 3-D: Liquid water

2.1 Introduction

Understanding how large are zero point nuclear quantum effects (NQE) both in water[5, 15–17] and ice [18] is an active area of research. How much the structure of liquid water is dependent on the classical treatment of the ionic degrees of freedom in *ab initio* molecular dynamics (MD) simulations is an open question[16, 19]. Even if a number of path integral molecular dynamics studies have addressed the issue [5, 15–17, 19], a definite answer has not yet been provided. The problem is subtle, due to the complex nature [20] of the OH–O hydrogen bond (Hbond) in water. It is well known that hydrogen bonded materials show an anti-correlation [21] between the high energy, stretching frequencies and the librational frequencies of the molecules. Recently [18], we have shown that this anti-correlation is the origin of negative grüneisen parameters of the high energy vibrational modes in ice. These are large enough to cause an anomalous isotope effect in the volume of ice, making the volume per molecule of heavy or D_2O ice larger than that of normal or H_2O ice. This anomaly is not captured by flexible and/or polarizable force-fields, due to their underestimation of the anti-correlation effect [18]. Nonetheless, we choose to use in this study the q-TIP4P/F [5] force field. Even if it has

been shown to fail in the description of the anomalous isotope effect of ice [18], it provides a good qualitative description of the anharmonicities of all the modes in liquid water. In classical MD simulations of force field models, all the modes are equilibrated at a given constant temperature. This equipartition of temperature is a classical description of liquid water which lacks NQE. Recently, Ceriotti *et al.*[2, 22–26] have shown that the key features of path integral molecular dynamics (PIMD) simulations of liquid water can be reproduced using custom tailored thermostats based on generalized Langevin dynamics (GLE). In their work, they were able to enforce the ω-dependent effective temperature $T(\omega) = \frac{\hbar\omega}{2k_B} \coth \frac{\hbar\omega}{2k_B T}$ simultaneously on different normal modes, without any explicit knowledge of the vibrational spectrum. The tailoring aspect of their thermostat involves complicated optimization to independently tune the drift and diffusion parameters of the GLE dynamics. In this work we introduce a new thermostating scheme with very few, and easy to tune parameters that can equilibrate modes to different temperatures. In our scheme we couple both Nose-Hoover (NH) and GLE dynamics to the system. We use GLE kernels that satisfy the fluctuation-dissipation (FD) condition which can be derived from a well defined harmonic bath model. We suppress the noise term in GLE dynamics by setting the GLE temperature close to 0. In this limit, the dynamics is almost deterministic. The frequency dependent equilibration is achieved through the independent tuning of NH and the frequency dependent friction profile. Microscopic details of the full dynamics are presented in Sec. (2.2.1). We sacrifice transferability of parameters between different systems in exchange for simplicity in their optimization against the known vibrational spectrum of the system. This thermostat acts on the system within a deterministic regime and hence our method can be thought as a deterministic frequency dependent thermostat or phonostat [27]. The goals of this study are two sided. On the methodological side, after rigorously deriving the thermostat equations, we evaluate its performance , by comparing it with PIMD simulations of q-TIP4P/F water. In addition, we address the question of competing quantum effects [5] or competing anharmonicities in water [18] using a quantified, temperature-dependent approach. To achieve this we reformulate the idea of NQE in terms of the zero point energy of individual

modes.

2.2 Nose-Hoover thermostats in presence of GLE kernel

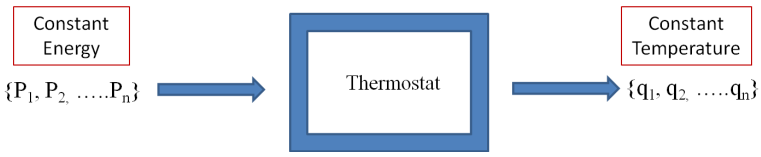

Figure 2.1: Schematic of thermostating in MD simulation

In this work, we construct a new frequency dependent thermostating scheme. This scheme involves use of two thermostats. We use the standard NH chain thermostats which is the gold standard of thermostats. To achieve frequency dependent equilibration, we use GLE to modify the NH action. Recently, Ceriotti and Parinello [2, 22–26] developed an extensive thermostating scheme based on GLE dynamics. We choose a particular form of GLE dynamics and use it in conjunction with the NH dynamics to enforce frequency dependent thermostating. We call this new scheme NGLE (for Nose-GLE) thermostating.

2.2.1 Microscopic derivation of NGLE dynamics

In this section we start with the microscopic model for NGLE thermostat starting from a system-bath coupling model. The full extended Hamiltonian of the system can be written as,

$$H_{total} = H_{sys}(\frac{p_i}{s}, q_i) + H_{NH}(p_s, s) + H_{GLE}(p_{i,x_k}, x_{i,k}) \tag{2.1}$$

Where,

$$H_{sys} = \sum_{i=1}^{3N} \frac{p_i^2}{2M_i s^2} + V(q_1....q_{3N}) \tag{2.2}$$

$$H_{NH} = \frac{p_s^2}{2Q} + (3N+1)k_B T_{NH} \log s$$

$$H_{GLE} = \sum_{i=1}^{3N} H_{GLE}^i \tag{2.3}$$

$$H_{GLE}^i = \sum_{k=1}^{g} \left(\frac{p_{i,x_k}^2}{2m} + \frac{1}{2} m\omega_k^2 \Big(x_{i,k} + \frac{\beta\ q_i}{m\omega_k^2} \Big)^2 \right) \tag{2.4}$$

s is the parameter that modifies the effective dynamics and enforces constant temperature ensemble on the rescaled momenta $(\frac{p}{s})$. Q is the NH mass. This rescaled dynamics is also coupled to a harmonic bath that enforces generalized Langevin dynamics. This is achieved by coupling each system degree of freedom to g harmonic oscillators of mass m and frequency ω_k. β is the coupling strength of the oscillator to the system degree of freedom. p_{i,x_k} is the momentum conjugate to the kth oscillator position $x_{i,k}$ (index i corresponds to the system degree of freedom). Hamilton Jacobi equations for the total dynamics for the system degrees of freedom can be written as,

$$\dot{q}_i = \frac{p_i}{M_i s^2} \tag{2.5}$$

$$\dot{p}_i = -\frac{\partial V(\mathbf{q})}{\partial q_i} - \sum_k \frac{\beta^2}{m\omega_k^2} q_i - \sum_k \beta x_{i,k} \tag{2.6}$$

The dynamics of NH degrees of freedom is given as,

$$\dot{s} = \frac{p_s}{Q}$$

$$\dot{p}_s = \sum_i^{3N} \frac{p_i^2}{M_i s^3} - \frac{(3N+1)k_B T_{NH}}{s} \tag{2.7}$$

We can further simplify NH dynamics in Eq. (2.7) by rescaling time and momenta. We perform $dt \rightarrow \frac{dt}{s}$ in Eq. (2.6). The resulting equations can be written in terms of the rescaled momenta $p_i \rightarrow \frac{p_i}{s}$

$$\begin{aligned} \dot{\eta} &= \frac{p_\eta}{Q} \\ \dot{p}_\eta &= \Big[\sum_i^N \frac{p_i^2}{M_i} - (3N+1)k_B T_{NH}\Big] \end{aligned} \tag{2.8}$$

Where $\eta = \log s$.

The dynamics of GLE bath degrees of freedom is given by.

$$\dot{x}_{i,k} = \frac{p_{i,x_k}}{m_k} \tag{2.9}$$

$$\dot{p}_{i,x_k} = -\beta q_i - m\omega_k^2 x_{i,k} \tag{2.10}$$

The above equations for the GLE bath can be solved exactly and can be substituted in Eq. (2.6). The resulting system's dynamics in presence of NH chains and the GLE bath[28, 29] can be written in the following form,

$$\dot{q}_i = \frac{p_i}{M_i} \tag{2.11}$$

$$\dot{p}_i = -\frac{\partial V}{\partial q_i} - \int_{-\infty}^{t} K(t-t')p_i(t')dt' + \zeta(t) - p_i\frac{p_\eta}{Q} \tag{2.12}$$

where the last term is the NH term that is coupled to the system. The memory kernel $K(t)$ has an exact expression in terms of the bath parameters,

$$K(t) = \sum_k \left(\frac{\beta}{\sqrt{m}\omega_k}\right)^2 \cos(\omega_k t) \tag{2.13}$$

The 'random' force $\zeta(t)$ can also be completely determined in terms of the bath degrees of freedom. $\zeta(t)$ is connected to the memory kernel through the FD theorem as $\langle\zeta(t)\zeta(t')\rangle = k_B T_{GLE}\ K(t-t')$ with $\langle\zeta(t)\rangle = 0$. Note

that the temperature enforced by the FD condition is different from the NH temperature. We can rewrite Eq. (2.12) by absorbing the NH term into the time integral.

$$\dot{p}_i = -\frac{\partial V}{\partial q_i} - \int_{-\infty}^{t} \tilde{K}(t,t')p_i(t')dt' + \sqrt{2M_i k_B T_{GLE}}\tilde{\zeta}(t) \tag{2.14}$$

Where we have defined,

$$\tilde{K}(t,t') = K(t-t') + \delta(t-t')\frac{p_\eta(t')}{Q} \ , \ \langle\tilde{\zeta}(t)\tilde{\zeta}(0)\rangle = K(t) \tag{2.15}$$

Now consider Eq. (2.14) in the case when $T_{GLE} \to 0$,

$$\dot{p}_i = -\frac{\partial V}{\partial q_i} - \int_{-\infty}^{t} \tilde{K}(t,t')p_i(t')dt' \tag{2.16}$$

In this case the noise term is completely suppressed and we have a GLE dynamics that involves only a nonlocal friction profile and the deterministic NH term that provides constant temperature T_{NH} to the system. The conserved energy for this modified dynamics can be written as,

$$H' = H_{sys}(p,q) + \frac{p_\eta^2}{2Q} + (3N+1)k_B T_{NH}\eta + \sum_i \Delta KE_i \tag{2.17}$$

The last term in the above equation is the change in kinetic energy for each GLE action summed over all past trajectories [24, 30]. In this work we achieve frequency dependent equilibration as a result of the competition between the NH dynamics and the damping action of nonlocal friction profile with suppressed noise.

2.2.2 Delta-like memory kernels

The friction term in Eq. (2.12) is linear in the system momentum, and the friction coefficient $K(t)$ is a simple function of the frequencies ω_k and the coupling constants $\frac{\beta}{\sqrt{m}}$. This generalized Langevin equation is exact and its validity is not restricted to small departures from thermal equilibrium. Now we consider the case of infinite number of oscillators with continuous distribution of frequencies ω_k. In this limit the summation in Eq. (2.13) can be replaced by an integral with some distribution function ($\sum \rightarrow N \int d\omega g(\omega)$).

$$K(t) = N \int d\omega \; g(\omega) \left(\frac{\beta}{\sqrt{m}\omega} \right)^2 \cos(\omega \; t) \tag{2.18}$$

Since we have control over the bath degrees of freedom we choose the coupling constant to be, $\frac{\beta}{\sqrt{m}} = \sqrt{\frac{\gamma(\Delta\omega^2+\omega_0^2)}{N}}$. We are free to choose the distribution of frequencies of the oscillators to enforce desired memory kernel on the system. To design delta like memory kernels $K(t)$ introduced in Ref. ([2]), we choose the frequency distribution function of the oscillators to be,

$$g(\omega) = \frac{\omega^2}{\Delta\omega^2 + (\omega - \omega_0)^2} \tag{2.19}$$

The above distribution of the continuum oscillator frequencies results in the effective delta like friction profile of Ref. ([2]) which is the essential component of frequency dependent thermostating scheme. The memory kernel obtained is given by,

$$\begin{aligned} K(\omega) &= \gamma \left(\frac{\Delta\omega^2 + \omega_0^2}{\Delta\omega} \right) \left(\frac{\Delta\omega}{\Delta\omega^2 + (\omega - \omega_0)^2} \right. \\ &+ \left. \frac{\Delta\omega}{\Delta\omega^2 + (\omega + \omega_0)^2} \right) \end{aligned} \tag{2.20}$$

$$K(t) = \gamma \left(\frac{\Delta\omega^2 + \omega_0^2}{\Delta\omega} \right) e^{-|t|\Delta\omega} \cos\omega_0 t \tag{2.21}$$

In the memory kernel defined above, γ is the friction coefficient (or coupling strength to the harmonic bath). ω_0 is the frequency at which the delta shaped memory kernel has maximum friction value or maximum strength of coupling. $\Delta\omega$ is the width of the friction profile. Notice that all the parameters related to the GLE thermostat are completely independent of the force field parameters. All we need to know is the position of the peaks of modes that we can obtain from the spectral density of the system in consideration. Non-Markovian dynamics can be mapped to Markovian dynamics in higher dimensional space[24] by adding auxiliary momentum degrees of freedom[1]. The modified higher dimensional dynamics can be implemented in the form of following dynamical equations,

$$\dot{q} = \frac{p}{m} \tag{2.22}$$

$$\begin{pmatrix} \dot{p} \\ \dot{\mathbf{s}} \end{pmatrix} = \begin{pmatrix} -\frac{\partial V}{\partial x} \\ 0 \end{pmatrix} - \mathbf{A} \begin{pmatrix} p \\ \mathbf{s} \end{pmatrix} + \mathbf{B}\xi(t) \tag{2.23}$$

Matrices $\mathbf{A}$ and $\mathbf{B}$ are the drift and diffusion matrices respectively. ξ is the uncorrelated Markovian noise, and $\mathbf{s}$ is the vector of additional momentum degrees of freedom. The drift and diffusion matrices may be constrained by the generalized FD theorem

$$(\mathbf{A} + \mathbf{A^T}) = M k_B T_{GLE} \mathbf{B}\mathbf{B^T} \tag{2.24}$$

The matrix $\mathbf{A}$ has the form $\begin{pmatrix} a_{pp} & \mathbf{a_{ps}} \\ \mathbf{a_{ps}^T} & \mathbf{a} \end{pmatrix}$. One can obtain functional form of the memory kernel from the matrix $\mathbf{A}$.

$$K(t) = 2a_{pp}\delta(t) - \mathbf{a_{ps}} e^{-|t|\mathbf{a}} \mathbf{a_{ps}^T} \tag{2.25}$$

The drift matrix $\mathbf{A}$ for that produces delta like friction profile in Eq. (2.20) is

[1]Note that the prescription to write Eq. (2.12) as higher dimensional Markovian process is a separate procedure and the auxiliary momenta s do not have any connection to the bath degrees of freedom (in this analysis). The auxiliary momenta s are introduced only for implementation purposes.

given by,

$$\mathbf{A} = \begin{pmatrix} 0 & \sqrt{\gamma(\frac{\Delta\omega^2+\omega_0^2}{2\Delta\omega})} & \sqrt{\gamma(\frac{\Delta\omega^2+\omega_0^2}{2\Delta\omega})} \\ -\sqrt{\gamma(\frac{\Delta\omega^2+\omega_0^2}{2\Delta\omega})} & \Delta\omega & \omega_0 \\ -\sqrt{\gamma(\frac{\Delta\omega^2+\omega_0^2}{2\Delta\omega})} & -\omega_0 & \Delta\omega \end{pmatrix} \tag{2.26}$$

2.2.3 Simulation Details

In this section we describe the implementation of NGLE thermostat. We begin by writing the classical evolution for the full dynamics. The infinitesimal evolution operator is given as,

$$\begin{aligned} U(\Delta t) &= e^{i\Delta t(L_{system}+L_{NHC}+L_{GLE})} && (2.27) \\ &\approx e^{i\frac{\Delta t}{2}(L_{GLE}+L_{NHC})}e^{i\Delta t L_{system}}e^{i\frac{\Delta t}{2}(L_{GLE}+L_{NHC})} && (2.28) \end{aligned}$$

Where L is the Liouville operator. The integrators for MD can be obtained from the Trotter factorization of Liouville propagators. The corresponding Liouville operators for NH and GLE are given in detail in Refs. ([24, 31]) respectively. The evolution of NH and GLE is updated at $\Delta t/2$ before and after the velocity-verlet routine for system evolution. As pointed out by Bussi and Parinello[30] there is a significant drift in the conserved quantity of the GLE dynamics for strong friction coefficient ($\gamma^{-1} \sim 10$ fs). This is mainly due to the error introduced by the approximate integrator for GLE when $\gamma\Delta t$ is not negligible. This error arises from the integration of the Hamilton equations and not from the friction itself. This problem can be solved by choosing a smaller time step for the simulation. In our simulation NGLE C (see Table. (2.1)) we use strong friction coefficient for zero point equilibration. For a stable conserved energy H' in Eq. (2.17), we perform this simulation with a time step of 0.05 fs. All the other simulations in this work are done with 0.5 fs time step.

As described in section 2.2.1 we have two thermostats acting on the system and they compete to enforce their respective temperatures. The strength

of the GLE thermostat varies with the frequency and is strongest for the modes in the range $\approx \omega_0 \pm \Delta\omega$. The result of this competition is that the modes in the range $\approx \omega_0 \pm \Delta\omega$ are thermostated at an effective temperature $T_{eff} < T_{NH}$. Depending on the strength of the friction coefficient (height of $K(\omega)$ peak), the effective temperature of the specific modes can lie anywhere between $0 \leq T(\omega)_{eff} \leq T_{NH}$. Temperature of all the other modes are equilibrated at $T \sim T_{NH}$ as the $K(\omega) \sim 0$ for $\omega \notin (\omega_0 - \Delta\omega,\ \omega_0 + \Delta\omega)$. Hence we can control the effective temperature of a particular normal mode using NGLE dynamics. Our system consists of 256 water molecules with a density of 0.997 g/cm^3 modeled by the flexible force field model q-TIP4P/F[5]. This model has been used in many isotope effects studies both for water and ice[15, 17, 32], and therefore is an excellent model to evaluate the performance of our approach. We now demonstrate effects of damping of narrow range of modes using NGLE thermostats. This example will establish the spirit in which we intend to use NGLE thermostats. We use in house developed code for the force field and MD implementations. In Fig. 2.2 we show the vibrational density of states (obtained from the Fourier transform of the velocity autocorrelation function) for the q-TIP4P/F model. The three peaks corresponds to translation+rotations ($400 - 1000\ cm^{-1}$), bending ($\sim 1600\ cm^{-1}$) and stretching ($\sim 3600\ cm^{-1}$) modes. We also plot the projected temperature of translation, rotation and intramolecular vibrational modes(see Fig. (2.8(a))). Mode-projected temperatures is an important parameter to monitor NGLE action on the system. We calculate these projections by defining new molecular subspaces along the center of mass (for the translations), molecular main three moment of inertia axis (for the rotations) and the three vibrational normal modes of the isolated molecule. These projections act as a guide to tune NGLE parameters for designing a frequency dependent temperature control. For GLE implementation we base our code on codes developed by Ceriotti *et al.*[2]. We see that without the GLE action all the modes are equilibrated to the temperature set by NH thermostats. We code the memory kernels to overlap with the vibrational spectrum of the system and tailor them to our requirement. We select a memory profile of very narrow width sharply peaked at some frequency, ω_0

[2]http://gle4md.berlios.de

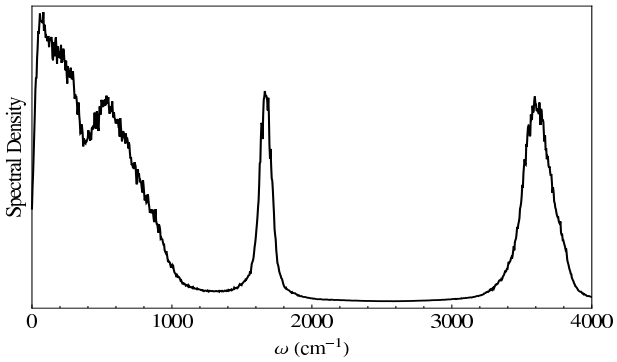

Figure 2.2: Spectral density plot of q-TIP4P/F liquid water equilibrated with NH thermostats at 300 K

which vanishes rapidly away from it. NH chains are set to 300 K. GLE is much more strongly coupled to the system than the NH chains at selective modes ($\omega_0 \pm \Delta\omega$). In the expression of memory kernel, Eq. (2.20), we set the peak position $\omega_0 = 3600\ cm^{-1}$, peak width $\Delta\omega = 5\ cm^{-1}$ and the strength of coupling $\gamma^{-1} = 1000$ ps (see Fig. 2.3). We now extend this method to study how the structure of liquid water changes when modes are kept at different temperatures.

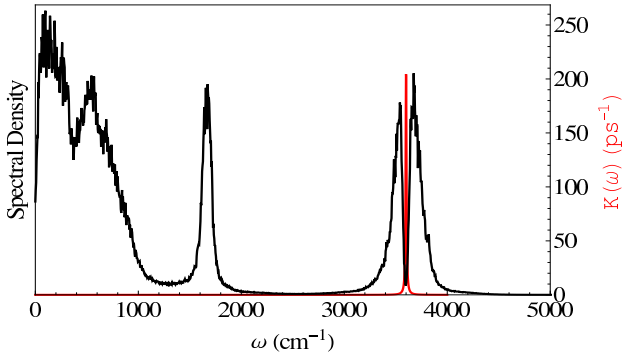

Figure 2.3: Spectral density plot of q-TIP4P/F liquid water at 300 K with NGLE, black line. Red line, delta-Like peak frequency depdendent friction profile.

2.3 NGLE applied to q-TIP4P/F water

Using NGLE to simulate liquid water to non-equilibrium distribution of temperatures, we can analyze how the structure of q-TIP4P/F water depends on the temperature of individual modes. This way we can establish the influence of each individual mode in the structure of the water. Also one can study how the different dynamical modes are connected to each other.

2.3.1 Weak damping of intramolecular modes

We damp the intramolecular modes and study their influence on the overall structure of liquid water, using a damping profile as shown in Fig. (2.4). For this simulation (NGLE A) parameters are described in Table 2.1. Projected temperatures plot (Fig 2.8(b)) show that the intramolecular modes are kept are relatively lower temperatures for the full simulation run.

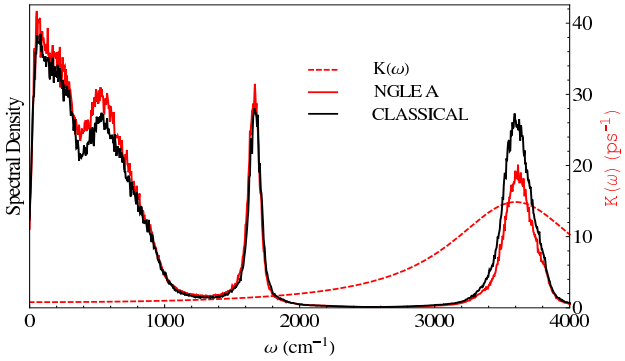

Figure 2.4: Spectral density plot. The black line is for of q-TIP4P/F liquid water at 300 K, the solid red line is for the NGLE A (see Table 2.1). The red dashed line shows the frequency dependent friction profile.

We also plot the radial distribution function (rdf) for NGLE A. This rdf clearly shows a local softening of the first two O-O peaks. On the other hand the first peak of the O-H rdf as expected is much sharper. The higher order peaks, linked to the Hbond network have also become softer. A more frozen covalent bond results in a loss of structure of liquid water. This is a consequence of the previously mentioned anticorrelation. The Hbond is

weakened by strengthening the O-H covalent bond.

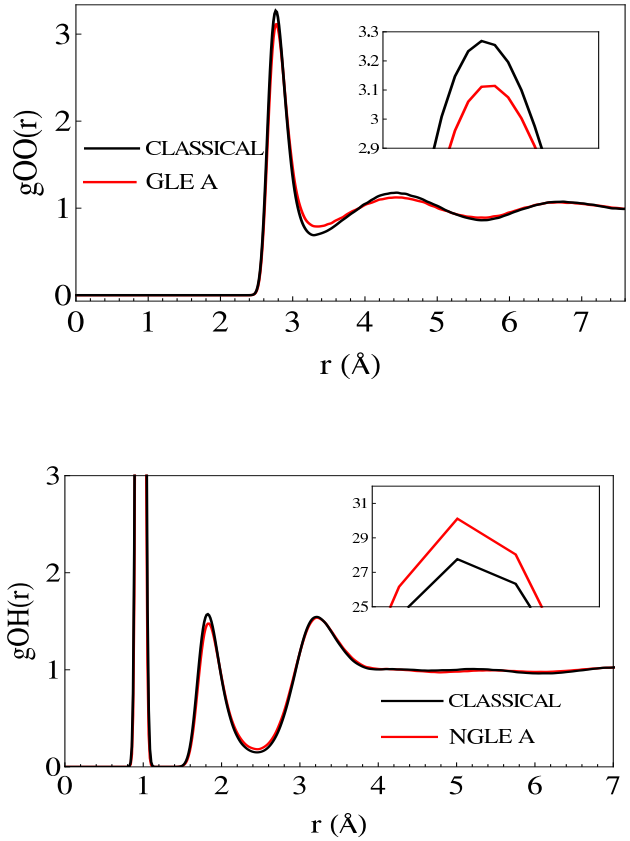

Figure 2.5: Radial distribution function plots of q-TIP4P/F liquid water for NVT simulation (black) at 300 K and NGLE damped OH stretching (red). Top: O-O rdf. Bottom: O-H rdfs, the inset shows a zoom into the first peak.

2.3.2 Weak damping of intermolecular modes

In this section we analyze whether a more fluctuating O-H covalent bond induces a local structuring of liquid water. To answer this question we now damp the low energy intermolecular modes. We couple GLE to low energy modes with almost no coupling to intramolecular modes. The parameters for this simulation (NGLE B) are described in Table 2.1 The Results are shown in Figs. (2.6,2.8).

The action of damping low energy modes results in relatively higher tem-

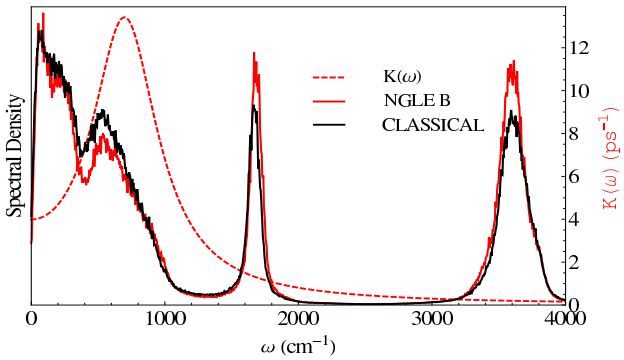

Figure 2.6: Spectral density plot. The black line is for of q-TIP4P/F liquid water at 300 K, the solid red line is for the NGLE B (see Table 2.1). The red dashed line shows the frequency dependent friction profile.

perature of vibrational modes (see Fig. 2.8(c)). Consequently, we see more structure in the O-O rdf (see Fig. 2.7). This establishes the well know anti-correlation [18] between inter and intramolecular modes in liquid water. Hence we demonstrate that the strengthening of the water structure (by more frozen Hbonds) implies a more delocalized O-H intramolecular bond, i.e. a softening of the stretching OH vibration. In Table (2.1) we present normal mode-projected temperatures for translations, rotations and vibration modes.

Table 2.1: Temperature distribution among individual modes

	T_{NH}(K)	Trans(K)	Rot(K)	Vib(K)	ω_0 (cm^{-1})	$\Delta\omega$ (cm^{-1})	γ^{-1} (ps)	T_{GLE}(K)
NVT	300	299	300	302	-	-	-	-
NGLE A	300	295	325	240	3600	800	0.9	0.0001
NGLE B	300	295	270	325	700	300	0.2	0.0001
NGLE C	1600	600	800	2200	700	650	0.006	0.0001

2.3.3 Modes close to their zero point temperature

None of the results shown in the previous sections were surprising, they are a confirmation of the anti-correlation effect. This effect is a manifestation of the strong anharmonicity of the vibrational modes, which strongly couple to the rotational modes when Hbonds are formed. However, when all the normal modes are equilibrated at their corresponding zero point temperatures, the two

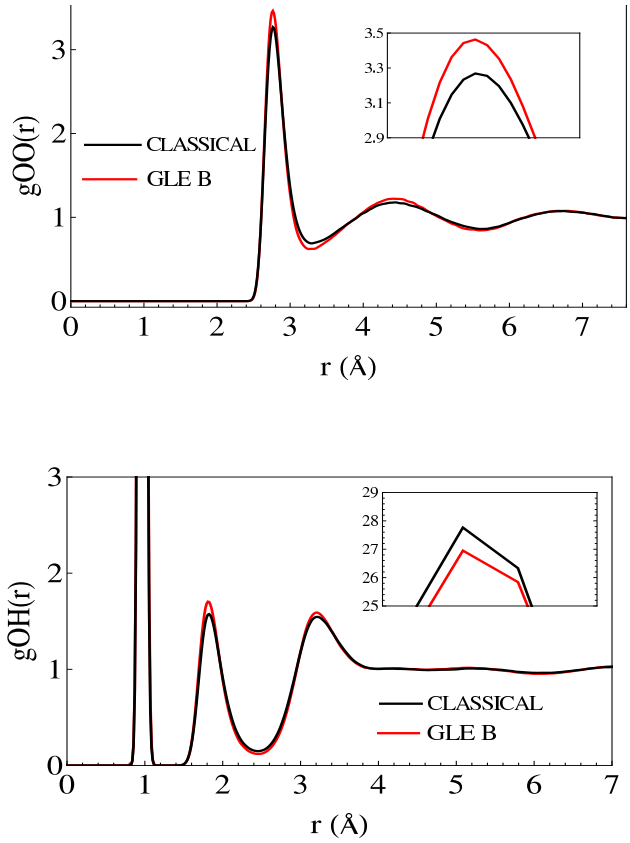

Figure 2.7: Radial distribution function plots of q-TIP4P/F liquid water for NVT simulation (black) at 300 K and NGLE damped intermolecular stretching (red). Upper panel: O-O rdf. Lower panel : O-H rdfs, the inset shows a zoom into the first peak.

opposite effects we just described should balance out. As shown by Habershon *et al.* [5], this competion results in an overall minimization of quantum effects on the structure of liquid water. To evaluate this using our method, we set the NH-temperature close to the zero point temperature of vibrational modes and damp intermolecular modes so that the effective temperature of the low energy modes are close to their effective zero point temperature. The shape of the tailored frequency dependent memory profile is shown in Fig. (2.9). The advantage we have is that very few parameters are used to achieve this non equilibrium T distribution.

We plot the rdfs of liquid water for this case (see Fig. (2.10)) and compare

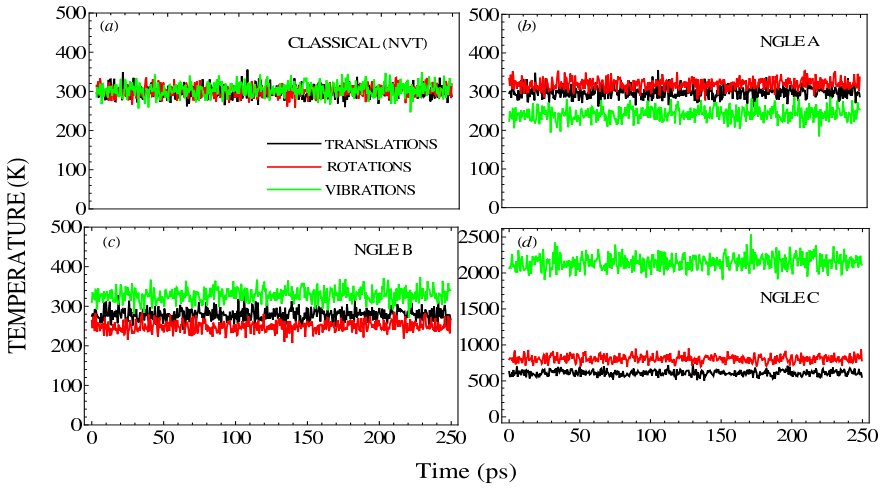

Figure 2.8: Temperature of translational (black), rotational (red) and vibrational (green) modes in liquid water plotted as a function of time. This mode projected temperature is plotted for (a) NVT simulation at 300 K. (b) NGLE A simulation with damped intramolecular OH stretching . (c) NGLE B simulation with damped intermolecular modes. (d) NGLE C simulation with modes close to effective zero point temperature. See Table (2.1) for temperature values.

them with those obtained from a "classical" and a PIMD simulation, both of an identical system. By "classical" we mean a standard NVT MD simulation at T=300 K, with the use of a NH thermostat (without any GLE). The PIMD simulation was performed using the same method as described in Ref. ([15]), using a polymer ring of P=32 beads. Fig. (2.10) clearly demonstrates that using NGLE (with NGLE-C parameters, see Table (2.1)) we can equilibrate modes to their average zero point temperature and the obtained rdfs are in good agreement with PIMD results.

2.3.3.1 Vibrational spectrum

Since NGLE is a deterministic thermostat, one of the advantages of this method is that dynamical properties are described with the same accuracy as in NH simulations. This allows us to study the changes on the vibrational spectrum induced by the new distribution of normal mode temperatures. In other words, it allows us to evaluate the intrinsic anaharmonicities of liquid wa-

ter (which strongly depend on the underlying model) at the correct zero-point temperature distribution.

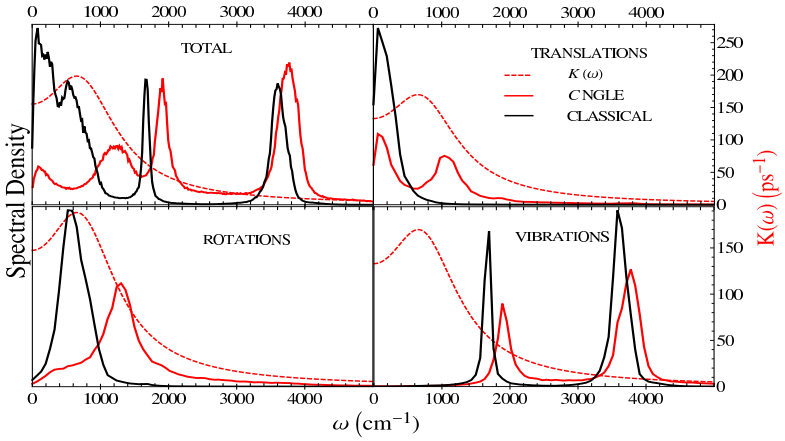

Figure 2.9: Spectral density plots, decomposed into different vibrational contributions. Total spectrum (top left panel). Projection onto translations (top right), rotations (bottom left) and vibrations (bottom right). Solid black line, NVT simulation at T=300 K. Red solid line, NGLE C (see Table (2.1)) simulation. The red dashed line shows the frequency dependent friction profile used in NGLE C.

In order to accurately evaluate how each region of the vibrational spectrum changes, we have obtained the spectral density projected onto translational, rotational and vibrational modes separately. The procedure is straightforward once the cartesian coordinates are projected onto the normal mode coordinates. The spectral density is obtained by computing the Fourier transform of the velocity-velocity autocorrelation function within each independent normal mode subspace. Results are presented in Fig. (2.9). The figure shows both the changes to the total spectrum (top left panel), and to the translations (top right), rotations (bottom left) and vibrations (bottom right).

The partition of the spectrum helps on identifying which are the modes that undergo major frequency shifts upon addition of quantum effects. The largest, and more interesting changes occur in the translational and rotational regions of the spectrum. While the lowest frequency translational motions remain unaffected, those modes with classical frequencies above $\approx$200 cm^{-1}

are strongly blue shifted. These are modes associated to the Hbond stretching. The rotational peak also undergoes a large blue shift, although some of the modes also remain unaffected. The shifted rotational modes most likely correspond to those associated to Hbond bendings. In both cases, the shift is a consequence of the large temperature NGLE imposes on the intramolecular vibrational modes. Indeed, as seen in Table (2.1), label "NGLE C" and in Fig. 2.8 (d), the net T of the vibrational modes is 2200 K. This large blue shift confirms the strong coupling between inter and intra molecular modes, or a strong intrinsic anharmonicity. This shift also modifies their corresponding zero point temperature. To account for this zero point shift, our NGLE parameters are tuned to equilibrate intermolecular modes to 600 K (trans) 800 K (rotations) whereas intramolecular modes are equilibrated at 2200 K.

The strong coupling between the different modes makes it difficult to fully determine the actual quantum vibrational spectrum of the model. How much a given model's vibrational spectrum should be modified upon consideration of NQE is an open question, not easy to address within a thermostated simulation [33, 34]. Nonetheless, our scheme is particularly suited to extract dynamical information. First of all, the method ensure the absence of zero-point leakage, as seen in the conservation of mode-projected temperatures through the simulation length. Secondly, due to the suppression of GLE noise, we do not add any more diffusion to the system, other than that associated to the NH thermostat. A first principles MD simulation of liquid water and its vibrational spectrum under the action of our NGLE thermostat will help to gain insight into the model-dependence of the NGLE spectrum.

2.4 Analysis and Discussion

In this section we present analysis of our results of selective mode thermostating of liquid water. Based on our results we are in a position to provide deeper insight into the role of individual modes contributing to the overall structure of liquid water.

2.4.1 Emergence of water structure from stretching modes

The results for zero point simulation using NGLE can also be interpreted from a different view point. In this section we compare classical simulation done at 600 K to our effective zero point simulation done at 600 K (translations), 800 K (rotations) and 2200 K (vibrations) ("NGLE C" in Table (2.1)).

Fig. (2.11) shows that for a classical simulation equilibrated at 600 K the liquid water structure is completely lost, as expected for such a high temperature. Indeed at this T the liquid is at a supercritical state, because we do not allow the volume of our simulation cell to change. The O-O rdf in red is a liquid water structure that emerges completely due to the higher temperature imposed on the stretching modes. This comparison clearly points out that zero point temperature of O-H stretching modes plays a dominant role in the structuring of liquid water.

2.4.2 Role of individual modes from PIMD simulations.

So far in this work we have demonstrated how quantum effects corresponding to individual modes effect the overall structure of liquid water. In this section we try to extract this information from PIMD simulations. Recent work of Habershon *et al.* [5] established the idea of competing quantum effects by understanding the role of intramolecular stretching modes. They observe reduced quantum to classical ratio of diffusion coefficient when the O-H stretching is allowed. This is due to the anharmonicity of the stretching mode, which couples it to the rotational and translational modes. This is in agreement with our results. However in this work we aim to understand this effect in terms of the zero point temperature of competing modes. In PIMD simulations, we map the zero point temperature on individual modes to the number of beads. The quantum limit is achieved with $P \to \infty$, P being the number of beads employed for the discretization of the path integral. A PIMD simulation with finite P at temperature T implies a high-temperature approximation, i.e. the partition function of the system is considered to be classical at a higher temperature given by the product PT. Usually the value of P is chosen so that the product PT is several times larger than the zero point temperature of the

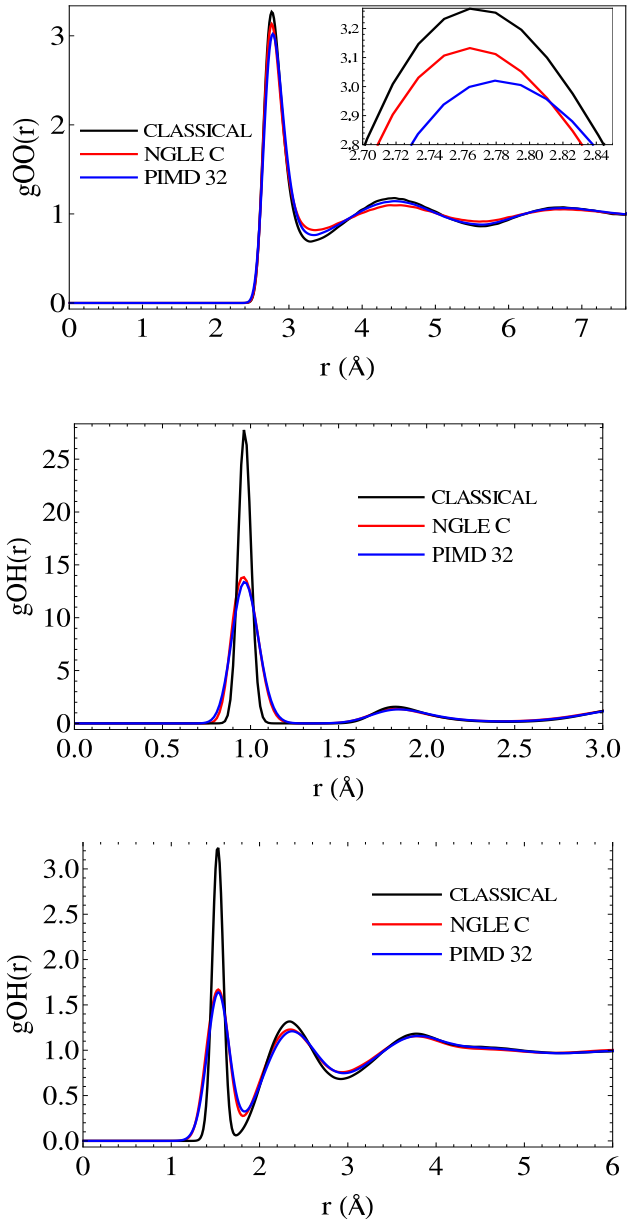

Figure 2.10: Radial distribution plots. Top: O-O rdf. Middle O-H rdf. Bottom H-H rdf. Black line: NVT simulation at 300 K. Red line: Zero-point NGLE simulation (NGLE C, in Table (2.1)). Blue line: PIMD simulation with 32 beads.

highest frequency.

We study the structure of liquid water as a function of P. We plot the

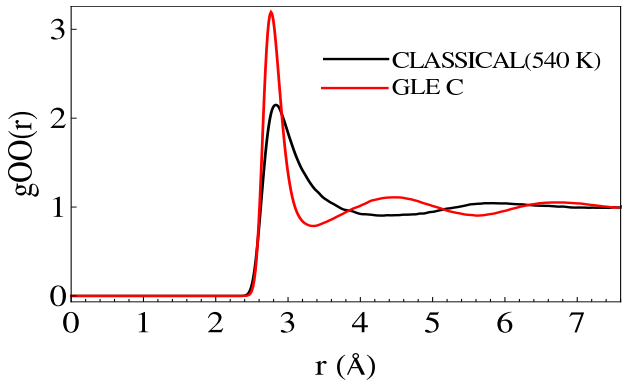

Figure 2.11: O-O Radial distribution function. Red line: NGLE C (see Table (2.1)) with a temperature distribution of: 600 K translations, 800 K rotations and 2200 K vibrations. Black line: NVT simulation equilibrated at 600 K.

rdf obtained from PIMD for O-O and O-H pairs, for a 256 molecules water simulation of 250 ps length and density 0.997 g/cm^3 (see Fig. 2.12).

Based on the plots in Fig. (2.12) we can analyze how the zero point effects of each mode influences the structure of liquid water. To understand the structure we introduce an order parameter which is the ratio of the first maxima to the first minima of the O-O rdf. The increasing value of this ratio is related to the increasing structure of liquid water. We plot this ratio as a function of P. For the O-H rdf we plot the height of the first peak as a function of P (see Fig. (2.13)).

In Fig. (2.13) we observe that for $P \leq 10$, i.e. for $PT \leq 3000$K goo(r) looses structure compared to the classical (P=1 bead) case. This can be attributed to the fact that using only a few beads, the zero point temperature of intermolecular modes is well captured and they tend to unstructure the liquid. However for small P the PIMD simulation is not able to describe the zero point vibration of the O-H stretching modes. We have already mentioned that the temperature PT must be several times larger that the zero point temperature for a reasonable approximation of the quantum limit in a PIMD simulation.. As we further increase no. of beads we see that goo(r) starts gaining structure. This gain in structure is due to the better and better description of zero point effects of intramolecular modes. This gain in structure saturates when the

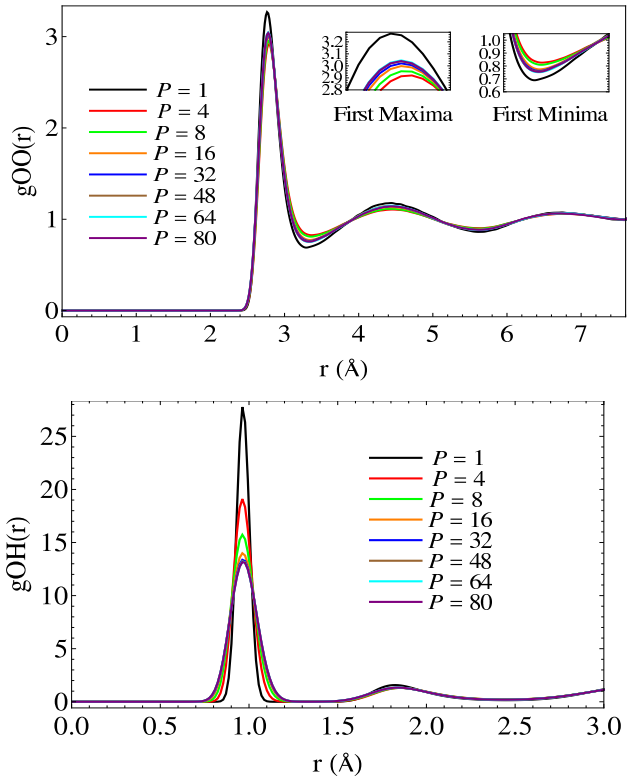

Figure 2.12: Radial distribution function plots for PIMD simulations as a function of the number of beads. Top: O-O rdf. The two insets are zoomed into the first peak and the first minima. Bottom: O-H rdf

intramolecular modes are kept close to their zero point temperature. Hence using P as a control parameter for quantum effects, we can understand the competition between intra and intermolecular modes. We also see a crossover from unstructuring to structuring in goo(r) (Fig. (2.12)) as we increase the no. of beads. A model with too little anticorrelation as the one used here [18], will not structure above the classical level, independently of the number of beads used.

2.5 Conclusions

In this work, we have combined NH and GLE thermostats to create a powerful selective mode thermostating scheme, that we coin NGLE. Using NGLE

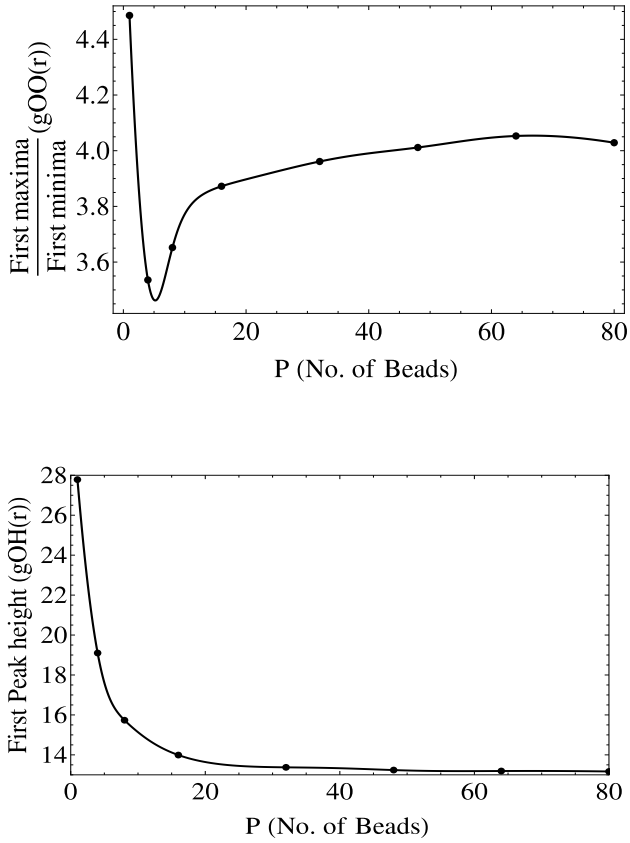

Figure 2.13: Order parameter as a function of the number of beads in PIMD simulations. Top: ratio of the height of first maxima to first minima. Bottom: height of first peak of the O-H rdf. The points are the actual data and the solid line is a fourth order interpolation.

we were able to equilibrate vibrational modes to different temperatures, ensuring the maintenance of the NGLE-imposed non-equilibrium temperature distribution for any simulation time length. The GLE noise is suppressed by setting the GLE temperature close to zero, making the thermostat dynamics deterministic. We have applied NGLE to a flexible force field model of water (q-TIP4P/F). Our results show that the structure of liquid water changes when intramolecular modes are equilibrated to a different temperature than that of intermolecular modes. We showed that equilibrating vibrations at slightly lower temperature than other modes results in the loss of structure in liquid water. Conversely water is more structured if we equilibrate vibrations

to slightly higher temperature. This simple exercise verifies the well known anticorrelation effect [18] in terms of the temperature of individual modes. Simply changing NGLE parameters we can set all modes to their corresponding zero point temperature. Equilibrating the intramolecular modes close to their zero point temperature ($\sim$ 2200 K) results in blue shift in the peak of the intermolecular (translation+rotation) modes. This indicates the large intrinsic anharmonicity of the vibrational modes in liquid water. Our zero point estimates of translations and rotations prove to be correct as NGLE simulations reproduce O-O, O-H and H-H rdf obtained from PIMD simulation with 32 beads. Finally, we have analyzed selective mode behavior as a function of their zero point temperature in PIMD. To this aim we showed that by a systematic increase of the number of beads P in PIMD simulations, the different vibrational modes of water can be successively tuned from a classical to a quantum limit. The height of first peak of the O-H rdf continuously decreased as a function of P. This effect is similar to adding more zero point temperature on vibrations. For $P \leq 10$, there is drastic softening of long range structure as seen in the O-O rdf. This is the case when the temperature of low energy modes are close to their zero point temperature but the vibration temperature is still far away from its zero point. For $P > 10$ we observe an increase of structure in the O-O rdf that asymptotically saturates with P. This is a consequence of intramolecular modes equilibrated to their zero point temperature. In summary, we successfully introduced a selective mode thermostating scheme (NGLE), which can be easily tuned to include quantum zero point effects, producing results in good agreement with PIMD. We used it to study how the structure of liquid water responds to different temperatures, unveiling the existence of large intrinsic anharmonicities in the vibrational modes of liquid water.

Chapter 3

Quantum effects in 2-D: Transport in d-wave superconductors

3.1 Introduction

The low-energy excitations of a d-wave superconductor are the Bogoliubov quasiparticles that reside in the vicinity of the four gap nodes at which the order parameter vanishes. The physics of these quasiparticles can be probed experimentally via a variety of low-temperature electrical and thermal transport measurements. Since quasiparticles are part electron and part hole, their energy is well defined but their charge is not. Thus, it is thermal current that follows quasiparticle current. Since $T \ll T_c$, we are well within the superconducting state. Since $T \ll \Delta_0$ (the gap maximum), transport is dominated by quasiparticles excited in the vicinity of the gap nodes. (The quasiparticle dispersion is therefore given by the anisotropic Dirac spectrum, $E = (v_f^2 k_1^2 + v_2^2 k_2^2)^{1/2}$,where v_f is the Fermi velocity, v_2 is the slope of the gap, and k_1 and k_2 are defined locally about each node. We shall choose our axes such that gap nodes are located at $\pm p_F \hat{\mathbf{x}}$ and $\pm p_F \hat{\mathbf{y}}$ in momentum space.) Furthermore, the temperatures of interest are low enough that sources of inelastic scattering are frozen out. This is what we mean by low-temperature quasiparti-

cle transport. In the mixed state, the remaining energy scales are the impurity scattering rate, Γ_0, the vortex scattering rate, Γ_v, and the temperature. We will focus on the weak-field high-temperature regime where $\Gamma_v \ll T$ and T is the dominant energy scale. In this regime, the quasiparticles responsible for transport are thermally generated rather than impurity-induced [35–37] or magnetic field-induced [38–40].(Note that thermal transport in the opposite, low T, regime has been discussed frequently in the literature [41–45].) In this high T regime, the physical situation is relatively simple, thermally excited quasiparticles carry the heat current. To understand the thermal transport, we only need to understand how they scatter from magnetic vortices. Experiments by Ong et. al ([7, 8])(See. Fig. (3.1)) have been successful in isolating the quasiparticle contribution by thermal Hall measurements. The longitudinal conductivity κ_{xx} is generally plagued by contributions from phonons. Hence, by measuring the transverse conductivity one can isolate the quasiparticle contribution as phonons are not skew scattered by vortices. In the vortex

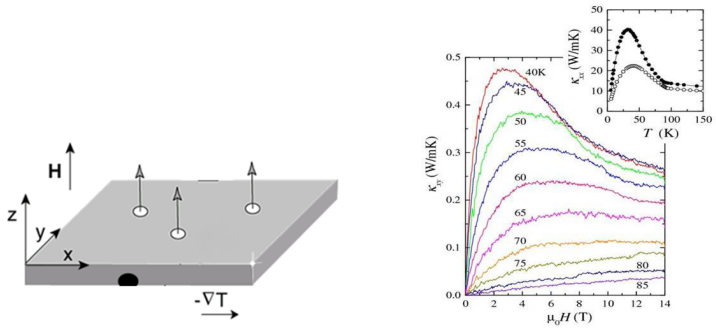

Figure 3.1: (Left) Thermal hall transport measurement schematic. (Right) Thermal hall conductivity (κ_{xy}) vs magnetic fields $H_0(T)$ and longitudinal thermal conductivity (κ_{xx})(inset) plotted vs temperature. Images taken from N. P. Ong's website.

state, low-temperature transport properties, such as the longitudinal thermal conductivity and thermal Hall conductivity, can be explained by studying the scattering of these quasiparticles from magnetic vortices. Since $H \ll H_{c2}$, the vortices are dilute, separated by distances large compared to the quasiparticle de Broglie wavelength. Quasiparticles scatter from vortices via two basic mechanisms: a circulating superflow and a Berry phase factor of (-1)

acquired upon circling a vortex. Scattering due to superflow current in a single vortex (without the Berry phase effect) has been calculated in Refs. [46] and [1]. Although the transport properties calculated in Ref. [46] capture the essential physics qualitatively, the Berry phase effect becomes important for the higher field (lower temperature) regime where the deBroglie wavelength is comparable to the distance between vortices. It is therefore of interest to consider the effect of Berry phase on the quasiparticle scattering. The influence of the Aharonov-Bohm (AB) effect due to an isolated vortex line on the quasiparticle states has been studied in the Refs [47] and [48]. Ref [47] also obtains the quasiparticle wavefunction and density of states at distances from the vortex large compared to the pentration depth ($r >> \lambda$). In this work, we consider ($r << \lambda$) and work in the limit $\lambda \to \infty$, such that the magnetic field is constant across the sample. This limit permits the application of a singular gauge transformation that encodes the Berry phase effect in the form of anti-periodic boundary conditions on the quasiparticle wave function. In contrast to conventional superconductors, the density of states at low energies in d-wave systems is dominated by contributions from the regions far from the cores [38] which are associated with extended quasiparticle states with momenta close to the nodal directions. This allows us to neglect the vortex core physics by zeroing the coherence length ($\xi \to 0$). This conclusion, based on the semiclassical approach [47, 49], has been confirmed by numerical analysis [50] of the BdG equations for a single isolated vortex line (in the limit $\lambda \to \infty$). Note that the calculations presented in [50] also point to the absence of truly localized core states or any resonant levels in the pure d-wave case, though such states were observed in numerical simulations [51]. The AB effect on quasiparticle excitations in macroscopic superconducting rings has been studied in detail in Refs [52] and [53]. In this work, we now calculate the scattering contribution due to the Berry phase effect. We take the following path. As discussed in Ref. [1] and summarized in Appendix 3.2, we apply a singular gauge transformation to the Bogoliubov-de Gennes equation and shift the origin of momentum space to the location of one of the gap nodes. This reduces the problem to that of an (anisotropic) Dirac fermion scattering from an effective non-central potential (due to the superflow) in the presence of antiperiodic

boundary conditions (a consequence of our gauge choice). For simplicity, we neglect the anisotropy of the Dirac dispersion by taking $v_f = v_2$. Since we are only interested in the Berry phase contribution, we neglect the presence of the effective non-central potential, which further reduces the problem to that of a massless Dirac fermion scattering due to the antiperiodic boundary conditions. Within the single-vortex approximation, the antiperiodic boundary condition manifests itself as a semi-infinite branch cut terminating at the vortex core. In Sec. 3.3 we study the single vortex scattering of quasiparticles due to this semi-infinite branch cut (without superflow current) and obtain a divergent differential cross section in the forward direction. The divergent nature of this cross section is unphysical and requires that we regularize this semi-infinite branch cut. In real situations these branch cuts terminate on the cores of the neighboring vortices and are finite in nature. Thus, considering a pair of vortices as our scatterer captures the finite branch cut and regularizes the Berry phase effect. Elliptical coordinates serve as a natural choice for this problem with two vortex cores. The presence of a finite branch cut between the two vortices manifests itself as a boundary condition on the wave function spinor across the line segment joining the two foci of the ellipse. In elliptical coordinates (μ, ν), we simply write

$$\psi(\mu, -\nu) \mid_{\mu=0} = (-1)^B \; \psi(\mu, \nu) \mid_{\mu=0} \tag{3.1}$$

We can impose the Berry phase condition using parameter B ($B = 0, 1$). When B=0, there is no branch cut between the vortex cores. We can turn on the Berry phase (branch cut) between the vortex cores by setting B=1. Thus, neglecting the anisotropy of the gap nodes, our problem reduces to that of the scattering of massless Dirac quasiparticles due to this finite branch cut. A similar setup for the scattering of quasiparticles due to the Berry phase has been considered by Melikyan and Tesanovic in Ref. [54]. Their approach was to construct scattering solutions to the 2d Dirac equation in elliptical coordinates from solutions to the Klein-Gordon equation (separated in elliptical coordinates) using self-adjoint extensions. But in going from Klein-Gordon to Dirac, the solutions are not separated in elliptical coordinates anymore. This results

in not being able to construct all the self-adjoint extensions. In this work, we avoid the issue of self-adjoint extensions by taking a different approach. We directly separate the (2+1)d Dirac equation in elliptical coordinates [55, 56]. The separation of variables is done in Sec. 3.5. The separated equations are Whittaker Hill equations (WHE) [55, 57]. In Sec. 3.6 we solve the separated equations to obtain eigenfunctions [58–66]. In Sec. 3.7, we develop an expansion for the incident plane wave (representing quasiparticle current) in terms of the separated solutions of WHE. In Sec. 3.8 we construct the scattering amplitude (as a sum of partial waves) from the asymptotic form of the scattered wave. We impose the boundary condition Eq. (3.1) on the full wavefunction spinor and calculate the phase shifts for each partial wave. We show that for B=0 (no branch cut) there is no quasiparticle scattering. In Sec 3.10, we turn on the Berry phase by setting B=1 (with branch cut between cores) and obtain a non-zero scattering cross section. Results and an analysis of the quasiparticle scattering cross section in the presence of Berry phase are presented in Sec. 3.11. Conclusions are discussed in Sec. 3.12.

3.2 Bogoliubov-de Gennes Equation

The setup for this problem is described in detail in Ref. [1, 67]. We summarize here. Consider the Bogoliubov-de Gennes (BdG) equation for a d-wave superconductor in the presence of a constant perpendicular magnetic field, $\mathbf{A} = \frac{1}{2}Hr\hat{\phi}$, and with an order parameter that winds once about the origin, $\Delta(\mathbf{r}) = \Delta_0 e^{i\phi}$:

$$H'\Psi = E\Psi \qquad H' = \begin{pmatrix} \hat{H}'_e & \hat{\Delta}' \\ \hat{\Delta}'^* & -\hat{H}'^*_e \end{pmatrix} \tag{3.2}$$

$$\hat{H}'_e = \frac{1}{2m}\left(\mathbf{p} - \frac{e}{c}\mathbf{A}\right)^2 - E_F \tag{3.3}$$

$$\hat{\Delta}' = \frac{1}{p_F^2}\{\hat{p_x}, \{\hat{p_y}, \Delta(\mathbf{r})\}\} - \frac{i}{4p_F^2}\Delta(\mathbf{r})(\partial_x\partial_y\phi) \tag{3.4}$$

Here $\mathbf{p} = -i\hbar\nabla$, $\{a, b\} = (ab + ba)/2$, and E is the quasiparticle energy. The form of the gap operator enforces the d-wave symmetry [44, 68]. Upon circling

an $hc/2e$ vortex, the quasiparticle acquires a Berry phase factor of (-1). This fact is encoded within the complex differential form of the gap operator, $\hat{\Delta}$. We simplify the Hamiltonian by effectively stripping the gap function, $\Delta(\mathbf{r})$, of its phase. This is done by applying the singular gauge transformation

$$U = \begin{pmatrix} e^{-i\phi/2} & 0 \\ 0 & e^{i\phi/2} \end{pmatrix} \qquad \Phi(\mathbf{r}) = U^{-1}\Psi(\mathbf{r}) \qquad H = U^{-1}H'U. \tag{3.5}$$

In this gauge, known as the Anderson gauge,

$$H\Phi = E\Phi \tag{3.6}$$

$$H = \tau_3 \frac{v_f}{2p_F}\left[(\mathbf{p} + \tau_3\mathbf{P}_s)^2 - p_F^2\right] + \tau_1 \frac{v_2}{2p_F}\left[2p_x p_y\right] \tag{3.7}$$

where

$$\mathbf{P}_s(\mathbf{r}) = \frac{\hbar}{2}\nabla\phi - \frac{e}{c}\mathbf{A} = \frac{\hbar}{2}\left(\frac{1}{r} - \frac{r}{R^2}\right)\hat{\phi} \tag{3.8}$$

is the gauge invariant superfluid momentum (superflow), $v_f = p_F/m$, $v_2 = \Delta_0/p_F$, and $R \equiv \sqrt{\hbar c/eH}$. In effect, the Berry phase contribution has been extracted from the Hamiltonian and encoded in the antiperiodic boundary conditions imposed on the wave function. While the original wave function was defined with periodic boundary conditions, $\Psi(r,\phi) = \Psi(r,\phi+2\pi)$, the transformed wave function is not single-valued and has antiperiodic boundary conditions, $\Phi(r,\phi) = -\Phi(r,\phi+2\pi)$. Hence, we have introduced a branch cut such that with each trip around the origin, the wave function changes sign. Note that the Berry phase effect is not a consequence of the choice of gauge. We have used the singular gauge transformation to extract the Berry phase contribution from the Hamiltonian and encode it in the boundary conditions of the wave functions. By definition, all observables, such as differential cross section or transport coefficients, are independent of this gauge choice. For other problems, other gauge choices are optimal. A nice discussion of this is provided for the case of vortex lattice by Franz and Tesanovic [50] and Vafek et al [69]. We can further simplify our Hamiltonian by shifting the origin of

momentum space to the location of one of the nodes. Shifting to node 1

$$p_x \to p_F + p_x \qquad p_y \to p_y \tag{3.9}$$

we find that

$$\begin{aligned} H &= H_D + H_C && (3.10)\\ H_D &= v_f \left[p_x\tau_3 + \alpha p_y \tau_1 + P_{sx}\right] && (3.11)\\ H_C &= \frac{v_f}{2p_F}\left[(p^2 + P_s^2)\tau_3 + 2\mathbf{P}_s\cdot\mathbf{p} + \alpha 2 p_x p_y \tau_1\right] && (3.12) \end{aligned}$$

where $\alpha = v_2/v_f$ and we have used the fact that $\mathbf{P}_s = P_s(r)\hat{\phi}$ to commute $\mathbf{p}$ with $\mathbf{P}_s$. Here H is written as the sum of a linear (Dirac) Hamiltonian, H_D, and a quadratic (curvature) Hamiltonian, H_C. The second (curvature) term is smaller than the first by a factor of E/E_F. We will focus on the dominant term, H_D. In order to study the quasiparticle scattering from vortices, we must consider the nature of the quasiparticle current in a *d*-wave superconductor. Since the incident and scattered currents will be considered in the far field where the quasiparticles are free, we wish to determine the quasiparticle current as a functional of Φ for $P_s = 0$. Setting $P_s = 0$ in Eq. (3.7) we find that the BdG Hamiltonian becomes

$$H = \begin{pmatrix} \hat{H}_e & \hat{\Delta} \\ \hat{\Delta}^* & -\hat{H}_e^* \end{pmatrix} \qquad \hat{H}_e = -\frac{v_f}{2p_F}\nabla^2 - E_F \qquad \hat{\Delta} = -\frac{v_2}{2p_F} 2\partial_x\partial_y \tag{3.13}$$

Following Refs. [1] and [70], we can write down the quasiparticle current corresponding to the BdG Hamiltonian. Once again, it is convenient to shift the origin of momentum space to a nodal point. Shifting to node 1 yields

$$\begin{aligned} \mathbf{j} &= \mathbf{j}_D + \mathbf{j}_C && (3.14)\\ \mathbf{j}_D &= v_f \Phi^\dagger(\tau_3\hat{\mathbf{x}} + \alpha\tau_1\hat{\mathbf{y}})\Phi && (3.15)\\ \mathbf{j}_C &= \frac{v_f}{p_F}\mathrm{Im}\left[\Phi^\dagger(\tau_3\hat{\mathbf{x}} + \alpha\tau_1\hat{\mathbf{y}})\frac{\partial\Phi}{\partial x} + \Phi^\dagger(\tau_3\hat{\mathbf{y}} + \alpha\tau_1\hat{\mathbf{x}})\frac{\partial\Phi}{\partial y}\right] && (3.16) \end{aligned}$$

where $\alpha = v_2/v_f$. In what follows, we will focus on the dominant term $\mathbf{j}_D$ corresponding to the Hamiltonian $\mathbf{H}_D$.

To proceed, we must obtain a general form for the scattering cross section. We consider a plane wave, with quasiparticle current in the incident direction, scattering off a vortex as a radial wave, with quasiparticle current in the scattered direction. If the incident momentum is $\mathbf{k} = (k, \theta)$ and the final momentum is $\mathbf{k}' = (k, \phi)$, then the incident direction is the direction of the group velocity at momentum $\mathbf{k}$ and the scattered direction is the direction of the group velocity at momentum $\mathbf{k}'$. For general, anisotropic nodes, the group velocity need not be parallel to the momentum. However, for the isotropic case that we consider

$$\mathbf{v}_G(\mathbf{k}) = \frac{\partial E_k}{\partial \mathbf{k}} = v_f \frac{\epsilon_k}{E_k}\hat{\mathbf{x}} + v_2 \frac{\Delta_k}{E_k}\hat{\mathbf{y}} = v_f \left(\cos\theta\hat{\mathbf{x}} + \sin\theta\hat{\mathbf{y}}\right) = v_f \hat{\mathbf{k}} \tag{3.17}$$

and the group velocity and momentum are parallel. Therefore, if Φ_i denotes the incident wave function and Φ_s denotes the scattered wave function, then we require

$$\mathbf{j}_D[\Phi_i] \sim \left(\cos\theta\hat{\mathbf{x}} + \sin\theta\hat{\mathbf{y}}\right) \sim \hat{\mathbf{k}} \qquad \mathbf{j}_D[\Phi_s] \sim \left(\cos\phi\hat{\mathbf{x}} + \sin\phi\hat{\mathbf{y}}\right) \sim \hat{\mathbf{k}}' \sim \hat{\mathbf{r}}. \tag{3.18}$$

Inspection of the form of the current functional, $\mathbf{j}_D = v_f \Phi^\dagger(\tau_3\hat{\mathbf{x}} + \tau_1\hat{\mathbf{y}})\Phi$ reveals that the appropriate incident plane wave is

$$\Phi_i(\mathbf{r}) = e^{i\mathbf{k}\cdot\mathbf{r}} \begin{pmatrix} \cos\frac{\theta}{2} \\ \sin\frac{\theta}{2} \end{pmatrix} \tag{3.19}$$

Note that outside the vortex, quasiparticles are subject to neither an order parameter phase gradient nor a magnetic field. Thus, the incident wave function is a plane wave. This is consistent with the well-known results of Franz and Tesanovic [50] who showed that the low-energy quasiparticle states of a d-wave superconductor in the vortex state are Bloch waves of massless Dirac fermions rather than Landau Levels. (For a discussion of the analysis that led to this important result, the reader is referred to Refs. [50, 71–73].)

$$\mathbf{j}_D[\Phi_i] = v_f \left[\left(\cos^2 \frac{\theta}{2} - \sin^2 \frac{\theta}{2} \right) \hat{\mathbf{x}} + \left(2 \sin \frac{\theta}{2} \cos \frac{\theta}{2} \right) \hat{\mathbf{y}} \right] = v_f \hat{\mathbf{k}}. \tag{3.20}$$

Note also that this form solves the BdG equation, as it must in the absence of the vortex. The appropriate scattered radial wave is then given by

$$\Phi_s(\mathbf{r}) = e^{i\frac{\phi}{2}} f(\phi, \theta) \frac{e^{ikr}}{\sqrt{r}} \begin{pmatrix} \cos \frac{\phi}{2} \\ \sin \frac{\phi}{2} \end{pmatrix} \tag{3.21}$$

$$\mathbf{j}_D[\Phi_s] = v_f \frac{|f|^2}{r} \left[\left(\cos^2 \frac{\phi}{2} - \sin^2 \frac{\phi}{2} \right) \hat{\mathbf{x}} + \left(2 \sin \frac{\phi}{2} \cos \frac{\phi}{2} \right) \hat{\mathbf{y}} \right] = v_f \frac{|f|^2}{r} \hat{\mathbf{r}}. \tag{3.22}$$

Here $f(\phi, \theta)$ is the scattering amplitude and the $e^{i\phi/2}$ prefactor has been added to make the wave function single-valued.

3.3 Berry Phase Scattering of Incident Plane Wave in Single Vortex Approximation (Without Superflow)

Quasiparticles scatter from vortices via both the circulating superflow and the Berry phase factor of (-1) acquired upon circling the vortex. This phase is encoded in the antiperiodic boundary conditions imposed on quasiparticles in our chosen gauge (see Appendix 3.2 for details). In this section, we neglect the superflow by setting $P_s = 0$ and consider only the Berry phase contribution. That is, we consider the scattering of quasiparticles due only to the presence of antiperiodic boundary conditions. Furthermore, we neglect the anisotropy of the Dirac dispersion and take $v_f = v_2$ ($\alpha = 1$). As we shall see, the antiperiodic boundary conditions yield the Aharonov-Bohm interference effect of an enclosed π-flux citedurstthesis,sriramberry.

We consider the isotropic Dirac Hamiltonian

$$H = v_f \left[\tau_3 p_x + \tau_1 p_y \right] \tag{3.23}$$

and seek solutions to the Bogoliubov-de Gennes equation, $H\Phi = E\Phi$. We express the quasiparticle wave function as a linear combination of angular momentum eigenstates which satisfy $J\Phi_\mu = \mu\Phi_\mu$. Since we have neglected the superflow, there is no effective potential and the general solution is easily found to be

$$\Phi = \sum_\mu \left[(A_\mu J_{\mu-\frac{1}{2}} + B_\mu Y_{\mu-\frac{1}{2}}) e^{i(\mu-\frac{1}{2})\phi} \begin{pmatrix} 1 \\ i \end{pmatrix} + i(A_\mu J_{\mu+\frac{1}{2}} + B_\mu Y_{\mu+\frac{1}{2}}) e^{i(\mu+\frac{1}{2})\phi} \begin{pmatrix} 1 \\ -i \end{pmatrix} \right] \quad (3.24)$$

where A_μ and B_μ are complex constants and $J_{\mu\pm\frac{1}{2}}$ and $Y_{\mu\pm\frac{1}{2}}$ are Bessel functions of argument $\rho = kr$. However, rather than imposing periodic boundary conditions by requiring that $\mu = n + 1/2$ with $n =$ integer, here we shall impose antiperiodic boundary conditions,

$$\Phi(r, \phi + 2\pi) = -\Phi(r, \phi) \quad (3.25)$$

by requiring that $\mu =$ integer. The radial functions are therefore half-integer Bessel functions rather than integer Bessel functions. The coefficients, A_μ and B_μ, are determined by satisfying boundary conditions at both long and short distances.

At long distances, we require an asymptotic wave function that is equal to the sum of an incident plane wave, Φ_i, and an outgoing radial wave, Φ_s. In terms of the current functional discussed in Appendix 3.2, $\mathbf{j}[\Phi] = v_f \Phi^\dagger(\tau_3 \hat{\mathbf{x}} + \tau_1 \hat{\mathbf{y}})\Phi$, we require that $\mathbf{j}[\Phi_i] \sim \hat{\mathbf{k}}$ and $\mathbf{j}[\Phi_s] \sim \hat{\mathbf{r}}$. In the presence of antiperiodic boundary conditions, we seek an incident wave of the form

$$\Phi_i(\mathbf{r}) = e^{i\gamma\frac{\varphi}{2}} e^{i\mathbf{k}\cdot\mathbf{r}} \begin{pmatrix} \cos\frac{\theta}{2} \\ \sin\frac{\theta}{2} \end{pmatrix} \qquad \gamma = \pm 1 \quad (3.26)$$

and a scattered wave of the form

$$\Phi_s(\mathbf{r}) = f(\varphi)\frac{e^{ikr}}{\sqrt{r}} \begin{pmatrix} \cos\frac{\phi}{2} \\ \sin\frac{\phi}{2} \end{pmatrix} \quad (3.27)$$

where $\mathbf{k} = (k, \theta)$, $\mathbf{r} = (r, \phi)$, and $\varphi = \phi - \theta$. In analogy with the problem of Aharonov-Bohm [74] scattering from an enclosed magnetic flux, we can say that $\gamma = -1$ corresponds to an effective π-flux while $\gamma = +1$ corresponds to an effective $(-\pi)$-flux. Since these two cases are equivalent, the choice of $\gamma = \pm 1$ is arbitrary. In the asymptotic limit, the half-integer Bessel functions take the form

$$J_{\mu-\frac{1}{2}}(\rho) = \eta_\mu \sqrt{\frac{2}{\pi\rho}} \cos(\rho - |\mu|\pi/2) \qquad Y_{\mu-\frac{1}{2}}(\rho) = \eta_\mu \sqrt{\frac{2}{\pi\rho}} \sin(\rho - |\mu|\pi/2) \tag{3.28}$$

where $\eta_\mu = 1$ for $\mu > 0$ and $\eta_\mu = (-1)^\mu$ for $\mu \leq 0$. Proceeding along the lines of Ref. [1], we can plug these asymptotic expressions into Eq. (3.24), reorganize terms, and thereby obtain a suggestive (yet still general) form for the quasiparticle wave function. Doing so, we find that

$$\Phi = e^{i\gamma\frac{\varphi}{2}} e^{i\mathbf{k}\cdot\mathbf{r}} \begin{pmatrix} \cos\frac{\theta}{2} \\ \sin\frac{\theta}{2} \end{pmatrix} + f(\varphi)\frac{e^{ikr}}{\sqrt{r}} \begin{pmatrix} \cos\frac{\phi}{2} \\ \sin\frac{\phi}{2} \end{pmatrix} - i\gamma g(\varphi)\frac{e^{-ikr}}{\sqrt{r}} \begin{pmatrix} -\sin\frac{\phi}{2} \\ \cos\frac{\phi}{2} \end{pmatrix} \tag{3.29}$$

where

$$f(\varphi) \equiv \sqrt{\frac{2}{\pi k}} \sum_\mu b_\mu e^{i\mu\varphi} \qquad g(\varphi) \equiv \sqrt{\frac{2}{\pi k}} \sum_\mu a_\mu e^{i\mu\varphi} \tag{3.30}$$

and a_μ and b_μ are complex constants defined via

$$A_\mu - iB_\mu \equiv i^\mu e^{-i\mu\theta} \left(e^{-i\frac{\pi}{4}}/2 + b_\mu\right) \tag{3.31}$$

$$A_\mu + iB_\mu \equiv -\gamma i^\mu e^{-i\mu\theta} \left(e^{i\frac{\pi}{4}}/2 + (-1)^\mu a_\mu\right). \tag{3.32}$$

If the plane wave is to be the only incident wave, we must eliminate the incident radial wave by requiring that $a_\mu = 0$ for all μ. With this restriction, B_μ and b_μ are related to A_μ via

$$B_\mu = i\left(A_\mu + i\gamma\ A_\mu^0\right) \qquad b_\mu = e^{-i\frac{\pi}{4}} \left(\frac{A_\mu}{A_\mu^0} - \frac{1 - i\gamma}{2}\right) \tag{3.33}$$

where $A_\mu^0 \equiv i^{\mu-1/2} e^{-i\mu\theta}/2$. The asymptotic wave function then takes the de-

sired form

$$\Phi = e^{i\gamma\frac{\varphi}{2}} e^{i\mathbf{k}\cdot\mathbf{r}} \begin{pmatrix} \cos\frac{\theta}{2} \\ \sin\frac{\theta}{2} \end{pmatrix} + f(\varphi)\frac{e^{ikr}}{\sqrt{r}} \begin{pmatrix} \cos\frac{\phi}{2} \\ \sin\frac{\phi}{2} \end{pmatrix} \tag{3.34}$$

and the differential cross section is given by

$$\frac{d\sigma}{d\varphi} = |f(\varphi)|^2 = \frac{2}{\pi k}\left|\sum_\mu b_\mu e^{i\mu\varphi}\right|^2 . \tag{3.35}$$

We can now determine the b_μ by imposing appropriate boundary conditions at the origin. As discussed in Ref. [1], the most restrictive condition is that the current through the origin (a point of zero area) must be zero. More precisely, we consider a semicircle of radius ϵ, oriented about the $\hat{\theta}$ direction, and require that the total current passing through it, I_θ, vanish as $\epsilon \to 0$. If $\Phi(\rho \to 0) \sim \rho^\alpha$, then $I_\theta \sim \epsilon^{2\alpha+1}$. Thus, to ensure that I_θ does not diverge at the origin, we must eliminate all terms in Eq. (3.24) which diverge faster than $\rho^{-1/2}$ as $\rho \to 0$. Since the half-integer Bessel functions exhibit the small-argument behavior, $J_{\mu\pm\frac{1}{2}} \sim \rho^{\mu\pm\frac{1}{2}}$ and $Y_{\mu\pm\frac{1}{2}} \sim \rho^{-\mu\mp\frac{1}{2}}$, this clearly requires that

$$B_\mu = 0 \text{ for } \mu > 0 \qquad A_\mu = 0 \text{ for } \mu < 0 \tag{3.36}$$

The condition for $\mu = 0$ is more subtle. Enforcing the above, the resulting wave function is dominated, as $\rho \to 0$, by the terms which diverge exactly as $\rho^{-1/2}$. We therefore find that

$$\Phi(\rho \to 0) = \sqrt{\frac{2}{\pi\rho}}\left[(A_0 - iB_0)\begin{pmatrix} \cos\frac{\theta}{2} \\ \sin\frac{\theta}{2} \end{pmatrix} + i(A_0 + iB_0)\begin{pmatrix} -\sin\frac{\theta}{2} \\ \cos\frac{\theta}{2} \end{pmatrix}\right]. \tag{3.37}$$

From Eq. (3.33), we know that $A_0 + iB_0 = -i\gamma A_0^0$ where $A_0^0 = e^{-i\pi/4}/2$. Furthermore, we can define a complex constant, β, such that $A_0 - iB_0 \equiv -i\gamma A_0^0\beta$. With this definition, the current density near the origin takes the form

$$\mathbf{j}(\rho \to 0) = \frac{v_f}{2\pi\rho}\left[\left(|\beta|^2 - 1\right)\hat{r} + 2\,\mathrm{Im}[\beta]\hat{\phi}\right]. \tag{3.38}$$

Explicitly computing the current through the origin, we find that

$$I_\theta = \lim_{\epsilon\to 0}\int_{\theta-\pi/2}^{\theta+\pi/2} \epsilon\, d\phi\, \mathbf{j}(\epsilon)\cdot\hat{\theta} = v_f \int \frac{d\phi}{2\pi}\left[\left(|\beta|^2-1\right)\hat{r}\cdot\hat{\theta} + 2\,\mathrm{Im}[\beta]\hat{\phi}\cdot\hat{\theta}\right] \quad (3.39)$$

which must be set to zero for all directions $\hat{\theta}$. This requires that $\beta = \pm 1$.

Putting everything together yields the values of our original coefficients

$$A_\mu = -i\gamma A_\mu^0 \left\{ \begin{array}{cc} 1 & \mu > 0 \\ \frac{1+\beta}{2} & \mu = 0 \\ 0 & \mu < 0 \end{array} \right\} \qquad B_\mu = -\gamma A_\mu^0 \left\{ \begin{array}{cc} 0 & \mu > 0 \\ \frac{1-\beta}{2} & \mu = 0 \\ 1 & \mu < 0 \end{array} \right\} \quad (3.40)$$

where $\gamma = \pm 1$ and $\beta = \pm 1$. The Z_2 ambiguity in γ and β is a consequence of the equivalence of a π-flux with a $(-\pi)$-flux, which cannot affect observable quantities. For $\beta = \gamma = \pm 1$,

$$b_\mu = \frac{1}{\sqrt{2}} \left\{ \begin{array}{cc} i & \gamma\mu > 0 \\ -1 & \gamma\mu \leq 0 \end{array} \right\}. \quad (3.41)$$

Plugging this into Eq. (3.35) and summing over μ (with a convergence factor $e^{-|\mu|0^+}$), yields

$$\frac{d\sigma}{d\varphi} = \frac{1}{2\pi k\,\sin^2(\varphi/2)} - \gamma\frac{2}{k}\frac{\delta(\varphi)}{\varphi}. \quad (3.42)$$

The same result is obtained for $\beta = -\gamma$. Note, however, that the above is only valid for $\varphi \neq 0$. As discussed (for the electron scattering case) in the original paper by Aharonov and Bohm [74], as well as in an excellent review by Olariu and Popescu [75], our asymptotic approximations are only valid away from the forward direction. Thus, the second term above, which is only nonzero for $\varphi = 0$ and is an artifact of our casual treatment of the forward direction, can be dropped. (For a detailed treatment of the Aharonov-Bohm scattering of an electron in the forward direction, see the paper by Stelitano [76]. Our differential cross section therefore takes the form

$$\frac{d\sigma}{d\varphi} = \frac{1}{2\pi k\,\sin^2(\varphi/2)} \quad (3.43)$$

which is exactly the differential cross section for the Aharonov-Bohm scattering of an electron from an enclosed π-flux. As expected, this result is independent of our choice of $\gamma = \pm 1$ and $\beta = \pm 1$ and is the same for quasiparticles about any of the four gap nodes. Due to the infinite range of the Berry phase effect, the total cross section diverges. However, the transport cross section is finite and given by $\sigma_{\parallel} = 1/\pi k$. Since left-right symmetry is not broken in the absence of a superflow, the skew cross section is zero. In the zero-superflow case considered above, it was easy enough to neglect the subtleties associated with forward scattering in the presence of antiperiodic boundary conditions. However, if we were to consider the superflow and the Berry phase effects together, it would be necessary to treat such nuances more carefully. The first step towards that is to regularize the calculation of the cross section due to the Berry phase effect. This is the goal of the remainder of this chapter.

3.4 Regularization of Berry Phase in Double vortex Setup

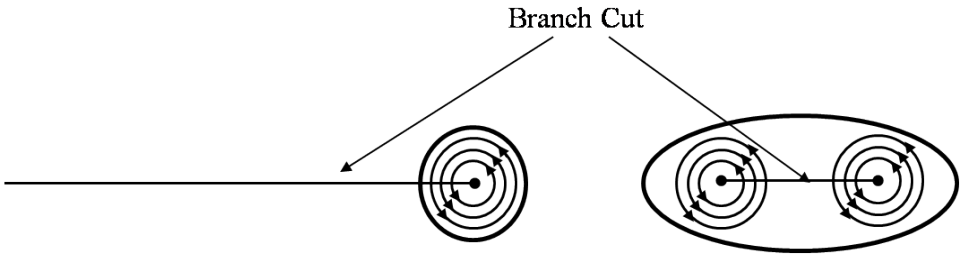

Figure 3.2: Single vortex with semi-infinite branch cut and double vortex with finite branch cut due to the Berry phase

The infinite range of the Berry phase effect is solely due to the isolated treatment of the single vortex (see Fig. 3.2). In reality these vortices are not isolated and the Berry phase effect terminates at the neighboring vortices, thereby resulting in a finite branch cut. The simplest object containing a finite branch cut is a pair of vortices separated by some distance as shown in Fig. 3.2. Elliptical coordinates are a natural setting for studying two-center

problems. We define elliptical coordinates via

$$x = R \cosh\mu \cos\nu \tag{3.44}$$

$$y = R \sinh\mu \sin\nu \tag{3.45}$$

The presence of a finite branch cut between the two vortex cores can be imposed as a boundary condition at $\mu = 0$ (line separating foci) on the full wavefunction spinor in the following way

$$\psi(\mu, -\nu) \mid_{\mu=0} = (-1)^B \ \psi(\mu, \nu) \mid_{\mu=0} \tag{3.46}$$

The parameter B is defined to take values 0 or 1. For B=0, there is no branch cut between the pair of vortices (or foci) and the condition reduces to a trivial continuity condition at $\mu = 0$ of the elliptical coordinate system. Setting B=1, we turn on the Berry phase effect via non-trivial boundary condition. The presence of the branch cut captures the fact that when a quasiparticle passes between the vortex cores, it acquires a phase factor of (-1), which on its own can scatter quasiparticles. Our task for the rest of this work is to capture the scattering of quasiparticles due to a finite branch cut between two vortices. We will follow the same prescription that we applied to the single vortex case to calculate the scattering cross section. The first step is to separate the (2+1)d Dirac equation in elliptical coordinates. The second step is to solve the separated equations to get the eigenfunctions for the separation parameter. the third step is to construct the incoming plane wave and the outgoing scattered wave in terms of phase shifts from the separated eigenfunctions. The fourth and final step is to impose the boundary condition for the branch cut on the full wavefunction spinor and calculate the scattering amplitude and differential scattering cross section.

3.5 Separation of the Dirac equation in Elliptical Coordinates

In this section we separate the Dirac equation in elliptical coordinates [55]. The detailed calculation for separation of variables can be found in Appendix A.1. The dirac equation in (2+1)d is given as

$$[\gamma^0\partial_t + \gamma^1\partial_x + \gamma^2\partial_y]\psi = 0 \tag{3.47}$$

We define the Dirac matrix representation to be $\gamma^0 = \tau_2$, $\gamma^1 = i\tau_1$ and $\gamma^2 = -i\tau_3$, where τ_i's are the Pauli matrices. We define elliptical coordinates via

$$x = f(\mu,\nu) = R\,\cosh\mu\,\cos\nu \tag{3.48}$$

$$y = g(\mu,\nu) = R\,\sinh\mu\,\sin\nu \tag{3.49}$$

Here μ is the radial coordinate and ν is the angular coordinate. Here, we directly define the transformations that separate the Dirac equation in elliptical coordinates and leave the rigorous details to Appendix A.1.

$$TS^{-1}[\gamma^0\partial_t + \frac{\widetilde{\gamma}^1(\mu,\nu)}{h}\partial_\mu + \frac{\widetilde{\gamma}^2(\mu,\nu)}{h}\partial_\nu]ST(ST)^{-1}\psi = 0 \tag{3.50}$$

The product of transformation matrices S and T can be explicitly written out as

$$ST = \frac{1}{(\cosh\,\mu + \cos\,\nu)}\begin{pmatrix} \cos\,\frac{\nu}{2}\cosh\,\frac{\mu}{2} & -\sin\,\frac{\nu}{2}\sinh\,\frac{\mu}{2} \\ \sin\,\frac{\nu}{2}\sinh\,\frac{\mu}{2} & \cos\,\frac{\nu}{2}\cosh\,\frac{\mu}{2} \end{pmatrix} \tag{3.51}$$

$$\psi = ST\,Y \tag{3.52}$$

Y is the transformed wavefunction spinor and is given by

$$Y = \begin{pmatrix} \alpha(\mu)B(\nu) \\ i\beta(\mu)A(\nu) \end{pmatrix} \tag{3.53}$$

Each component of Y satisfies separable second order equation. We define a separation constant λ^2 such that

$$
\begin{aligned}
(\partial_\nu^2 - ikR\cos\nu + k^2R^2\sin^2\nu + \lambda^2)A(\nu) &= 0 && (3.54)\\
(\partial_\nu^2 + ikR\cos\nu + k^2R^2\sin^2\nu + \lambda^2)B(\nu) &= 0 && (3.55)\\
(\partial_\mu^2 - ikR\cosh\mu + k^2R^2\sinh^2\mu - \lambda^2)\alpha(\mu) &= 0 && (3.56)\\
(\partial_\mu^2 + ikR\cosh\mu + k^2R^2\sinh^2\mu - \lambda^2)\beta(\mu) &= 0 && (3.57)
\end{aligned}
$$

which is equivalent to four coupled first-order equations that connect the upper and lower components of the wave function spinor

$$
\begin{aligned}
(\partial_\nu - ikR\sin\nu)A(\nu) &= i\lambda B(\nu) && (3.58)\\
(\partial_\nu + ikR\sin\nu)B(\nu) &= i\lambda A(\nu) && (3.59)\\
(\partial_\mu - ikR\sinh\mu)\alpha(\mu) &= \lambda\beta(\mu) && (3.60)\\
(\partial_\mu + ikR\sinh\mu)\beta(\mu) &= \lambda\alpha(\mu) && (3.61)
\end{aligned}
$$

The separated equations Eq. (3.54), (3.55), (3.56), and (3.57) are known as the radial and angular Whittaker Hill equations (WHE) and the upper and lower components of the spinor are connected via first order coupled equations.

3.6 Solutions to the Whittakker Hill Equation (WHE)

We transform the radial and angular WHE by using the following functional transform,

$$A(\nu) = y_1 e^{-ikR\cos\nu} \tag{3.62}$$

where y_1 satisfies the differential equation known as the Ince equation [58–60, 65] .

$$y_1'' + 2ikR\sin\nu\, y_1' + \lambda^2 y_1 = 0 \tag{3.63}$$

We do similar transformations for the radial WHE

$$\alpha(\mu) = x_2 e^{ikR\,\cosh\,\mu} \tag{3.64}$$

to obtain

$$x_2^{''} + 2ikR\sinh\,\mu\, x_2^{'} - \lambda^2 x_2 = 0 \tag{3.65}$$

$B(\nu)$ and $\beta(\mu)$ are calculated from the first-order coupled equations. Now we will try to solve all the Ince equations as an eigenvalue problem using a matrix method. We write a general form of the Ince equation from which we can deduce Ince equations (3.63) and (3.65) and try to find the recursions for the general equation [58].

$$\frac{d^2\psi}{d\theta^2} + 2i\,\omega\,\sin\,\theta\frac{d\psi}{d\theta} + (\lambda^2 + \omega(\rho + i)\cos\,\theta)\psi = 0 \tag{3.66}$$

$\psi = y_1$, $\theta = \nu$, $\rho = -i$ and $\omega = kR$ will yield Eq. (3.63).

$\psi = x_2$, $\theta = i\mu$, $\rho = -i$ and $\omega = -kR$ will yield Eq. (3.65).

3.6.1 Solutions to angular WHE (Matrix method)

As often happens in the solution of differential equations with periodic coefficients, the solutions fall into four classes corresponding to the four types of Fourier series. They may be even or odd functions of θ and may have 2π as their period or antiperiod. The four possible solutions to Eq. (3.66) are

$$\psi_m^1(\theta) = \sum_{r=0}^{\infty} a_{mr}\,\cos r\theta, \qquad \psi_m^2(\theta) = \sum_{r=0}^{\infty} b_{mr}\,\sin r\theta \tag{3.67}$$

$$\psi_m^3(\theta) = \sum_{r=0}^{\infty} a_{mr}\,\cos(r+\frac{1}{2})\theta, \qquad \psi_m^4(\theta) = \sum_{r=0}^{\infty} b_{mr}\,\sin(r+\frac{1}{2})\theta \tag{3.68}$$

We know that the full wave function has to have 2π periodicity in ν. In order to obtain this we have to choose the solutions of the Ince equations to be 2π antiperiodic in ν. This is so because the transformation matrix (ST) multiplying the wave function spinor is 2π antiperiodic in ν (see Appendix A.1

for details of the transformation matrix),and hence the product of antiperiodic spinor and antiperiodic transformation matrix will yield 2π periodicity in ν. Hence the possible solutions are Eq. (3.68). Now we substitute these solutions in Eq. (3.66) and get recursion relations for the coefficients. Reducing WHE to Ince equations has the advantage that the Ince equation has only three term recursion relations as opposed to the five term recursions for WHE. The eigenvalue equation for the even solution is

$$\begin{aligned} a_0(\lambda e^2 - \frac{1}{4} + \frac{\omega\rho}{2}) + a_1\frac{\omega}{2}(\rho - 2i) &= 0\,(r=0) \\ \frac{\omega}{2}(\rho + 2r\,i)a_{r-1} + (\lambda e^2 - (r+\frac{1}{2})^2)a_r + \frac{\omega}{2}(\rho - 2(r+1)i)a_{r+1} &= 0\,(r \geq 1) \end{aligned} \tag{3.69}$$

The eigenvalue equation for the odd solution is

$$\begin{aligned} b_0(\lambda o^2 - \frac{1}{4} - \frac{\omega\rho}{2}) + b_1\frac{\omega}{2}(\rho - 2i) &= 0 \quad (r=0) \\ \frac{\omega}{2}(\rho + 2r\,i)b_{r-1} + (\lambda o^2 - (r+\frac{1}{2})^2)b_r + \frac{\omega}{2}(\rho - 2(r+1)i)b_{r+1} &= 0 \qquad (r \geq 1) \end{aligned} \tag{3.70}$$

We can see that the coefficients of a_0 and b_0 are different in the recursions for even and odd parity solutions. This implies that the cosine-type series solution and sine-series solution have different eigenvalues (λe_m^2 and λo_m^2 where m is the eigenvalue index) and they turn out to be complex conjugates of each other. The complex eigenvalue is a consequence of the non-Hermiticity of the Whittaker Hill equation. These recursions can be written in a matrix form. The solutions can be expressed as an infinite trigonometric series and we may truncate it at a point where the extra terms are not significant. We can obtain the eigenvalues and eigenvectors of the matrix which will provide the complete solutions to the Ince equations that are used in the solution to Whittaker Hill

equations. Summarizing the angular solutions we can write

$$Ae_m(\nu) = e^{-ikR\cos\nu}\sum_{r=0}^{\infty} a_{mr}\cos(r+\frac{1}{2})\nu \tag{3.71}$$

$$Ao_m(\nu) = e^{-ikR\cos\nu}\sum_{r=0}^{\infty} b_{mr}\sin(r+\frac{1}{2})\nu \tag{3.72}$$

$Ae_m(\nu)$ and $Ao_m(\nu)$ are solutions for the angular factor of the lower component of the separated spinor. Using the first order coupled equation (3.58) we can obtain the upper component angular eigenfunctions,

$$Be_m(\nu) = \frac{1}{i\lambda e_m}(\partial_\nu - ikR\sin\nu)Ae_m(\nu) \tag{3.73}$$

$$Bo_m(\nu) = \frac{1}{i\lambda o_m}(\partial_\nu - ikR\sin\nu)Ao_m(\nu) \tag{3.74}$$

$Be_m(\nu)$ and $Bo_m(\nu)$ are of the opposite parity to $Ae_m(\nu)$ and $Ao_m(\nu)$ due to the above operation and are given as

$$Be_m(\nu) = \frac{1}{i\lambda e_m}e^{-ikR\cos\nu}\sum_{r=0}^{\infty} a_{mr}(-r-\frac{1}{2})\sin(r+\frac{1}{2})\nu \tag{3.75}$$

$$Bo_m(\nu) = \frac{1}{i\lambda o_m}e^{-ikR\cos\nu}\sum_{r=0}^{\infty} b_{mr}(r+\frac{1}{2})\cos(r+\frac{1}{2})\nu \tag{3.76}$$

Note that for the sake of notation, we always classify eigenfunctions according to the eigenvalues λe_m^2 and λo_m^2. Functions corresponding to λe_m^2 get the suffix "e" and corresponding to λo_m^2 get the suffix "o".

3.6.2 Solutions to the radial WHE

Since we have obtained the eigenvalues by solving the angular equations, the eigenvalues can be used as parameters in the radial differential equations.

The first method to evaluate the radial solutions is to replace $\nu \to i\mu$ and $(kR \to -kR)$ in the angular solutions (which is the same transformation that connects radial and angular WHE), the regular periodic (in $i\mu$) solutions are

denoted by Je and Jo.

$$Je_m(\mu) = e^{ikR\cosh\mu} \sum_{r=0}^{\infty} c_{mr} \sinh(r+\frac{1}{2})\mu \tag{3.77}$$

$$Jo_m(\mu) = e^{ikR\cosh\mu} \sum_{r=0}^{\infty} d_{mr} \cosh(r+\frac{1}{2})\mu \tag{3.78}$$

The lower component of the spinor can be obtained from coupled radial Eqs. (3.60) and (3.61). We denote the lower component radial solution with primes and keep this notation for all the lower component radial solutions. Note that prime does not imply derivative but is defined by the following operator acting on the upper component solutions.

$$Je'_m(\mu) = \frac{1}{\lambda e_m}(\partial_\mu - ikR\sinh\mu)Je_m(\mu) \tag{3.79}$$

$$Jo'_m(\mu) = \frac{1}{\lambda o_m}(\partial_\mu - ikR\sinh\mu)Jo_m(\mu) \tag{3.80}$$

The second linearly independent solution that is non-periodic in $(i\mu)$ is given as

$$Ne_m(\mu) = C^e_m(kR)\mu Je_m(\mu) + C^e_m(kR)\sum_{r=0}^{\infty} f_{mr} \cosh(r+\frac{1}{2})\mu \tag{3.81}$$

$$No_m(\mu) = C^o_m(kR)\mu Jo_m(\mu) + C^o_m(kR)\sum_{r=0}^{\infty} g_{mr} \sinh(r+\frac{1}{2})\mu \tag{3.82}$$

where the presence of factor of μ ensures the non-periodicity of the second solutions in $i\mu$. Note that it is of opposite parity to the regular Je and Jo. This approach is similar to the calculation of non-periodic second solutions of the modified Mathieu equation [77]. $C^{e,o}_m(kR)$ are the normalization constants.

The second method to calculate the radial solutions is the power series method. In this method we simply do a power series analysis in μ for the second order radial Ince equation (3.65) (note that such solutions do not capture the complex periodicity of the hyperbolic functions). We then immediately get the two independent solutions of even and odd parity with the predetermined

eigenvalues from the angular solutions acting as a parameter characterizing the different radial solutions.

$$Je_m(\mu) = e^{ikR\cosh\mu}\sum_{r=0}^{\infty} c_r\,\mu^{2r+1}\ , \quad Ne_m(\mu) = e^{ikR\cosh\mu}\sum_{r=0}^{\infty} f_r\,\mu^{2r} \tag{3.83}$$

$$Jo_m(\mu) = e^{ikR\cosh\mu}\sum_{r=0}^{\infty} d_r\,\mu^{2r}, \quad No_m(\mu) = e^{ikR\cosh\mu}\sum_{r=0}^{\infty} g_r\,\mu^{2r+1} \tag{3.84}$$

We are interested in studying the scattering problem which requires the radial solutions to have a well-defined asymptotic form. We can evaluate the radial solutions as power series in μ and in series of $\sinh\mu$ and $\cosh\mu$ as described in the above mentioned methods. But these forms of solution diverge at large μ and therefore do not yield proper asymptotic forms. Fortunately, the radial solutions to Whittaker Hill equations can be written as series of confluent hypergeometric functions [61–63, 66] which converge for all μ. We follow the procedure described in Ref. ([61]),and start with radial Ince equation (3.65)

$$\alpha^{''}(\mu) + 2ikR\sinh\,\mu\,\alpha^{'}(\mu) - \lambda^2\alpha(\mu) = 0 \tag{3.85}$$

and then make the transformation $z = \cosh^2\frac{\mu}{2}$. The resulting equation takes the form

$$z(z-1)\alpha^{''}(z) + (4ikR\ z^2 - 4ikR\ z + z - \frac{1}{2})\alpha^{'}(z) - \lambda^2\alpha(z) = 0 \tag{3.86}$$

To extract the even and odd parity of solutions, we make the following functional transformations to the above equation,

$$\alpha(z) = \sqrt{z}\ \alpha e(z)\ \text{(for even parity)},\ \alpha(z) = \sqrt{z-1}\ \alpha o(z)\ \text{(for odd parity)} \tag{3.87}$$

Making these transformations, we get the following differential equations for

$\alpha e(z)$ and $\alpha o(z)$.

$$\begin{aligned} z(z-1)\alpha e^{''}(z) &+ \frac{1}{2}(8ikR\ z(z-1)+4z-3)\alpha e^{'}(z) \\ &+ (2ikR\ (z-1)+\frac{1}{4}-\lambda e^2)\alpha e(z)=0 \qquad (3.88) \\ z(z-1)\alpha o^{''}(z) &+ \frac{1}{2}(8ikR\ z(z-1)+4z-1)\alpha o^{'}(z) \\ &+ (2ikR\ (z)+\frac{1}{4}-\lambda o^2)\alpha o(z)=0 \qquad (3.89) \end{aligned}$$

We have classified the eigenvalues as λe^2 and λo^2 for the even parity solutions and the odd parity solutions respectively (we know the eigenvalues from the angular eigenvalue Eqs. (3.69,3.69) and Eqs. (3.70,3.70). Solutions to the above equations can be expressed in terms of confluent hypergeometric functions

$$\begin{aligned} \alpha e_m(z) &= \sum_{n=0}^{\infty} c^e_{m\ n}\, M(n+1/2, n+2, -4ikR\ z) \qquad (3.90) \\ \alpha o_m(\mu) &= \sum_{n=0}^{\infty} c^o_{m\ n}\, M(n+1/2, n+2, -4ikR\ z) \qquad (3.91) \end{aligned}$$

where the M are the regular hypergeometric functions satisfying the Kummer differential equation [78]

$$zM''(z)+(b-z)M'(z)-aM(z)=0 \qquad (3.92)$$

The three term recursion relations for the coefficients c^e_m and c^o_m are

$$\begin{aligned} c^e_{m\ n-1}4ikR(n-\frac{1}{2})^2 &+ c^e_{m\ n}[n(n+1)+4ikR\ n+\frac{1}{4}-\lambda e^2_m] \\ &+ (n+1)c^e_{m\ n+1}=0 \qquad (3.93) \\ c^o_{m\ n-1}4ikR(n-\frac{1}{2})(n+\frac{1}{2}) &+ c^o_{m\ n}[n(n+1)+4ikR\ (n+\frac{1}{2})+\frac{1}{4}-\lambda o^2_m] \\ &+ (n+1)c^o_{m\ n+1}=0 \qquad (3.94) \end{aligned}$$

and the full solution to the radial WHE (from the solution to the Ince equation)

can be written as

$$Jo_m(\mu) = e^{ikR\cosh\mu}\sqrt{\cosh^2\frac{\mu}{2}}\sum_{n=0}^{\infty} c^e_{m\ n}\, M(n+\frac{1}{2}, n+2, -4ikR\cosh^2\frac{\mu}{2}) \tag{3.95}$$

$$Je_m(\mu) = e^{ikR\cosh\mu}\sqrt{\cosh^2\frac{\mu}{2}-1}\sum_{n=0}^{\infty} c^o_{m\ n}\, M(n+\frac{1}{2}, n+2, -4ikR\cosh^2\frac{\mu}{2}) \tag{3.96}$$

The second linearly independent solution can be obtained from the first solution using the following method,

$$Fey_m(\mu) = Je_m(\mu)\int_{\mu_0}^{\mu}\frac{1}{Je_m(\mu')^2}d\mu' \tag{3.97}$$

$$Gey_m(\mu) = Jo_m(\mu)\int_{\mu_0}^{\mu}\frac{1}{Jo_m(\mu')^2}d\mu' \tag{3.98}$$

Fey and Gey are the second linearly independent solutions corresponding to Je and Jo. The lower component of the spinor can be evaluated by using the coupled equations (3.60).

$$Fey'_m(\mu) = \frac{1}{\lambda e_m}(\partial_\mu - ikR\sinh\mu)Fey_m(\mu) \tag{3.99}$$

$$Gey'_m(\mu) = \frac{1}{\lambda o_m}(\partial_\mu - ikR\sinh\mu)Gey_m(\mu) \tag{3.100}$$

$$\tag{3.101}$$

Solutions to the radial WHE for both upper component ($\alpha e_m(\mu)$, $\alpha o_m(\mu)$) and lower component ($\beta e_m(\mu)$, $\beta o_m(\mu)$) can be summarized in the combination of

two linearly independent solutions as,

$$\begin{aligned}
\alpha e_m(\mu) &= A^e_m Je_m(\mu) + B^e_m Fey_m(\mu) && (3.102)\\
\beta e_m(\mu) &= A^e_m Je'_m(\mu) + B^e_m Fey'_m(\mu)) && (3.103)\\
\alpha o_m(\mu) &= A^o_m Jo_m(\mu) + B^o_m Gey_m(\mu) && (3.104)\\
\beta o_m(\mu) &= A^o_m Jo'_m(\mu) + B^o_m Gey'_m(\mu)) && (3.105)
\end{aligned}$$

$A^e_m,\ B^e_m$ and $A^o_m,\ B^o_m$ are the undetermined coefficients and for notation sake we classify undetermined coefficients according to eigenvalues corresponding to λe^2_m or λo^2_m. We identify undetermined coefficients with superscript "e" and "o" corresponding to the eigenvalues. A normalized choice for the undetermined coefficients would be

$$\begin{aligned}
A^e_m &= \cos\delta^e_m \qquad A^o_m = \cos\delta^o_m && (3.106)\\
B^e_m &= \sin\delta^e_m \qquad B^o_m = \sin\delta^o_m && (3.107)
\end{aligned}$$

Such a choice is helpful in formulating the scattering cross section in terms of phase shifts in the scattering amplitude with δ^e_m an δ^o_m being the phase shifts.

Armed with all the solutions to the individual components of the separated Dirac spinor, we can now write the full solution to the free Dirac equation as a superposition of all the eigenstates of the separated equations

$$\psi(\mu,\nu) = (ST)\sum_m \begin{pmatrix} \alpha e_m(\mu) Be_m(\nu) + \alpha o_m(\mu) Bo_m(\nu) \\ i(\beta e_m(\mu) Ae_m(\nu) + \beta o_m(\mu) Ao_m(\nu)) \end{pmatrix} \qquad (3.108)$$

3.7 Expansion of Incoming Plane Wave Spinor in terms of Whittaker Hill Eigenfunctions

The form of the incoming plane wave (see Appendix 3.2 Eq. (3.19)) is given as $e^{i\,\vec{k}\cdot\vec{r}}\begin{pmatrix}\cos\frac{\theta}{2}\\ \sin\frac{\theta}{2}\end{pmatrix}$ (θ is the angle of incidence of the quasiparticle current). One of the requirements to construct the scattering cross section is to expand the incident plane wave in terms of eigenfunctions of the free Dirac equation which

satisfy the following continuity condition (3.109) at $\mu = 0$.

$$\psi(\mu, -\nu) \mid_{\mu=0} = \psi(\mu, \nu) \mid_{\mu=0} \tag{3.109}$$

To write the plane wave expansion we take the following path. We write the free solution of the Dirac equation in elliptical coordinates as a linear combination of the eigenstates. One specific superposition of these eigenstates represents the plane wave spinor. Our aim in this section is to obtain these linear combination coefficients which represent the plane wave spinor. We can see that applying condition (3.109) to $\psi(\mu, \nu)$ is the same as applying it to $Y(\mu, \nu)$ (see Eq. (3.53)). This is because the transformation matrix which connects ψ to Y cancels on both sides of the Eq. (3.109).

$$Y(\mu, -\nu) \mid_{\mu=0} = Y(\mu, \nu) \mid_{\mu=0} \tag{3.110}$$

Applying the above condition, we can find the following constraint on the two undetermined constants (per eigenstate) appearing in the radial solutions due to the overall parity of the eigenfunctions.

$$B_m^e = B_m^o = 0 \tag{3.111}$$

Thus we see that the radial functions with constraint at $\mu = 0$ do not depend on Fey, Gey . Hence, the plane wave term only has Je and Jo terms which is analogous to the plane wave expansion in terms of Bessel functions in polar coordinates (see Ref. [78]) which only contains regular J Bessel functions. Applying the appropriate boundary conditions on Y, we find the plane wave solution to be:

$$\psi = (ST) \sum_m \begin{pmatrix} (A_m^e Je_m Be_m(\nu) + A_m^o Jo_m Bo_m(\nu)) \\ (i\ A_m^e Je'_m Ae_m(\nu) + i\ A_m^o Jo'_m Ao_m(\nu)) \end{pmatrix} \tag{3.112}$$

The above solution with arbitrary constants A_m^e and A_m^o is an arbitrary superposition of eigenstates. We need to calculate the linear combination coefficients (as a function of θ) for which the expansion represents a plane wave spinor

(3.19). We write down the following expansion for the plane wave incident at an angle θ with respect to the x-axis. This step is important since we would like to control the angle of incidence of the incoming quasiparticle current.

$$\begin{aligned} e^{i\,\vec{k}\cdot\vec{r}} \begin{pmatrix} \cos\frac{\theta}{2} \\ \sin\frac{\theta}{2} \end{pmatrix} &= (ST)\Bigg\{ \sum_m n_m^e Be_m(\theta) \begin{pmatrix} Je_m Be_m \\ i\,Je_m^{'} Ae_m \end{pmatrix} \\ &+ \sum_m n_m^o Bo_m(\theta) \begin{pmatrix} Jo_m Bo_m \\ i\,Jo_m^{'} Ao_m \end{pmatrix} \Bigg\} \end{aligned} \tag{3.113}$$

For details of the calculation of the plane wave expansion coefficients n_m^e and n_m^o refer to Appendix A.3.

3.8 Scattering Amplitude and Phase Shifts

To study the scattering problem one requires well defined asymptotic forms of the full wavefunction spinor. The asymptotic form of the wavefunction determines the scattering amplitude in terms of the phase shifts of each partial wave with respect to the partial waves in the incident quasiparticle current. Thus, we consider the asymptotic limit $\mu \to \infty$ for the full wave function spinor $\psi = (ST\ )Y$,

$$\begin{aligned} \psi(\mu,\nu) &= \frac{1}{(\cosh\,\mu + \cos\,\nu)} \begin{pmatrix} \cos\,\frac{\nu}{2}\cosh\,\frac{\mu}{2} & -\sin\,\frac{\nu}{2}\sinh\,\frac{\mu}{2} \\ \sin\,\frac{\nu}{2}\sinh\,\frac{\mu}{2} & \cos\,\frac{\nu}{2}\cosh\,\frac{\mu}{2} \end{pmatrix} \\ &\times \sum_m \begin{pmatrix} \alpha e_m(\mu) Be_m(\nu) + \alpha o_m(\mu) Bo_m(\nu) \\ i(\beta e_m(\mu) Ae_m(\nu) + \beta o_m(\mu) Ao_m(\nu)) \end{pmatrix} \end{aligned} \tag{3.114}$$

. To proceed further, we need to use asymptotic forms for the radial functions. As $\mu \to \infty$, the asymptotic form (see Appendix A.2) for the radial functions

is given as

$$\alpha e_m(\mu) \sim \sqrt{\frac{1}{\pi kR}} e^{-i\frac{\pi}{4}} (\cos\delta_m^e + i\sin\delta_m^e) e^{i\frac{kR}{2}e^{\mu}} \tag{3.115}$$

$$\beta e_m(\mu) \sim \sqrt{\frac{1}{\pi kR}} e^{-i\frac{\pi}{4}} (\cos\delta_m^e - i\sin\delta_m^e) e^{-i\frac{kR}{2}e^{\mu}} \tag{3.116}$$

$$\alpha o_m(\mu) \sim \sqrt{\frac{1}{\pi kR}} e^{-i\frac{\pi}{4}} (\cos\delta_m^o + i\sin\delta_m^e) e^{i\frac{kR}{2}e^{\mu}} \tag{3.117}$$

$$\beta o_m(\mu) \sim \sqrt{\frac{1}{\pi kR}} e^{-i\frac{\pi}{4}} (\cos\delta_m^o - i\sin\delta_m^e) e^{-i\frac{kR}{2}e^{\mu}} \tag{3.118}$$

For compact notation, we can write $e^{\mu} = \frac{2r}{R}$, where R is half the distance between the foci of the elliptical coordinates and r is the polar radial coordinate in the limit where the angular elliptical coordinate ν approaches the polar angle ϕ. In large μ limit elliptical coordinates reduce to polar coordinates.

$$\alpha e_m(r) \sim \sqrt{\frac{1}{\pi kR}} e^{-i\frac{\pi}{4}} e^{i(kr+\delta_m^e)} \tag{3.119}$$

$$\beta e_m(r) \sim \sqrt{\frac{1}{\pi kR}} e^{-i\frac{\pi}{4}} e^{-i(kr+\delta_m^e)} \tag{3.120}$$

$$\alpha o_m(r) \sim \sqrt{\frac{1}{\pi kR}} e^{-i\frac{\pi}{4}} e^{i(kr+\delta_m^o)} \tag{3.121}$$

$$\beta o_m(r) \sim \sqrt{\frac{1}{\pi kR}} e^{-i\frac{\pi}{4}} e^{-i(kr+\delta_m^o)} \tag{3.122}$$

The asymptotic form of the ST transformation matrix can also be evaluated. As $\mu \to \infty$, $\cosh\mu + \cos\nu \sim \cosh\mu$ and $\cosh\mu \sim \sinh\mu \sim \frac{e^{\mu}}{2} = \frac{r}{R}$. Applying these limits in the ST matrix of Eq. (3.51) gives

$$ST \sim \frac{\sqrt{R}}{\sqrt{r}} \begin{pmatrix} \cos\frac{\nu}{2} & -\sin\frac{\nu}{2} \\ \sin\frac{\nu}{2} & \cos\frac{\nu}{2} \end{pmatrix} \tag{3.123}$$

We can then substitute the asymptotic forms of the radial solutions back into the full solution spinor of Eq. (3.108) to obtain

$$\begin{aligned}\psi &= (ST)\sqrt{\frac{1}{\pi kR}}e^{-i\frac{\pi}{4}}\sum_m \Bigg\{ e^{ikr}(e^{i\delta^e_m}Be_m(\nu)+e^{i\delta^o_m}Bo_m(\nu))\begin{pmatrix}1\\0\end{pmatrix} \\ &+ e^{-ikr}i(e^{-i\delta^e_m}Ae_m(\nu)+e^{-i\delta^o_m}Ao_m(\nu))\begin{pmatrix}0\\1\end{pmatrix}\Bigg\} \end{aligned} \tag{3.124}$$

We would like to write the full wave function in the two suggestive parts requisite to set up the scattering problem

$$\psi = \psi^{plane\,wave} + \psi^{scattered} \tag{3.125}$$

The plane wave expanded in terms of the separated eigenstates Eq. (3.113) in the large μ limit takes the form

$$\begin{aligned}\psi^{plane\,wave} &= (ST)\sqrt{\frac{1}{\pi kR}}e^{-i\frac{\pi}{4}}\sum_m e^{ikr}(n^e_m Be_m(\theta)Be_m(\nu) \\ &+ n^o_m Bo_m(\theta)Bo_m(\nu))\begin{pmatrix}1\\0\end{pmatrix} \\ &+ (ST)\sqrt{\frac{1}{\pi kR}}e^{-i\frac{\pi}{4}}\sum_m e^{-ikr}i(n^e_m Be_m(\theta)Ae_m(\nu) \\ &+ n^o_m Bo_m(\theta)Ao_m(\nu))\begin{pmatrix}0\\1\end{pmatrix} \end{aligned} \tag{3.126}$$

Now we construct the outgoing radial wave with the appropriate asymptotic form.

$$\begin{aligned}\psi^{scattered} &= (ST)\sum_m (d^e_m n^e_m Be_m(\theta)Be_m(\nu)He_m(\mu) \\ &+ d^o_m n^o_m Bo_m(\theta)Bo_m(\nu)Ho_m(\mu))\begin{pmatrix}1\\0\end{pmatrix} \end{aligned} \tag{3.127}$$

$He_m(\mu)$ and $Ho_m(\mu)$ are the linear combinations of two linearly independent solutions to the radial WHE ($Je_m(\mu)$, $Fey_m(\mu)$) and ($Jo_m(\mu)$, $Gey_m(\mu)$) which

have the behavior of an outgoing radial wave ($He_m(r) \sim Ho_m(r) \sim e^{ikr}$) in the asymptotic limit. They play the role of Hankel functions [78] (linear combination of Bessel J and Bessel Y) which appear in the study of scattering problems in polar coordinates. d_m^e and d_m^o are the undetermined coefficients. The asymptotic form of the scattered wave is given as

$$\begin{aligned}\psi^{scattered}(\mu \to \infty) &= (ST)\sqrt{\frac{1}{\pi kR}}e^{-i\frac{\pi}{4}}e^{ikr}\sum_m (d_m^e n_m^e Be_m(\theta)Be_m(\nu) \\ &+ d_m^o n_m^o Bo_m(\theta)Bo_m(\nu))\begin{pmatrix}1\\0\end{pmatrix} \qquad (3.128)\end{aligned}$$

Now we compare our full wave function spinor, Eq. (3.108) and with the wave functions written in a suggestive form in the asymptotic limit. e^{ikr} and e^{-ikr} multiplied by the angular functions in ν are independent functions. Hence we can equate their coefficients in Eq. (3.125) and Eq. (3.124). We get four equations for the undetermined coefficients corresponding to the four independent angular functions.

$$e^{i\delta_m^e} = (1+d_m^e)n_m^e Be_m(\theta) \qquad (3.129)$$

$$e^{i\delta_m^o} = (1+d_m^o)n_m^o Bo_m(\theta) \qquad (3.130)$$

$$e^{-i\delta_m^e} = (n_m^e)Be_m(\theta) \qquad (3.131)$$

$$e^{-i\delta_m^o} = (n_m^o)Bo_m(\theta) \qquad (3.132)$$

Solving the above four equations, we can write d_m^e and d_m^o (which are the undetermined coefficients of the scattered wave) in terms of the phase shifts $\delta_m^e$and δ_m^o.

$$d_m^e = (e^{2i\delta_m^e} - 1)\ ,\ d_m^o = (e^{2i\delta_m^o} - 1) \qquad (3.133)$$

To write the full form of the scattering amplitude, we multiply the scattered wave by the ST transformation matrix in its asymptotic form.

$$\begin{aligned}\psi^{scattered} &= \sqrt{\frac{1}{\pi k}}e^{-i\frac{\pi}{4}}\sum_m (d_m^e n_m^e Be_m(\theta)Be_m(\nu) \\ &+ d_m^o n_m^o Bo_m(\theta)Bo_m(\nu))\frac{e^{ikr}}{\sqrt{r}}\begin{pmatrix}\cos\frac{\nu}{2}\\ \sin\frac{\nu}{2}\end{pmatrix} \end{aligned} \tag{3.134}$$

$\begin{pmatrix}\cos\frac{\nu}{2}\\ \sin\frac{\nu}{2}\end{pmatrix}$ represents the quasiparticle current going in the radial direction (see Eq. (3.22)). The scattering amplitude can be extracted from the asymptotic form of the scattered wave as

$$\begin{aligned}f(\theta,\nu) &= \sqrt{\frac{1}{\pi k}}e^{-i\frac{\pi}{4}}(\sum_m (e^{2i\delta_m^e}-1)n_m^e Be_m(\theta)Be_m(\nu) \\ &+ (e^{2i\delta_m^o}-1)\ n_m^o Bo_m(\theta)Bo_m(\nu)) \end{aligned} \tag{3.135}$$

Hence, we were successful in constructing the scattering amplitude (analogous to the general form of scattering amplitude (Eq. (3.21)) in elliptical coordinates. The only thing that remains is to calculate the phase shifts δ_m^e and δ_m^o, and for that we need to impose the conditions for the branch cut on the full wave function spinor, Eq. (3.108).

3.9 Scattering Cross Section without Branch Cut (Berry Phase Parameter B=0)

Before going on to the case with the branch cut, we make a quick check on our scattering amplitude for the case of no branch cut or B=0 in Eq. (3.1). We expect this trivial case to yield no scattering of quasiparticles. For the case of no branch cut between the foci of the ellipse ($\mu = 0$), we impose the following condition on the wave function spinor

$$\psi(\mu,-\nu)\mid_{\mu=0} = \psi(\mu,\nu)\mid_{\mu=0} \tag{3.136}$$

At $\mu = 0$, we have the following behavior for $Je_m(\mu)$, $Je'_m(\mu)$, $Jo_m(\mu)$ and $Jo'_m(\mu)$

$$Jo_m(0) \neq 0,\ Je_m(0) = 0 \tag{3.137}$$

$$Je'_m(0) \neq 0,\ Jo'_m(0) = 0 \tag{3.138}$$

At $\mu = 0$, the second independent solutions are all nonzero,

$$Fey_m(0) \neq 0,\ Gey_m(0) \neq 0 \tag{3.139}$$

$$Fey'_m(0) \neq 0,\ Gey'_m(0) \neq 0 \tag{3.140}$$

Applying condition (3.136), all the terms containing even parity angular eigenfunctions cancel out and we can write the remaining terms as

$$\begin{pmatrix} (\cos\delta^e_m Je_m(0) + \sin\delta^e_m Fey_m(0))Be_m(\nu) \\ i\ (\cos\delta^o_m Jo'_m(0) + \sin\delta^o_m Gey'_m(0))Ao_m(\nu) \end{pmatrix} = \begin{pmatrix} 0 \\ 0 \end{pmatrix}$$

Substituting for the values of the radial functions at $\mu = 0$, we have

$$\begin{pmatrix} (\sin\delta^e_m Fey_m(0))Be_m(\nu)) \\ i\ (\sin\delta^o_m Gey'_m(0))Ao_m(\nu) \end{pmatrix} = \begin{pmatrix} 0 \\ 0 \end{pmatrix}$$

From the boundary condition at the origin we get the following constraints on the undetermined coefficients,

$$\sin\delta^o_m = 0, \quad \sin\delta^e_m = 0 \tag{3.141}$$

The above expression gives phase shifts as $\delta^e_m = 0$ and $\delta^o_m = 0$. Putting the obtained phase shifts back into Eq. (3.135) for the scattering amplitude, we obtain

$$f(\theta, \nu) = 0 \tag{3.142}$$

Hence, we recover our trivial result that without the branch cut (and without superflow) there is no scattering. Now we move to the interesting case of quasiparticle scattering with the branch cut.

3.10 Scattering Cross Section due to a Branch cut (B=1)

For the case with a branch cut between the foci of the ellipse ($\mu = 0$), we set the Berry phase parameter B=1, which sets the condition imposed on the wave function spinor Eq. (3.108) to,

$$\psi(\mu, -\nu) \mid_{\mu=0} = -\psi(\mu, \nu) \mid_{\mu=0} \tag{3.143}$$

Applying the above condition and using the values of the radial eigenfunctions at $\mu = 0$, all the terms containing odd angular eigenfunctions cancel out and we can write the remaining terms as

$$\begin{pmatrix} (\cos\delta_m^o Jo_m(0) + \sin\delta_m^o Gey_m(0)) Bo_m(\nu) \\ i\ (\cos\delta_m^e Je'_m(0) + \sin\delta_m^e Fey'_m(0)) Ae_m(\nu) \end{pmatrix} = \begin{pmatrix} 0 \\ 0 \end{pmatrix}$$

From the boundary condition at the origin we get the following constraints on the undetermined coefficients,

$$\cos\delta_m^o Jo_m(0) = -\sin\delta_m^o Gey_m(0), \quad \cos\delta_m^e Je'_m(0) = -\sin\delta_m^e Fey'_m(0) \tag{3.144}$$

In other words

$$\tan\delta_m^e = -\frac{Je'_m(0)}{Fey'_m(0)} \tag{3.145}$$

$$\tan\delta_m^o = -\frac{Jo_m(0)}{Gey_m(0)} \tag{3.146}$$

Since $\tan\delta_m^e$ and $\tan\delta_m^o$ are complex conjugates of each other we have to account for the relative sign between δ_m^e and δ_m^o while calculating the inverse tangent in the above relation. Substituting for δ_m^e and δ_m^o in the definitions of

the phase shifts, Eq. (3.133) we obtain

$$(e^{2i\delta_m^e} - 1) = \frac{-2Je'_m(0)}{Je'_m(0) + i\ Fey'_m(0)} \tag{3.147}$$

$$(e^{2i\delta_m^o} - 1) = \frac{-2Jo_m(0)}{Jo_m(0) - i\ Gey_m(0)} \tag{3.148}$$

Using Eq. (3.147) and Eq. (3.148) we can completely evaluate the scattering amplitude and the differential cross section for quasiparticle scattering due to branch cut without the superflow.

$$\begin{aligned} f(\theta,\nu) &= \sqrt{\frac{4}{\pi k}} e^{-i\frac{\pi}{4}} \sum_m \left(\frac{Je'_m(0)}{Je'_m(0) + i\ Fey'_m(0)} \right) n_m^e Be_m(\theta) Be_m(\nu) \\ &+ \left(\frac{Jo_m(0)}{Jo_m(0) - i\ Gey_m(0)} \right) n_m^o Bo_m(\theta) Bo_m(\nu) \end{aligned} \tag{3.149}$$

We can write the exact differential cross section for the quasiparticle scattering in terms of $\varphi = \nu - \theta$,

$$\begin{aligned} \frac{d\sigma}{d\varphi} &= \frac{4}{\pi k} \Bigg| \sum_m \left(\frac{Je'_m(0)}{Je'_m(0) + i\ Fey'_m(0)} \right) n_m^e Be_m(\theta) Be_m(\varphi + \theta) \\ &+ \left(\frac{Jo_m(0)}{Jo_m(0) - i\ Gey_m(0)} \right) n_m^o Bo_m(\theta) Bo_m(\varphi + \theta) \Bigg|^2 \end{aligned} \tag{3.150}$$

Recall that at the outset of this calculation, we shifted the origin of momentum space to the center of node 1. Thus, in the discussions that followed, we have been considering quasiparticles scattered from one state in the vicinity of node 1 to another state in the vicinity of node 1. The resulting cross section is therefore only the cross section for these node-1 quasiparticles. However, given a quasiparticle current in any particular direction, quasiparticles from all four nodes will contribute equally. Thus to obtain the physical cross section, we must average over the cross sections for quasiparticles at each of the four nodes. Our results for node 1 can be easily generalized to node $j = \{1, 2, 3, 4\}$ by transforming coordinates to those appropriate to node j. In accordance with the d-wave structure of the gap, we can define a local coordinate system

at each of the four nodes with a $\hat{\mathbf{k}}_1$ axis pointing along the direction of increasing ϵ_k and a $\hat{\mathbf{k}}_2$ axis pointing along the direction of increasing Δ_k. Note that while nodes 1 and 3 define right-handed coordinate systems, nodes 2 and 4 define left-handed coordinate systems. We can therefore transform from node 1 to node j simply by rotating our incident and scattered angles (θ and ν) and then changing the sign of these angles to account for the handedness of the local coordinate system.

$$\begin{array}{lllll} \text{Node 1:} & \theta_1 = \theta & \nu_1 = \nu & \varphi_1 = \nu_1 - \theta_1 = \varphi \\ \text{Node 2:} & \theta_2 = -(\theta - \frac{\pi}{2}) & \nu_2 = -(\nu - \frac{\pi}{2}) & \varphi_2 = \nu_2 - \theta_2 = -\varphi \\ \text{Node 3:} & \theta_3 = \theta + \pi & \nu_3 = \nu + \pi & \varphi_3 = \nu_3 - \theta_3 = \varphi \\ \text{Node 4:} & \theta_4 = -(\theta + \frac{\pi}{2}) & \nu_4 = -(\nu + \frac{\pi}{2}) & \varphi_4 = \nu_4 - \theta_4 = -\varphi \end{array} \tag{3.151}$$

Thus, to obtain results for quasiparticles about node j, we need only input each θ_j and take the output as a function of $(-1)^{j+1}\varphi$. Then the physical cross sections are

$$\frac{d\sigma}{d\varphi} = \frac{1}{4}\sum_{j=1}^{4}\left(\frac{d\sigma}{d\varphi}\right)_j \qquad \sigma_{\parallel} = \frac{1}{4}\sum_{j=1}^{4}\sigma_{\parallel}^{j} \tag{3.152}$$

3.11 Differential Cross Section Results for Berry Phase Scattering

In this section we plot the differential cross section for quasiparticle scattering from branch cut (no superflow) for several cases. We define the distance between the two vortices by the dimensionless parameter kR. The incident angle for the current is described by θ as shown in Fig. 3.3. The thick dots on the foci of the ellipse depict the vortex cores and the thick line joining the cores denotes the branch cut and is also the μ=0 line in elliptical coordinates. The wiggly arrows represent the incident quasiparticle current. The angle of incidence is θ with respect to the x-axis. The plane wave spinor representing quasiparticle current is incident on the vortex cores and part of it acquires a Berry phase factor of (-1) between the vortex cores. The scattering contribution is entirely

due to this effect.

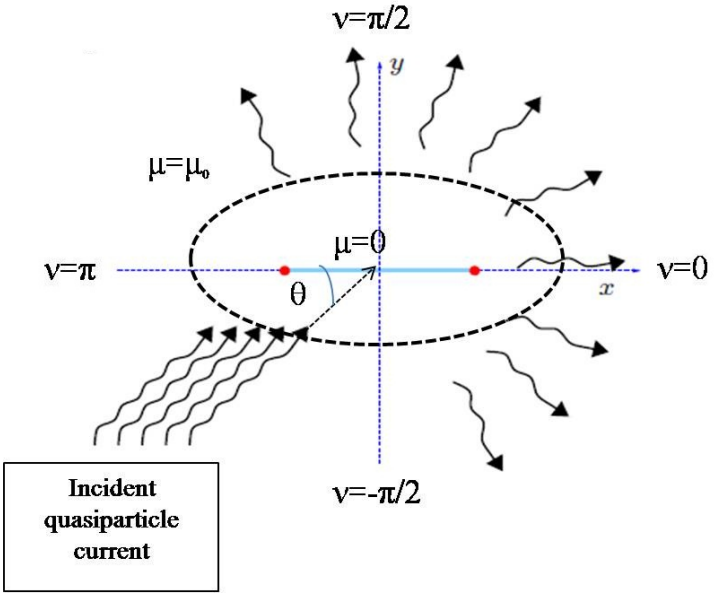

Figure 3.3: Schematic of scattering of quasiparticles due to the Berry phase effect. The Berry phase effect is denoted by the finite branch cut shown by the thick line joining the dots. The dots represent the vortex cores coinciding with the foci. Wiggly lines denote the incident quasiparticle current. θ is the incident angle of the quasiparticle current with respect to the x-axis.

For very small inter vortex separation (kR=0.1), the ellipse looks like a circle (see Fig. 3.4). In this limit we expect near-circular symmetry in the plots of the differential cross section. We see that the quasiparticles see a relatively small branch cut which results in the differential cross section being almost independent of the incident angle θ (see Fig. 3.4). Note that this is not a very good limit physically since we can no longer ignore the presence of other vortices in the sample. When we stretch the vortex cores apart (kR=1), the scatterer becomes more elliptical (see Fig. 3.5). This is reflected in the elliptical symmetry we see in the cross section plots as we rotate the incident angle of the quasiparticle current (see Fig. 3.5). We see that we get the same plots for differential cross section if we rotate the incident angle by π, which reflects the symmetry of the scatterer (symmetric under π rotation).

As we increase the inter-vortex separation further to kR=3.0, we obtain

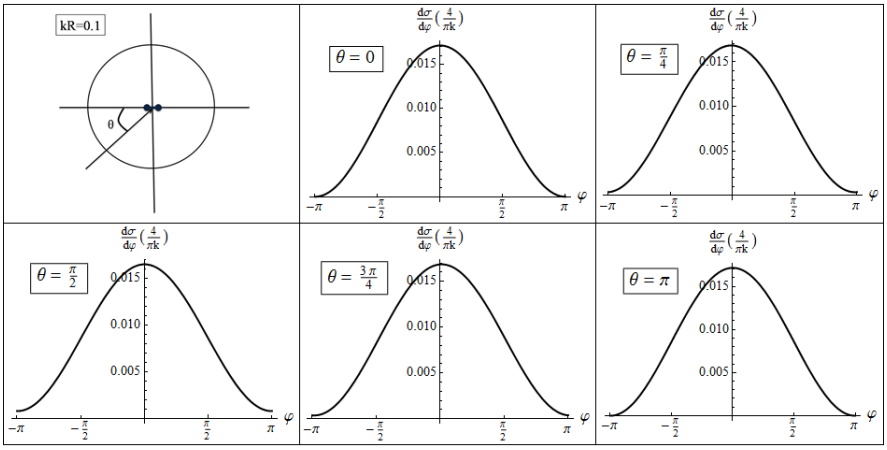

Figure 3.4: Vortex cores (foci of ellipse) are depicted by dots and the line joining them is the branch cut. Vortex cores are separated by dimensionless length kR=0.1. θ is the angle of incidence of the quasiparticle current. For small inter-vortex separation, the ellipse looks like a circle which indicates near-circular symmetry in the scatterer. We plot the single-node differential scattering cross section for quasiparticle current incident at different angles θ. The plots of the scattering cross section emphasize the near-circular symmetry with respect to the incident angle θ due to small inter vortex separation.

the case of a highly elliptical scatterer. For this case the magnitude of the scattering cross section increases as compared to the case of kR=1 (see Fig. 3.6). We observe the scattered current sweeping closer to the forward direction for higher kR. For kR=1 and kR=3, we see maximum scattering for the case of $\theta = \pi/2$. At this angle the quasiparticle current is normally incident on the branch cut and results in maximum exposure to the Berry phase effect. Mirror symmetry about $\theta = \pi/2$ is seen in the cross section plots. Thus our results for the scattering cross section are consistent with the geometry of the scatterer. We note that the scattering is reflectionless, or in other words, there is no backscattering of the quasiparticle current. The absence of backscattering due to the Berry phase has been previously reported in the literature for the case of carbon nanotubes (see Ref. [79]).

We must now average over the scattering contribution due to quasiparticles from all four nodes. The four node average has been performed as prescribed in Eq. (3.151) and Eq. (3.152). After averaging over four nodes, we still see

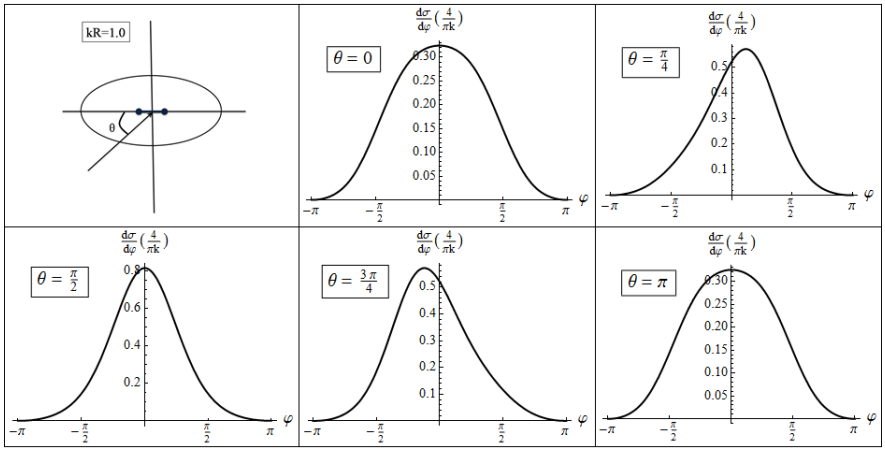

Figure 3.5: Vortex cores are further apart with dimensionless length kR=1.0. With the increase in inter-vortex separation the scatterer becomes more elliptical and plots show expected elliptical symmetry in the single node differential scattering cross section. Also note the increased magnitude of scattering cross section which can be attributed to the increase in the length of branch cut. In other words, more quasiparticles hit the branch cut

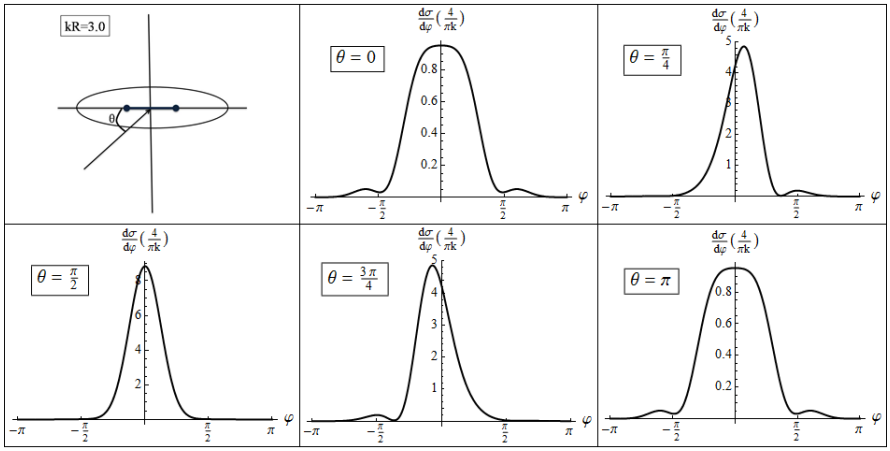

Figure 3.6: Vortices are further apart with kR=3.0. The plots of the single node scattering cross section show elliptical symmetry. We also see increase in the magnitude of scattering cross section as compared to the case of kR=1.0

θ dependence in the differential cross section (see Fig. 3.7). The resulting cross section is $\pi/2$ periodic with respect to θ. This is a consequence of the definition of θ at each node (see Eq. (3.151)). We should keep in mind that in the setup that we consider (cuprate sample), the pair of vortices is not always

aligned along the x-axis as shown in Fig. 3.3.

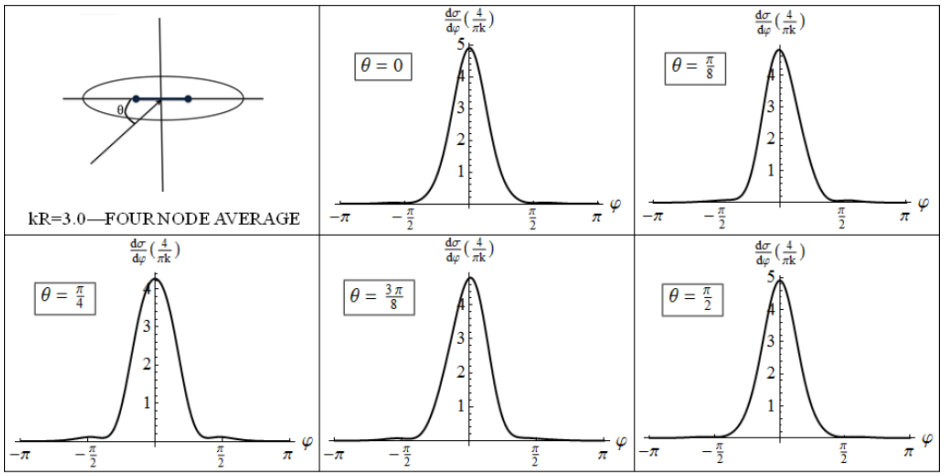

Figure 3.7: Four node average differential cross section. We plot differential cross section averaged over the contributions of quasiparticles from all four gap nodes, for quasiparticle current incident at various angles θ and for inter-vortex separation kR=3.0. Results are $\pi/2$ periodic with respect to θ.

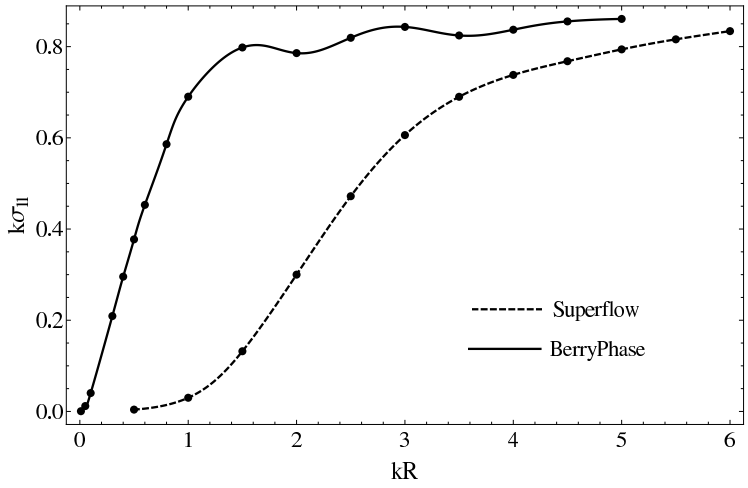

Figure 3.8: $k\sigma_{\parallel}$ plotted versus increasing inter vortex separation, averaged over the incident angle θ. The solid curve shows the transport cross section for the Berry Phase scattering case. The dashed curve shows the transport cross section for the superflow scattering. Inset shows $k\sigma_{\parallel}$ plot for the case of superflow scattering of quasiparticles plotted for very high kR values [1].

In Fig. 3.8, we plot the total transport cross section, $k\sigma_{\parallel}$ as a function of

inter-vortex separation kR.

$$k\sigma_{\parallel} = \int_{-\pi}^{\pi} d\varphi \, \frac{d\sigma}{d\varphi}(1 - \cos\varphi) \tag{3.153}$$

We notice that the transport cross section goes to 0 as kR→0. This is expected since the Berry phase effect (branch cut) is negligible for very small values of kR. With the increase in kR, the longitudinal cross section increases rapidly and then saturates for $kR > 1$. On the basis of the transport cross section plots obtained for the case of superflow and Berry phase scattering, one can make an intuitive comparison of these two effects. In the superflow paper [1], we have neglected the Berry phase effect by applying periodic boundary conditions to the quasiparticle wave functions. This amounts to scattering of quasiparticles from vortices with superflow potential with the strength of two vortices. To calculate the transport cross section for the case of a branch cut between the two vortices, we have neglected the superflow contribution. Hence we have neatly isolated the scattering contributions due to these two effects, which gives us an opportunity to compare these two effects. Before such a comparison, we must treat the case of the Berry phase scattering on an equal footing with the superflow scattering. Due to the two-center nature of the regularized Berry phase effect, we are dealing with elliptical geometry in this case. Upon performing the four-node average, we see that this elliptical symmetry shown in the differential cross section plots (See Fig. 3.6) has been reduced to near circular symmetry even for the highly elliptical case of kR=3 (Fig. 3.7). Also, since there is no preferred orientation of the branch cut, one can average over the alignment of the branch cut with respect to the x-axis. The final DCS averaged over this alignment will have no elliptical symmetry or skew scattering. Based on the above arguments, we may directly compare the transport cross section due to superflow potential of two vortices of radii kR on top of each other to the Berry phase scattering due to two vortices separated by the distance kR (averaged over incident angle θ). In both cases, kR parameterizes the dimensionless energy of incident quasiparticles. kR also determines the size of the vortex for the case of superflow scattering and the length of the branch cut for the case of Berry phase scattering. For the super-

flow case, we see a steep increase in the transport cross section (after averaging over 4 nodes) followed by saturation for $kR > 5$. For the case of Berry phase scattering, the increase in transport cross section is steeper than for the superflow case. For the Berry phase scattering the magnitude of $k\sigma_{\parallel}$ saturates for $kR > 1$. This shows that the Berry phase is the more important effect of the two for $kR < 5$ (high field low temperature regime). The magnitudes of transport cross sections for higher kR (weak field high temperature regime) are similar for both the superflow and Berry phase processes. On the basis of the plots of transport cross section for both cases, one can conclude that the transport cross section due to the branch cut dominates for $kR < 5$, and is of similar order to the superflow contribution for $kR > 5$.

3.12 Conclusions

In this chapter, we calculated the Berry phase contribution to the scattering of quasiparticles from vortices in a d-wave superconductor. We simplified the Bogoliubov-de Gennes Hamiltonian by applying a singular gauge transformation. This transformation extracts the phase from the gap function and encodes it in the antiperiodic boundary conditions imposed on the wave function. Within the single-vortex approximation, this antiperiodic boundary condition (Berry phase) manifests itself as a semi-infinite branch cut such that with each trip around the origin, the wave function changes sign. We neglected the superflow contribution and considered the scattering of quasiparticles due only to the presence of this antiperiodic boundary condition. We found the scattering cross section for this case to be divergent in the forward direction. In order to regularize the Berry phase effect, we considered the two vortex problem (two Aharonov-Bohm half fluxes) which has a finite branch cut between its cores. To solve this two-center problem, we chose to work in elliptical coordinates,which provide an advantage in implementing the branch cut condition on the wave function spinor. We can turn on the Berry phase effect by simply imposing the boundary condition (see Eq. (3.1)) on the wave function spinor. We separated the (2+1)d Dirac equation in elliptical coordinates and found that the separated equations were Whittaker Hill equations

(WHE). We solved the eigenvalue problem for the angular WHE. With the calculated eigenvalue as a parameter, we obtained the two linearly independent radial solutions with well-defined asymptotic behavior. We developed a plane wave expansion for the incident quasiparticle current in terms of the separated solutions of the WHE. Using a partial wave analysis, we expressed the scattering amplitude and differential cross section in terms of phase shifts. We obtained the phase shifts by imposing the branch cut condition (Berry phase effect) on the full wave function spinor. We analyzed the scattering cross section due to the Berry phase effect for different separations of the vortex cores. We have also presented the variation of the total transport cross section as a function of the inter-vortex separation. We have also given a qualitative comparison of transport cross sections for the Berry phase and the superflow scattering mechanisms in Sec. 3.11. The Berry phase scattering of quasiparticles discussed here is not restricted to the case of d-wave superconductors. With some modifications of the incident plane wave, our problem becomes that of general relativistic scattering in two dimensions due to two Aharonov-Bohm half fluxes. In this work, we have neglected the superflow contribution. Single vortex scattering due to a circulating superflow is considered in a separate paper [1]. The problem that we have considered in both the manuscripts is a simplified version of a more complicated scattering process. We have made a series of approximations [1] to tackle the problem in its simplest form. This work should be treated as a first step forward to understand the complicated and important issue of scattering of quasiparticles from vortices. Deviating from the analytical setup, we can improve the model by considering the anisotropic Dirac spectrum, internodal scattering, and an even more rigorous description of plane waves. All these effects become important once we move away from the weak-field limit. The linearized version of the BdG equation is limited to low energy quasiparticle excitations and one must use the full BdG equation and solve it numerically for higher energy cases. One way to include the above mentioned effects is to consider a sea of vortices in a lattice model. Such a vortex lattice calculation has been considered by Melikyan and Tesanovic [54]. In the appendix of their paper, they have set up the two vortex scattering problem in elliptical coordinates. In this chapter,

we have successfully obtained the exact scattering solutions to the two vortex problem in elliptical coordinates. The results of our calculations along with the vortex lattice calculations provide a greater insight into the bigger picture of quasiparticle scattering from vortices. To this end, our simplified model of double vortex scattering in an analytical framework is an important result. Our next step will be to consider both effects within the double vortex model by including the superflow that circulates around the vortices in the presence of the branch cut that lies between them. We expect that this analysis, left for future research, will provide insight about not only the relative importance of the two contributions but also the interference between them.

Chapter 4

Quantum effects in 1D: Fractional Quantum Hall Edge Interferometry

4.1 Introduction

Quantum Hall devices are realized in Gallium-Arsenide heterostructures, in which the the electrons are confined to the two-dimensional interface between a layer of doped $Al_xGa_{1-x}As$ and undoped GaAs. The doped layer is a semiconductor, while the undoped one is an insulator. By applying a confining electric field perpendicular to the interface (gate voltage), a 2DEG is formed at the interface. In order for an incompressible (Hall) state of the 2DEG to emerge, the device is brought into a strong magnetic field transversal to the interface. A voltage drop V_y may be applied inside the interface so as to generate an electric current I_y. Due to the Lorentz force acting on the electrons that carry the current, a voltage drop V_x in the direction perpendicular to the current is then observed. Fundamental properties of quantum Hall system can be understood in terms of standard electrodynamics. We write down the electrodynamics of the incompressible Hall fluid. The following section is based on the review article by Bieri and Fröhlich [80].

4.1.1 Electrodynamics of incompressible Hall liquid

Consider a 2DEG confined to a planar region and in presence of strong, uniform external magnetic field $\vec{B}_0$ perpendicular to (X, Y) plane. Due to the mobility gap in the bulk (or $R_L = 0$), we have a incompressible quantum hall fluid. On slowly varying the em fields ($\vec{B}^{total} = \vec{B}_0 + \vec{B}(\vec{x})$, we study the the orbital dynamics of electrons in the planar region. This dynamics only depends on $B_z^{total} = (\vec{B}_0 + \vec{B}(\vec{x})) \cdot \vec{e}_z$ and $\vec{E}_{\|} = \boldsymbol{E}(x) = (E_1(\vec{x}), E_2(\vec{x}))$. The electromagnetic field tensor in 2+1 dimensions can be written as,

$$(F_{\mu\nu}) = \begin{pmatrix} 0 & E_1 & E_2 \\ -E_1 & 0 & -B \\ -E_2 & B & 0 \end{pmatrix} . \tag{4.1}$$

Electrodynamics of Quantum hall state can be written in terms of following equations.

$$j^k(\vec{x}) = \sigma_H \epsilon^{kl} E_l(\vec{x}) \tag{4.2}$$

which is **Hall's law** (for $R_L = 0$). The electric current is perpendicular to the electric field. Charge- and current density in Λ satisfy the continuity equation given by

$$\frac{\partial}{\partial t} \rho(\vec{x}) + \boldsymbol{\nabla} \cdot \boldsymbol{j}(\vec{x}) = 0 . \tag{4.3}$$

From **Faraday's induction law** we can write,

$$\frac{\partial}{\partial t} B_z^{total}(\vec{x}) + \boldsymbol{\nabla} \times \boldsymbol{E}(\vec{x}) = 0 . \tag{4.4}$$

Based on the above written equations we arrive at

$$\frac{\partial}{\partial t} \rho = -\boldsymbol{\nabla} \cdot \boldsymbol{j} = -\sigma_H \boldsymbol{\nabla} \times \boldsymbol{E} = \sigma_H \frac{\partial}{\partial t} B_z^{total} . \tag{4.5}$$

We integrate Eq. (4.5) in time, with integration constants chosen such that

$$\begin{aligned} j^0(\vec{x}) &= \rho(\vec{x}) + en , \\ B_z^{total}(\vec{x}) &= B(\vec{x}) + B_0 , \end{aligned} \tag{4.6}$$

where $-en$ is the charge density of a homogenous 2DEG in a constant magnetic field $\vec{B}_0$. We then arrive at the Chern-Simons Gauss Law [81]

$$j^0(\vec{x}) = \sigma_H B(\vec{x})\,. \tag{4.7}$$

In terms of the electromagnetic field tensor, we can write Faraday's induction law as

$$\partial_{[\mu} F_{\nu\lambda]} = 0\,, \tag{4.8}$$

which in turn can be written in terms of vector potential,

$$F_{\mu\nu} = \partial_{[\mu} A_{\nu]}\,. \tag{4.9}$$

In compact notation we can write the current as,

$$\begin{aligned} j^\mu(x) &= \frac{\sigma_H}{2}\,\epsilon^{\mu\nu\lambda} F_{\nu\lambda}(x) && (4.10)\\ &= \sigma_H\,\epsilon^{\mu\nu\lambda}\partial_\nu A_\lambda(x)\,. && (4.11) \end{aligned}$$

Whenever σ_H is constant, the current (4.10) satisfies the continuity equation (ii), i.e.,

$$\partial_\mu j^\mu = \frac{1}{2}\sigma_H \epsilon^{\mu\nu\lambda}\partial_\mu F_{\nu\lambda} \overset{(4.8)}{=} 0\,. \tag{4.12}$$

At the boundary of the sample Σ, the value of σ_H jumps (across the boundary seperating the Hall state and the insulator) and the current (4.10) is not conserved (violates continuity equation)

$$\partial_\mu j^\mu(\vec{x}) = \frac{1}{2}\epsilon^{\mu\nu\lambda}(\partial_\mu \sigma_H)\, F_{\nu\lambda} \neq 0\,,\ \text{for } x \in \Sigma\,, \tag{4.13}$$

In order to resolve this contradiction, we need to define a total current that has an edge component added at the boundary of this discontinuity. Hence we can derive the edge dynamics from the requirement of consistency of continuity

condition. with

$$\begin{aligned} \partial_\mu j^\mu_{total} &= 0\,, \\ j^\mu_{total} &= j^\mu_{bulk} + j^\mu_{edge}\,,\,, \\ \boldsymbol{j}_{edge} \cdot \boldsymbol{\nabla}\sigma_H &= 0\,. \end{aligned}$$

Equation (4.13) for the *bulk current* (4.10) then implies that, on the "edge" Σ,

$$\partial_\mu j^\mu_{edge} = -\partial_\mu j^\mu_{bulk} = \Delta\sigma_H E_\parallel|_\Sigma\,, \tag{4.14}$$

where $E_\parallel|_\Sigma$ denotes the electric field "parallel" to Σ (i.e., the component of $\boldsymbol{E}|_\Sigma$ parallel to the contour lines of σ_H) and $\Delta\sigma_H$ is the discontinuity of σ_H across Σ. This non-conservation of the edge current is called *chiral anomaly* in $1+1$ dimensions. The chiral anomaly (in $3+1$ dimensions) is a well-known phenomenon in gauge theories of elementary particles. In the following section we exploit this anomaly to write the gauge invariant form of the edge action.

4.2 Effective action of Hall liquid confined in infinite strip

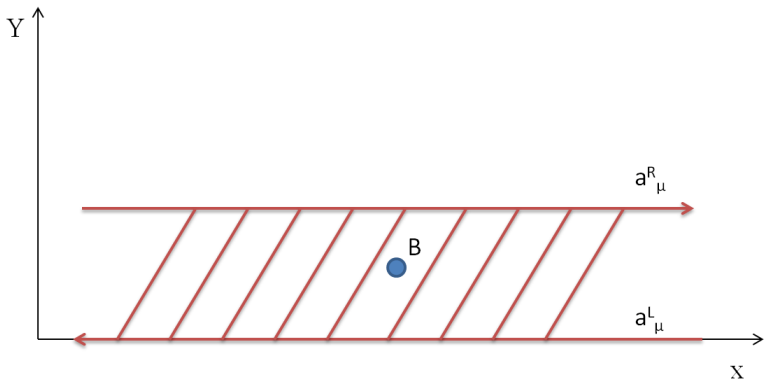

Figure 4.1: Fractional Quantum Hall in infinite strip.

Based on the idea of chiral anomaly we write down gauge invariant effective

action that gives the current in Eq. (4.10).

$$S[A] = \frac{\nu}{4\pi}\int_D d^3r\epsilon^{\mu\nu\lambda}A_\mu\partial_\nu A_\lambda \tag{4.15}$$

. This action is the well known Chern-Simons action in (2+1)D [82]. For an infinitely extended Hall droplet this action is gauge invariant. But for a finite domain this action is gauge non-invariant due to the boundary terms. We now derive the effective edge action designed to cancel this anomaly. We write the effective edge action in a gauge non-invariant form where we can manipulate the two edges independently (see Fig. (4.1)). The gauge invariant action describing incompressible FQH droplet in infinite strip is given by

$$\begin{aligned} S &= S_{cs}^{bulk}[A_\mu] + S_L^{edge}(a_\mu^L) + S_R^{edge}(a_\mu^R) \\ S &= \frac{\nu}{4\pi}\int_D d^3r\epsilon^{\mu\nu\lambda}A_\mu\partial_\nu A_\lambda \\ &+ \frac{1}{4\pi}\sum_i^{L,R}\int dxdt[\gamma_i D_t\phi^i D_x\phi^i - v(D_x\phi^i)^2 + \kappa_i\epsilon^{\mu\nu}a_\mu^i\partial_\nu\phi^i] \end{aligned} \tag{4.16}$$

where we have defined the gauge invariant covariant derivative as,

$$D_\mu\phi^i = \partial_\mu\phi^i + \gamma_i\kappa_i a_\mu^i. \tag{4.17}$$

Here $\gamma_i = \pm 1$ is the chirality of the edge and κ_i is the normalization constant and is fixed by the anomaly cancellation. We have also defined the vector potentials $a_\mu^{R,L} = \gamma_{R,L}A_\mu|_{\partial D^{R,L}}$ as the boundary definitions of A_μ on the two edges of the infinite FQH strip. The definition of two "independent" boundaries allows us to manipulate the edges via different boundary gauge fields. Now we show that the overall action is gauge invariant. We make the transformation $A_\mu \to A_\mu + \partial_\mu\beta$, $a_\mu^i + \partial_\mu\beta^i$ and $\phi^i \to \phi^i - \gamma_i\kappa_i\beta_i$ on S. Individual

terms in S are not gauge invariant and transform as follows,

$$\begin{aligned} S &= S + \delta S_{cs}^{bulk}[A_\mu] + \delta[S_L^{edge}(a_\mu^L) + S_R^{edge}(a_\mu^R)] \\ &= S + \sum_i^{R,L} \frac{\nu}{4\pi} \int_{\partial D^i} d^2r \gamma_i \epsilon^{\mu\nu} \beta^i \partial_\mu A_\nu|_{\partial D^i} - \frac{1}{4\pi} \sum_i^{R,L} \gamma_i \kappa_i^2 \int dx dt \beta^i \epsilon^{\mu\nu} \partial_\mu a_\nu^i \end{aligned} \tag{4.18}$$

S becomes gauge invariant if we set the normalization $\kappa_i^2 = \nu$.

$$S = \frac{1}{4\pi} \sum_i^{L,R} \int dx dt [\gamma_i D_t \phi^i D_x \phi^i - v(D_x \phi^i)^2 + \kappa_i \epsilon^{\mu\nu} a_\mu^i \partial_\nu \phi^i] \tag{4.19}$$

Expanding the definition of covariant derivatives we obtain,

$$\begin{aligned} S &= \frac{1}{4\pi} \sum_i^{L,R} \int dx\ dt [-\phi^i (\gamma_i \partial_t \partial_x - v\partial_x^2)\phi^i \\ &+ \kappa_i^2 (\gamma_i a_0^i a_1^i - v(a_1^i)^2) - 2\kappa_i \phi^i \partial_x (a_0^i - v\gamma_i a_1^i)] \end{aligned} \tag{4.20}$$

Our goal in the above action is to shift the field ϕ^i in such a way that it cancels the linear terms in ϕ^i. In order to do that, we use the following parametrization of the gauge fields.

$$a_0^i = \dot{\alpha}^i - v\beta_x^i,\ a_1^i = \alpha_x^i - \frac{1}{v}\dot{\beta}^i \tag{4.21}$$

We can rewrite the above expression in an alternative form,

$$\Box \beta^i = (\partial_x a_0^i - \partial_t a_1^i) \tag{4.22}$$

$$\Box \alpha^i = (\frac{1}{v}\partial_t a_0^i - v\partial_x a_1^i) \tag{4.23}$$

Where we define the D' Alembertian operator as $\Box = \frac{1}{v}\partial_t^2 - v\partial_t^2$. Expanding the covariant derivative in the Eq. (4.19) and writing it in terms of parameterized

gauge potentials.

$$S = \frac{1}{4\pi}\sum_{i}^{L,R}\int dxdt[-\phi^i(\gamma_i\partial_t\partial_x - v\partial_x^2)\phi^i - 2\kappa_i\gamma_i\phi^i\partial_x(\gamma_i\partial_t - v\partial_x)(\alpha^i + \gamma_i\beta^i)$$
$$+ \kappa_i^2(\alpha_x^i - \frac{1}{v}\dot{\beta}^i)(\gamma_i\partial_t - v\partial_x)(\alpha^i + \gamma_i\beta^i) + \kappa_i^2(\gamma_i a_0^i a_1^i - v(a_1^i)^2)] \quad (4.24)$$

Now we shift the fields $\phi^i \to \phi^i - \gamma_i\kappa_i(\alpha^i + \gamma_i\beta^i)$. Under this shift the action in Eq. (4.24) transforms as,

$$S = \frac{1}{4\pi}\sum_{i}^{L,R}\int dxdt[-\phi^i(\gamma_i\partial_t\partial_x - v\partial_x^2)\phi^i + \kappa_i^2\gamma_i\beta^i\Box(\alpha^i + \gamma_i\beta^i)] \quad (4.25)$$

We can now write the fields in terms of the vector potentials.

$$S = \frac{1}{4\pi}\sum_{i}^{L,R}\int dxdt[-\phi^i(\gamma_i\partial_t\partial_x - v\partial_x^2)\phi^i$$
$$+ \kappa_i^2\gamma_i(\partial_x a_0^i - \partial_t a_1^i)(\partial_t - v\gamma_i\partial_x)^{-1}(a_0^i - \gamma_i v a_1^i)] \quad (4.26)$$

Now we choose a gauge where $a_0^i = 0$ and $\partial_t a_1^i = E^i(x,t)$

$$S = \frac{1}{4\pi}\sum_{i}^{L,R}\int dxdt\left[-\phi^i(\gamma_i\partial_t\partial_x - v\partial_x^2)\phi^i + v\kappa_i^2\frac{a_1^i\partial_t a_1^i}{(\partial_t - v\gamma_i\partial_x)}\right] \quad (4.27)$$

In the above action the left and right edges are completely decoupled and can be manipulated independently using different gauge fields. In other words the edges that do not participate in the tunneling process can be integrated out from the partition function. To make contact with interferometers made out of these edges, we write edges as ϕ_1 and ϕ_2 and their chirality is determined by γ_1 and γ_2 which also determines the geometry of the interferometers (Fabry Perot or Mach-Zehnder). Note that our description allows us to consider each edge of the infinite FQH strip independently. The gauge fields coupled to them can also be varied independently. We consider system of two FQH strips with two tunneling point contacts between any two edges of different droplets (see Fig. (4.2)).

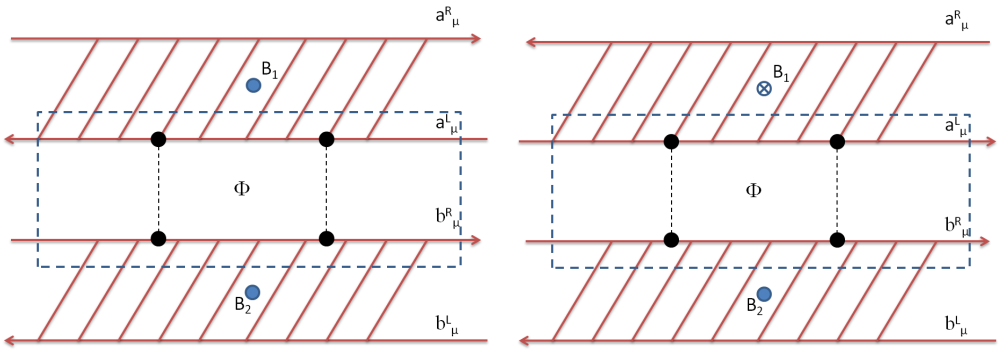

Figure 4.2: 2 point contact Fabry Perot(left) and Mach Zehnder(Right) interferometers made of two FQH edges.

4.2.1 Interferometer Currents from Generalized Gauge Fields

We construct interferometers (see Fig. (4.2)) from these decoupled edges with point contact tunneling described by two boundary Sine-Gordon terms.

$$\begin{aligned} S &= \frac{1}{4\pi}\sum_{i=1}^{2}\int dxdt\partial_x\phi_i(\gamma_i\partial_t - v_i\partial_x)\phi_i \\ &+ \int dt\sum_j \frac{DU_j}{\pi}\cos\left(\frac{\phi_1(x_j,t)}{\sqrt{\nu_1}} - \frac{\phi_2(x_j,t)}{\sqrt{\nu_2}} + \bar{a}_j(t)\right) \\ &+ \frac{1}{4\pi}\sum_{i=1}^{2}\int dxdt\ v\kappa_i^2\left(\frac{a_1^i\partial_t a_1^i}{\partial_t - v_i\gamma_i\partial_x}\right) \end{aligned} \tag{4.28}$$

where $\kappa_i = \sqrt{\nu_i}$

$$\bar{a}_j(t) = a_j(t) + \sum_i (-1)^i\gamma_i(\alpha^i(x_j,t) + \gamma_i\beta^i(x_j,t)) \tag{4.29}$$

We define $a_j(t)$ as the integrated vector potential responsible for tunneling from one edge to another via jth point contact. Varying the action with respect to $a_j(t)$ gives the tunneling current from the point contact j. $a_1^i(x,t)$ is the vector potential corresponding to the ith edge. Varying the action through $a_1^i(x,t)$ gives current at any point x on the ith edge. The shift term in the

fields can be written as

$$(\alpha^i + \gamma_i\beta^i) = -v_i\gamma_i \int\int dx'dt' Q^i(x-x',t-t')a_1^i(x',t') \quad (4.30)$$

where we have defined the retarded kernel Q as,

$$\begin{aligned} Q^i(x-x',t-t') &= \int\int d\omega dk \frac{e^{ik(x-x')-i\omega(t-t')}}{i(\omega+\gamma_i v_i k+i0)} \\ Q^i(x-x',t-t') &= \theta(t-t')\delta(x-x'+\gamma_i v_i(t-t')) \end{aligned} \quad (4.31)$$

Substituting the kernel we can obtain expressions for $\alpha^i + \gamma_i\beta^i$:

$$(\alpha^i + \gamma_i\beta^i) = -v_i\gamma_i \int_{-\infty}^{t} dt' a_1^i(x+\gamma_i v_i(t-t'),t') \quad (4.32)$$

The point contact tunneling current is given as,

$$\begin{aligned} I_j(t) &= \frac{\delta S[\phi_1,\phi_2,a_1,a_2,a_1^1,a_1^2]}{\delta a_j(t)} \\ &= \frac{-DU_j}{\pi}\sin\left(\frac{\phi_1(x_j,t)}{\sqrt{\nu_1}} - \frac{\phi_2(x_j,t)}{\sqrt{\nu_2}} + \bar{a}_j(t)\right) \end{aligned} \quad (4.33)$$

The current at any point on the ith edge is given by,

$$\begin{aligned} I^i(x,t) &= \frac{\delta S[\phi_1,\phi_2,a_1,a_2,a_1^1,a_1^2]}{\delta a_1^i} \\ &= \frac{v_i\ \nu_i}{2\pi}\int_{-\infty}^{0} dt' E^i(x+\gamma_i v_i t',t) + \sum_j \theta(\gamma_i(x-x_j))I_j(t) \end{aligned} \quad (4.34)$$

In the next part of this chapter we calculate explicit expressions for current in both weak and strong tunneling limits. We show that including compactness of chiral boson theory in the path integral formalism is important for obtaining physical results in the strong tunneling limit.

4.3 Field Theory of Two Point Contact Interferometers of Arbitrary Filling Factors.

Introduction. The defining feature of quantum Hall states is the existence of topologically protected massless edge states. These states are believed to be effectively described by a theory of chiral bosons also known as the one-dimensional chiral Luttinger Liquid (χLL) [82, 83] (for review see [84]). The tunneling experiments provide one of the natural ways to probe these edge states [84]. The theory of tunneling into FQHE edge was extensively developed over last two decades [82, 84–102]

The simplest model which is believed to universally describe the tunneling into the FQHE edge is the model of two chiral bosons coupled by a tunneling cosine term. If both chiral edges are identical, the model can be mapped to an integrable boundary sine-Gordon model and analyzed both in the limit of weak and strong tunneling between the edges [85]. In the limit of strong tunneling the charge transfer between chiral edges can be described by instanton configurations of the model. The corresponding instanton expansion can be understood as a weak coupling expansion of a dual model [9, 103].

The subject of this work is the system of chiral edges coupled via several tunneling contacts. The presence of several tunneling points allows for quantum interference between several paths of charge propagation in coherent regime. Unfortunately, the model with several tunneling contacts is not integrable and cannot be solved by Bethe Ansatz.

Model. Let us start by defining the field theory model for FQHE interferometers. In this chapter we focus on the case of a two point-contact interferometer leaving generalizations to a multiple-point-contact case for future. We consider two chiral FQH edges corresponding to filling factors $\nu_{1,2}$. The Lagrangian for two FQH edges in imaginary time formalism can be written in the bosonized form as

$$L_0 = \sum_{\sigma=1}^{2} \frac{\nu_\sigma}{4\pi} (\partial_x \phi_\sigma)(i\gamma_\sigma \partial_\tau - v_\sigma \partial_x)\phi_\sigma \tag{4.35}$$

where the fields $\phi_{1,2}$ are compact ($\phi_\sigma \equiv \phi_\sigma + 2\pi$) chiral bosonic fields describing two propagating chiral edge modes with velocities $v_{1,2}$ respectively. The sign factors $\gamma_{1,2} = \pm 1$ determine the direction of propagation of chiral fields (right/left), so that $\gamma_1\gamma_2 = -1$ and $\gamma_1\gamma_2 = 1$ represent the cases of Fabry-Perot and Mach-Zehnder interferometers respectively. Each point contact tunneling can be modeled as a boundary Sine-Gordon term driven by the integrated vector potential Φ_j ($j = 1, 2$) [104]

$$L_{tunn} = -\sum_{j=1}^{2} \frac{U_j}{\delta} \cos\Big(\varphi(x_j, \tau) + \Phi_j(\tau)\Big)\,, \tag{4.36}$$

where

$$\varphi(x, \tau) = \phi_1(x, \tau) - \phi_2(x, \tau)\,, \tag{4.37}$$

U_j are tunneling amplitudes and δ represents the microscopic (ultraviolet) scale. The overall action of the system is

$$S = \int dx\, d\tau\, (L_0 + L_{tunn}) \tag{4.38}$$

and the partition function of the interferometer is given by

$$Z[\Phi_j] \;=\; \int D\phi_1 D\phi_2\, e^{-S[\phi_1, \phi_2, \Phi_j]}\,. \tag{4.39}$$

It is a functional of the e/m potentials $\Phi_j(t)$ which encodes electromagnetic responses of the interferometer. [104] Namely, the variation of (4.39) with respect to Φ_j gives the tunneling current $I_j(\tau)$ through the contact j. A functional integration in (4.39) is taken over the compact bose fields $\phi_j \equiv \phi_j + 2\pi$. We have chosen the normalization of the fields such that the electron operator on the edge j is proportional to $\sim e^{i\phi_j}$ In this work we pay special attention to the compactness of the Bosonic fields ϕ_j. In the theory of non-chiral boson the compactness is known to be important. In the path integral formulation the compactness requirement is equivalent to allowing for instanton (vortex) configurations and might lead to the Kosterlitz-Thouless transition (see e.g., [10]). In the present context of chiral fields the proper treatment of compact-

ness is crucial for obtaining correct results in the limit of strong tunneling $U_j \to \infty$. Indeed, in the limit of strong tunneling it is natural to assume that the values of the bose field at tunneling points $\varphi(x_j)$ are pinned to the minima of the cosine in (4.36) and the expansion in the number of instantons corresponding to the transitions between these minima will result in the expansion in $1/U_j$. It turns out however that this expansion is plagued by non-localities and being applied without caution produces unphysical results [92, 96, 105]. A work around solution to the problem was found by V. Ponomarenko and Averin [92, 95] who introduced auxiliary "zero modes" designed to kill pesky nonlocal terms to produce physically meaningful result. The main goal of this work is to show that the correct treatment of the compactness of the bosonic field φ makes the use of auxiliary modes unnecessary and produces physical results identical to Ref. [95].

Green's function. The tunneling part of the model (4.36) depends only on a difference φ of bose fields (4.37). We can take advantage of this fact replacing $\phi_1 \to \varphi + \phi_2$ and then integrating out the field ϕ_2. This leaves us with the partition function (4.39) given by $Z[\Phi_j] = \int D\varphi \, \exp\{S_0 + S_{tunn}\}$ where the tunneling part of the action is given by $S_{tunn} = \int d\tau \, L_{tunn}$ with (4.36) while the free part of the action is given in Fourier representation by

$$S_0[\varphi] = -\int \frac{d^2k}{(2\pi)^2} \, \varphi^* \tilde{G}^{-1} \varphi \,, \tag{4.40}$$

where

$$\tilde{G}(\omega, k) = \frac{8\pi}{\nu} \frac{\widetilde{v} - ia\omega/k}{(v_1 k - i\gamma_1\omega)(v_2 k - i\gamma_2\omega)} \,. \tag{4.41}$$

Here we defined

$$\nu^{-1} = \frac{\nu_1^{-1} + \nu_2^{-1}}{2}, \; \widetilde{v} = \frac{\nu_1 v_1 + \nu_2 v_2}{\nu_1 + \nu_2}, \; a = \frac{\gamma_1\nu_1 + \gamma_2\nu_2}{\nu_1 + \nu_2} \,. \tag{4.42}$$

We can think of ν^{-1}, $\tilde{v}$ and a as of average inverse filling factor, velocity and chirality of edges. Let us remark here the Mach-Zehnder interferometer case corresponds to $a = \pm 1$, the Fabry-Perot interferometer with $\nu_1 = \nu_2$ corresponds to $a = 0$. All other values of the parameter a are between -1 and

1 and correspond to an asymmetric Fabry-Perot interferometer.

In the limit of weak coupling the generating function $Z[\Phi_j]$ can be written as a series expansion in U_j using the correlation function (4.41) rewritten as

$$\tilde{G}(\omega,x) \;=\; \frac{\pi i}{\omega}\int\frac{dk}{2\pi}\,e^{ikx}\left[\frac{2a\gamma_1\gamma_2}{\nu k}-\sum_{\sigma=1}^{2}\frac{\gamma_\sigma/\nu_\sigma}{k-i\frac{\gamma_\sigma}{v_\sigma}\omega}\right]. \tag{4.43}$$

We can split this propagator into local and non-local contributions $\tilde{G}=\tilde{G}_{nl}+\tilde{G}_{loc}$. The non-local contribution coming from the first term in Eq. 4.43 can be written as

$$\tilde{G}|_{nl}(\tau,x) \;=\; i\frac{\pi a\gamma_1\gamma_2}{\nu}sgn(\tau)\,sgn(x)\,. \tag{4.44}$$

Since $a\gamma_1\gamma_2/\nu=(\gamma_1\nu_1^{-1}+\gamma_2\nu_2^{-1})/2$ is strictly integer number, it contributes only as an overall phase to the correlation function of corresponding vertex operators $\langle e^{i\varphi(0,0)}e^{-i\varphi(\tau,x)}\rangle = e^{i\pi\frac{a}{\nu}}\exp\{-G_{loc}(\tau,x)\}$. The only non-trivial contribution comes from the local part of the correlation function given by the second term in (4.43)

$$\tilde{G}_{loc}(\omega,x)=\sum_{\sigma=1}^{2}\frac{\pi}{\nu_\sigma|\omega|}e^{-|\omega\frac{x}{v_\sigma}}\theta(\omega\gamma_\sigma\frac{x}{v_\sigma})\,, \tag{4.45}$$

At coinciding points we understand (4.45) as a limit $x\to 0^+$ with $\theta(0^+)=1/2$.

Our goal is to find the partition function of the model (4.38,4.36,4.40) in the limit of strong tunneling $U_j\to\infty$. First of all, following previous approaches [103, 106] we are going to integrate our the degrees of freedom corresponding to the one-dimensional bulk and leave an effective action of Caldeira-Leggett type (CL) depending only at the values of fields at the tunneling contacts.

4.4 Effective Caldeira-Leggett Model.

The action of the tunneling model is quadratic except for the tunneling part (4.36) localized at tunneling point. To integrate out the bulk field we impose

the following constraint

$$\varphi(x_j, \tau) = \varphi_j(\tau) \bmod 2\pi. \tag{4.46}$$

by inserting

$$1 = \int D\varphi_j \prod_j \delta_P(\varphi(x_j) - \varphi_j). \tag{4.47}$$

into the path integral. Here we introduced new "contact" fields $\phi_j(\tau)$ which are constrained to be the values of the $\varphi(x, \tau)$ field at contact points $x = x_j$. The notation δ_P is chosen for the periodic version of the Dirac's delta function defined as

$$\delta_P(\varphi_j(\tau)) = \sum_{\alpha_j(\tau)} e^{i \int d\tau \alpha_j(\tau) \varphi_j(\tau)}, \tag{4.48}$$

where the sum is taken over the integer-valued fields $\alpha_j(\tau)$. [1] The periodicity of the constraint (4.46) is the key point of our derivation. It is very important for the following and is a direct manifestation of the compactness of φ which is ultimately related to the discreteness of electric charge.

Inserting (4.47) into the partition function and using (4.48) we can integrate out the field φ and obtain

$$Z[\Phi_j] = \int [D\varphi_j] \exp\left\{-S_{CL}[\phi_j] - S_{tunn}[\phi_j, \Phi_j]\right\}, \tag{4.49}$$

$$S_{tunn} = \int d\tau \sum_j \frac{U_j}{\delta} \cos\Big(\varphi_j(\tau) + \Phi_j(\tau)\Big) \tag{4.50}$$

$$S_{CL} = -\log \int [D\alpha_j] e^{\sum_\omega \alpha_i^* G_{ij} \alpha_j} e^{-i \sum_\omega \alpha_j^* \varphi_j}. \tag{4.51}$$

Here the latter formula is written in frequency representation and we assumed the summation over tunneling points i, j. The CL matrix Green's function is defined in terms of (4.45) as

$$G_{ij}(\omega) = \tilde{G}(\omega, x_i - x_j). \tag{4.52}$$

[1] One should think of $\alpha_j(\tau)$ as of integer number defined for every slice of imaginary time.

Notice that we dropped here the nonlocal part of the Green's function (4.44). This is allowed as the α fields are integer-valued and the contribution to the first factor in (4.51) is the overall phase.

After dropping the oscillatory non-local part of the propagator we assume that the path integral (4.51) is dominated by large fluctuations of α fields. We replace the functional summation over discrete α fields by Gaussian integration in (4.51) and obtain

$$S_{CL} \;=\; \frac{1}{4}\sum_{\omega}\varphi_i^*(G^{-1})_{ij}\varphi_j\,. \tag{4.53}$$

Indeed, the dominant fluctuations of α fields can be estimated from $\sum_\omega \delta\alpha_i^2(\omega) \approx \sum_\omega G_{ii}(\omega) \approx \sum_\omega |\omega|$, which is a huge number controlled by the ultraviolet cutoff of the problem. The partition function can be written as (4.49) with (4.50,4.53), where $(G^{-1})_{ij}$ is given by the matrix inversion of (4.52).

Current in weak tunneling limit. To calculate the tunneling current in the limit of weak tunneling we need the correlators of vertex operators given by[2]

$$\begin{aligned}\left\langle e^{i\varphi_j(\tau)}e^{-i\varphi_k(0)}\right\rangle &= e^{4\sum_\omega e^{i\omega\tau}G_{jk}} \\ &= K(\xi^1_{jk},i\tau)K(\xi^2_{jk},i\tau)\,.\end{aligned} \tag{4.54}$$

where the propagation time between the contacts is defined as

$$\xi^\sigma_{jk} = \gamma_\sigma\frac{x_j-x_k}{v_\sigma}. \tag{4.55}$$

Here we defined K as,

$$K(\xi^\sigma_{jk},i\tau) = \begin{cases} \left[\frac{1}{v_\sigma(\xi^\sigma_{jk}+i\tau)}\right]^{\frac{1}{\nu_\sigma}} & (T=0) \\ \\ \left[\frac{\pi T}{v_\sigma\sinh\pi T(\xi^\sigma_{jk}+i\tau)}\right]^{\frac{1}{\nu_\sigma}}, & (T\neq 0) \end{cases} \tag{4.56}$$

Using the correlation function (4.54,4.56) we obtain the tunneling current

[2]Note here that one could use instead of (4.52) the Green's function including the non-local term (4.44). This would not change the correlation functions for vertex operators.

through the j-th point contact in the lowest order of perturbation theory as [9, 103]

$$\begin{aligned} I_j(t) &= \sum_i \frac{U_i U_j}{2\delta^2} \int_{-\infty}^{t} dt_1 \sin(\Phi_i(t_1) - \Phi_j(t)) \\ &\times Im\left(\prod_{\sigma=1}^{2} K(\xi_{ij}^{\sigma}, t_1 - t - i0)\right). \end{aligned} \tag{4.57}$$

In fact, it is easy to write down the expression for the current at any point on the interferometer as a function of real time

$$I^{\sigma}(x,t) = I_{cs}(E_\sigma) + \sum_j \theta(\gamma_\sigma(x - x_j)) I_j(t) \tag{4.58}$$

where $I_{cs} = \frac{v_\sigma \ \nu_\sigma}{2\pi} \int_{-\infty}^{0} dt' E^{\sigma}(x + \gamma_\sigma v_\sigma t', t)$ is the current due to the electric field E_σ along the edge due to the contribution of the bulk Hall current [104].

4.5 Interference in weak tunneling regime

In this section we calculate explicit expressions for tunneling current at point contacts as a function of applied bias and flux. In this section we assume that the only vector potential applied is across the tunneling contacts by setting $\Phi_j = V\tau$. Eq. (4.57) can be used to generalize for arbitrary gauge potentials.

$$Z = \int D[\varphi_1, \varphi_2] e^{-\sum_{\omega,ij} \varphi_i^* G_{ij}^{-1} \varphi_j + \sum_j \frac{U_j}{\delta} \int d\tau \cos(\varphi_j(\tau) + \Phi_j(\tau))} \tag{4.59}$$

In the weak tunneling limit for small U_j, we expand the tunneling term. Retaining terms till first order we obtain,

$$\begin{aligned} Z = Z_0[1 &+ \frac{1}{4} \sum_{ij} \frac{U_i U_j}{\delta^2} \int d\tau_1 d\tau_2 \cos(\Phi_i(\tau_1) - \Phi_j(\tau_2)) \\ &\times K(\xi_{ij}^1, i\tau_1 - i\tau_2) K(\xi_{ij}^2, i\tau_1 - i\tau_2) + ...] \end{aligned} \tag{4.60}$$

From the above expression for partition function we can calculate current using $\langle I_k(\tau)\rangle = \frac{\delta \log(Z)}{\delta \Phi_k(\tau)}$.

$$\langle I(\tau)\rangle = \frac{1}{2}\sum_{ij}\frac{U_iU_j}{\delta^2}\int d\tau_1 \sin(\Phi_i(\tau_1)-\Phi_j(\tau))K(\xi^1_{ij}, i\tau_1 - i\tau)K(\xi^2_{ij}, i\tau_1 - i\tau) \tag{4.61}$$

We analytically continue the expression for current in Eq. (4.61) to real time along Kadanoff-Baym contour (t_0 to t and t to $t_0 + i\beta$)[107]. Out of the three branches of the contour, the vertical imaginary contribution is 0 if we ignore the initial correlations by letting $t_0 \to -\infty$. The remaining two contributions come from the forward and backward branches of the real time Keldysh contour.

$$\begin{aligned}\langle I(t)\rangle &= \sum_{ij}\frac{U_iU_j}{2\delta^2}\int_{-\infty}^{t} dt_1 \sin(\Phi_i(t_1)-\Phi_j(t)) \\ &\times -i \left[K(\xi^1_{ij}, t_1 - t)K(\xi^2_{ij}, t_1 - t)|_{>} - K(\xi^1_{ij}, t_1 - t)K(\xi^2_{ij}, t_1 - t)|_{<}\right]\end{aligned} \tag{4.62}$$

Where the $>$ ($<$) symbol represents contour ordered correlations living on the upper (lower) branch of the Keldysh contour. The differ by an infinitesimal imaginary term $+(-)i\epsilon$. Hence we directly arrive at retarded Green's functions using Keldysh trick. We define the vector potential as $\Phi_i(t_1) - \Phi_j(t) = V(t_1 - t) + \kappa_{ij}$. $\kappa = \kappa_i - \kappa_j$ is the flux responsible for the interference between the tunneling currents. Physically this means we have applied constant bias across the two tunneling contacts with a flux between the two tunneling contacts. Experimentally this scenario can be realised when one FQH droplet is kept at a constant higher bias than the other. After performing shift $t_1 \to t_1 - t$, we get

$$\begin{aligned}\langle I\rangle &= \sum_{ij}\frac{U_iU_j}{2i\delta^2}\int_{-\infty}^{0} dt \sin(Vt + \kappa_{ij}) \\ &\times \left[K(\xi^1_{ij}, t)K(\xi^2_{ij}, t) - (K(\xi^1_{ij}, t)K(\xi^2_{ij}, t))^*\right]\end{aligned} \tag{4.63}$$

Average total current in real time can be expressed as a sum of individual currents and interference current.

$$\langle I \rangle = \sum_j \langle \bar{I}_j \rangle + \langle \Delta I(\xi_{12}) \rangle \tag{4.64}$$

In real time two point chiral correlation K can be expressed as,

$$K(\xi^\sigma_{ij}, t) = \Big[\frac{\pi T}{v_\sigma \sinh \pi T(\xi^\sigma_{ij} - t - i0)}\Big]^{\frac{1}{\nu_\sigma}} \tag{4.65}$$

$$K(\xi^\sigma_{ij}, t) = \Big[\frac{\pi T}{v_\sigma \sinh \pi T(|\xi^\sigma_{ij} - t|)}\Big]^{\frac{1}{\nu_\sigma}} e^{i\frac{\pi}{2\nu_\sigma} Sgn(\xi^\sigma_{ij} - t)} \tag{4.66}$$

Here we have to keep in mind that ν_σ is a analytically continued to complex plane. We will analytically continue it back to real axis at the after evaluating the integral. We can and order the point contacts such that $x_2 - x_1 = L > 0$ and thus $\xi^\sigma = \frac{\gamma_\sigma L}{v_\sigma}$. Total average current can be expressed in terms of a common integral,

$$\langle I \rangle = \sum_j \frac{U_j^2}{2\delta^2} \mathrm{Im}[f_V(0,0,0)] + \frac{D^2 U_1 U_2}{\delta^2} \mathrm{Im}[f_V(\xi^1, \xi^2, \kappa_{21})] \tag{4.67}$$

Integral in the above expression can be written as,

$$f_V(\xi^1, \xi^2, \kappa_{12}) = (\pi T)^{\frac{2}{\nu}} P.V. \int_{-\infty}^{\infty} \frac{e^{i(Vt+\kappa_{21})} \sin\left[\frac{\pi}{2}\left(\frac{sgn(\xi^1 - t)}{\nu_1} + \frac{sgn(\xi^2 - t)}{\nu_2}\right)\right]}{[\sinh(\pi T|\xi^1 - t|)]^{\frac{1}{\nu_1}} [\sinh(\pi T|\xi^2 - t|)]^{\frac{1}{\nu_2}}} \tag{4.68}$$

Detailed result of this integral is given in the Appendix (B.2).

4.6 Strong Tunneling Limit from Compact CL Model

Let us illustrate here the role of compactness of bosonic fields using the limit of infinitely strong tunneling. In the limit of strong tunneling $U_j \to \infty$ the

path integral in (4.49) will be dominated by fields pinned to the minima of tunneling cosine term (4.50) so that the optimal field configurations are given by

$$\varphi_j(\tau) = 2\pi n_j - \Phi_j(\tau)\,, \tag{4.69}$$

where n_j are arbitrary integer numbers. The calculation of the generating functional (4.49) in this limit amounts to substitution of the optimal field configurations (4.69) into (4.49,4.50,4.51). It is very important that although the nonlocal contribution to Green's function (4.44) would be of no consequence in calculating (4.51) and in (4.54) it is vital to use only the local expression (4.52,4.45) if one calculates the value of Caldeira-Leggett action using (4.53). We start from the partition function for CL model given in Eq. (4.59). Where inverse $(G^{-1})_{ij}$ can be written in a compact form,

$$(G^{-1})_{ij} = \begin{cases} \frac{\nu|\omega|}{\pi}\frac{1}{D(\omega)} & (i=j) \\ \\ -\sum_{\sigma=1}^{2}\frac{\nu^2|\omega|}{\pi\nu_\sigma}e^{-|\omega\xi^\sigma|}\theta(\omega\xi^\sigma_{ji})\frac{1}{D(\omega)}\,, & (i\neq j) \end{cases} \tag{4.70}$$

where we defined the resonance term

$$D(\omega) = (1-(1-a^2)e^{-\sum_\sigma|\omega\xi^\sigma|}) \tag{4.71}$$

. a is given by expression 4.42. Note that the resonance is absent for the case of MZI where $a = \pm 1$ as both the edges have same chirality. $D(\omega) = 0$ corresponds to resonance that occurs for the only case of FPI ($a = 0$, $\gamma_1\gamma_2 = -1$) when $\nu_1 = \nu_2$, $\omega \to 0$. As $U_j \to \infty$, the tunneling part of the action dominates free action and classical solutions in Euclidean space corresponds to 4.72. In the limit $U < \infty$, to the first order, we allow for fields to change their values to $2\pi(n_j \pm 1)$. $e_{lj} = \pm$ corresponds to instanton/anti-instanton tunneling events to the neighboring minima for the jth point contact. In this case instanton configuration of $\varphi_j(\tau)$ is given by,

$$\varphi_j = 2\pi n_j - \Phi_j(\tau) + 2\pi\sum_l e_{lj}\theta(\tau-\tau_{lj}) \tag{4.72}$$

In ω space we can write

$$\varphi_j(\omega) = 2\pi n_j \delta(\omega) - \Phi_j(\omega) + 2\pi i \sum_l e_{lj} \frac{e^{i\omega\tau_{lj}}}{\omega}. \tag{4.73}$$

We substitute 4.72 in the free CL action $S = \frac{1}{4}\sum_\omega \varphi_i(-\omega)(G^{-1})_{ij}\varphi_j(\omega)$ which leads to

$$\begin{aligned} S &= \frac{1}{4}\sum_\omega \sum_{ij} \Big\{ \Phi_i^*(G^{-1})_{ij}\Phi_j \\ &+ 4\pi i \sum_l (\Phi_i^* - 2\pi n_i \delta(\omega)) e_{lj} (G^{-1})_{ij} \frac{e^{i\omega\tau_{lj}}}{\omega} \\ &+ \sum_{ll'} e_{l'i} e_{lj} (2\pi)^2 (G^{-1})_{ij} \frac{e^{i\omega(\tau_{lj}-\tau_{l'i})}}{\omega^2} \Big\}. \end{aligned} \tag{4.74}$$

We can rewrite the above action in terms of a dual model in strong tunneling limit that reproduces the above expansion in perturbatively.

$$\begin{aligned} S \quad & [\Theta_1, \Theta_2, \Phi_1^d, \Phi_2^d] = \frac{1}{4}\sum_{\omega,ij} \Theta_i^* M_{ij}^{-1} \Theta_j + \frac{1}{4}\sum_{\omega,ij} \Phi_i^{d*} M_{ij}^{-1} \Phi_j^d \\ - \quad & \sum_j \frac{W_j}{\delta} \int d\tau \cos\left(\Theta_j(\tau) + \Phi_j^d(\tau)\right) \end{aligned} \tag{4.75}$$

We have defined the dual propagator M and dual vector potential Φ_j^d as,

$$M_{ij} = \left[\left(\frac{2\pi}{\omega}\right)^2 G_{ij}^{-1} \right] \tag{4.76}$$

$$\Phi_j^d(\omega) = \frac{\omega}{\pi} \sum_i M_{ij}(\omega)(\Phi_i(\omega) - 2\pi n_i \delta(\omega)) \tag{4.77}$$

We now write the partition function for the dual model that reproduces the strong tunneling instanton expansion. While writing the partition function of the model one has to sum over $n_1,\ n_2$ to account for the degenerate minima

of the potential.

$$\begin{aligned}\frac{Z}{Z_0} &= e^{-\frac{1}{4}\sum_{\omega,ij}\Phi_i^{d*}M_{ij}^{-1}\Phi_j^d}\Big[1+\frac{1}{4}\sum_{n_1,n_2}\sum_{ij}\frac{W_iW_j}{\delta^2} \\ &\times \int d\tau_1 d\tau_2 \cos(\Phi_i^d(\tau_1)-\Phi_j^d(\tau_2))\langle e^{i\Theta_j(\tau_1)}e^{-i\Theta_k(\tau_2)}\rangle\Big]\end{aligned} \tag{4.78}$$

Tunneling amplitude $W_j \sim \frac{1}{U_j}$ is the small parameter around which we do perturbation in the dual regime. This scale is set by the smearing of the instanton switching time scale. The quadratic term in vector potential corresponds to the zeroth order instanton expansion ($U = \infty$). Before calculating current due to first order in instantons, in the following section we calculate current in $U = \infty$ limit.

4.7 Current in $U = \infty$ limit

In this section we calculate the tunneling current for interferometers in strong tunneling regime when the tunneling amplitude $U = \infty$. In this limit fields are pinned to their minima and there is no instanton contribution. The action for this case is given by Eq. (4.69). Partition function is given by $Z = \sum_{n_1,n_2} e^{-\frac{1}{4}\sum_{\omega,ij}\Phi_i^{d*}M_{ij}^{-1}\Phi_j^d}$. Let us substitute Eq. (4.69) in to Eq. (4.53) and neglect fluctuations around the optimal configurations (4.69). The terms coming from n_j do not contribute to the tunneling current and hence can be dropped. In this regime the action and the partition function can be written as

$$S_0 = \frac{1}{4}\sum_{\omega,ij}\Phi_i^*(G^{-1})_{ij}\Phi_j \tag{4.79}$$

By taking variation with respect to Φ_k^* and analytically continuing to real time [3] we obtain current through point contact

$$I_k^\infty(\omega) = \frac{1}{2}\sum_j (G^{-1})_{kj}|_{ret}\Phi_j. \tag{4.80}$$

We have defined $\xi_{tot} = \sum_\sigma \xi^\sigma$. For the vector potential $\Phi_j(t) = Vt\theta(t)$ ($\Phi_j(\omega) = \frac{-iV}{(\omega+i0)^2}$) Now we can write the current expression as

$$I_k^\infty(t) = \frac{1}{2}\int \frac{d\omega}{2\pi i} e^{-i\omega t}\frac{V}{(\omega+i0)^2}\sum_j (G^{-1}_{\omega+i0})_{kj} \tag{4.81}$$

.

$$I_k^\infty(t) = \frac{\nu V}{2\pi}\int \frac{d\omega}{2\pi i} e^{-i\omega t}\frac{\omega+i0}{(\omega+i0)^2}\frac{1-\sum_{\sigma=1}^2 \frac{\nu}{\nu_\sigma} e^{i\omega\xi^\sigma}\theta(\omega\xi^\sigma_{j\neq k})}{(1-(1-a^2)e^{\sum_\sigma i\omega\xi^\sigma})} \tag{4.82}$$

$$I_k^\infty(t) = \frac{\nu V}{2\pi}\int \frac{d\omega}{2\pi i} e^{-i\omega t}\frac{1}{(\omega+i0)}\frac{1-\sum_{\sigma=1}^2 \frac{\nu}{\nu_\sigma} e^{i\omega\xi^\sigma}\theta(\omega\xi^\sigma_{j\neq k})}{(1-(1-a^2)e^{i\omega\sum_\sigma \xi^\sigma})} \tag{4.83}$$

We now define $\xi_{tot} = \sum_\sigma \xi^\sigma$ Now we expand the exponential in the denominator (note that the ω in the exponential is regulated by a positive imaginary part that allows us to expand) and write the expression for the current as,

$$I_k^\infty(t) = \frac{\nu V}{2\pi}\sum_{n=0}^\infty (1-a^2)^n \int \frac{d\omega}{2\pi i}\frac{e^{-i\omega(t-n\xi_{tot})} - \sum_{\sigma=1}^2 \frac{\nu}{\nu_\sigma} e^{-i\omega(t-\xi^\sigma-n\xi_{tot})}\theta(\omega\xi^\sigma_{j\neq k})}{(\omega+i0)} \tag{4.84}$$

After performing the contour integral, we obtain the result for current as,

$$I_k^\infty(t) = \frac{\nu V}{2\pi}\sum_{n=0}^\infty (1-a^2)^n \left(\theta(t-n\xi_{tot}) - \sum_{\sigma=1}^2 \frac{\nu}{\nu_\sigma}\theta(t-\xi^\sigma-n\xi_{tot})\theta(\omega\xi^\sigma_{j\neq k})\right) \tag{4.85}$$

We note that the current completely switches directions from one point contact

[3] To obtain the retarded Green's function $(G^{-1})_{jk}|_{ret}$ we should analytically continue $i\omega \to \omega + i0$ which amounts to $|\omega| \to i\omega$ and $\theta(\omega\xi^\sigma_{ij}) \to \theta(\xi^\sigma_{ij})$ in 4.70

to another.

4.8 Current in $U < \infty$ limit

To calculate first order instanton contribution to the current we expand the resonance function appearing in the quasiparticle propagator in the following form,

$$\frac{1}{D(\omega)} = \sum_{m=0}^{\infty} (1-a^2)^m \; e^{-m\sum_\sigma |\omega\xi^\sigma|} \tag{4.86}$$

. Two point quasiparticle correlators can be written as,

$$\begin{aligned} \langle e^{i\Theta_j(\tau)} e^{-i\Theta_k(0)} \rangle &= e^{4\sum_\omega e^{i\omega\tau} \left(\frac{2\pi}{\omega}\right)^2 G^{-1}_{jk}} \\ &= \prod_{m=0}^{\infty} K^{qp}(\chi^1_{jk}(m), i\tau) K^{qp}(\chi^2_{jk}(m), i\tau) \end{aligned} \tag{4.87}$$

We have defined

$$\chi^\sigma_{jk}(m) = \left(\frac{\xi^\sigma_{jk}}{v_n} + m \; \mathrm{sgn}(\xi^\sigma_{jk}) \xi_{tot} \right), \; \xi_{tot} = \sum_\sigma |\xi^\sigma| \tag{4.88}$$

$$K^{qp}(\chi^\sigma_{jk}(m), i\tau) = \begin{cases} \left[\frac{1}{\chi^\sigma_{jk}(m) + i\tau)} \right]^{\frac{\nu^2(1-a^2)^m}{\nu_\sigma}} & (T=0) \\ \\ \left[\frac{\pi T}{v_\sigma \sinh \pi T(\chi^\sigma_{jk}(m) + i\tau)} \right]^{\frac{\nu^2(1-a^2)^m}{\nu_\sigma}}, & (T \neq 0) \end{cases} \tag{4.89}$$

Quasiparticle correlators in the above expression is general for both FP and MZ interferometers. Different geometries are classified by the parameter a. The current at any point on the edge in the dual picture is only modified by the point contact tunneling current in Eq. (4.58). In the dual limit tunneling

current at a point contact can be calculated by $\mathbf{I} = \frac{\delta \log \mathbf{Z}}{\delta \mathbf{\Phi^d}} \left\| \frac{\delta \mathbf{\Phi^d}}{\delta \mathbf{\Phi}} \right\|$.

$$\begin{aligned} I_k(t) &= \sum_{n_1,n_2} \sum_i \frac{W_i W_k}{2\delta^2} \int_{-\infty}^{t} dt_1 \left\| \frac{\delta \mathbf{\Phi^d}}{\delta \mathbf{\Phi}} \right\| \sin\left(\Phi_i^d(t_1) - \Phi_k^d(t)\right) \\ &\times Im\left(\prod_{m=0}^{\infty} \prod_{\sigma=1}^{2} K^{qp}(\chi_{ik}^{\sigma}(m), t_1 - t - i0) \right) + I_k^{\infty} \end{aligned} \tag{4.90}$$

4.8.1 Tunneling Current for the Mach Zehnder Interferometer

The tunneling current for the MZI in the dual limit simplifies as $D(\omega) = 1$. For this case, the tunneling current receives contribution from $m = 0$ term of the quasiparticle correlators. In other words, the quasiparticle interferometer model is self-dual to its electron counterpart up to a change of $\nu \rightleftarrows \frac{1}{\nu}$. This is because of the beam splitter geometry of MZI, where both the edges propagate in the same direction as shown in Fig. (4.2). Hence, for this case we can borrow results for current from weak tunneling and replace $\nu \to \frac{1}{\nu}$.

4.8.2 Tunneling current for the Fabry-Perot Interferometer

For the FPI geometry as shown in Fig. (4.2), one of the edges carries backward propagation of current. Due to this, part of the current is stuck in the loop between two contacts. This feature manifests itself in the quasiparticle correlation function as an infinite product over m cycles (see Eq. (4.87)). Hence the expression of current is proportional to this infinite product over cycles. This product can be simplified by considering currents calculated over some finite cycles of propagation. This is justified as the time scale of measurement can be chosen such that higher order feedbacks are not important.

4.8.3 Resonant tunneling current for the Fabry-Perot Interferometer (a=0, $\nu_1 = \nu_2$)

When we have two counterpropagating edges of the same filling factor, there is no effective chiral mode that kicks out current from the Fabry-Perot loop. This case reduces to an effective non-chiral action. In the strong-tunneling limit, the applied flux can also be tuned to resonance condition. This case was considered by Kim and Fradkin. A detailed analysis for tunneling currents in coherent and incoherent regimes is derived in Ref. [9]. Our model can be reduced to the effective non chiral model they consider by setting $a = 0$ in CL action.

4.9 Conclusions

In this chapter, we considered interferometer made of fractional quantum Hall edge state. In Sec. (B.1), we started from the Chern-Simons theory in an infinite strip. We construct gauge invariant form of the Chern-Simons theory which required two topologically protected massless (R, L) edge degrees of freedom. This construction enabled independent coupling of the gauge fields to each edge of the strip. We constructed interferometer by considering two FQH strip with two tunneling point contacts between them (given by boundary Sine-Gordon terms). As shown in the Fig. (4.2) depending on the chirality of the edges involved in the tunneling process, they can be classified into Mach-Zehnder and Fabry-Perot geometry. Edge excitations can be represented as chiral bosons. In Sec. (4.4) we construct Caldeira-Leggett (CL) type model for two point contact tunneling with careful treatment of compactness. We show that by taking compactness of chiral bosons in the path integral formalism, we can calculate the tunneling currents in both weak and strong tunneling regimes. The compactness condition resolves ambiguity involved in the matrix inversion of CL Greens function. We give general expressions for the current in both weak and strong tunneling limits for MZI and FPI. We obtain electron periodicity with adiabatic variations of flux in both weak and strong tunneling limits. Our results are in agreement with Averin and Ponomarenko who

used auxiliary fields to cancel ambiguous terms in chiral boson correlators. In the future, we will extend our analysis to construct and analyze topological quantum circuits made out of Caldeira-Leggett (CL) points on FQH edges. Current injection and measurement can be done using the generalized Chern-Simons gauge fields(see Sec. (B.1)) . We can realize non-trivial geometry of FQH edge networks and reconnections by simply allowing some CL points to be strong tunneling points. Our work can be easily extended to the Jain fractions that involve multiple edge modes. The interesting direction of future research would be to gain formal insight into how compactness affects chiral boson theory.

Chapter 5

Additional Project I: Fluctuation relations for current components in open electric circuits

In this work we derive a new class of fluctuation relations, to which we refer as *Fluctuation Relations for Current Components* (FRCCs). FRCCs can be used to estimate system parameters when complete information about nonequilibrium many-body electron interactions is unavailable. We show that FRCCs are often robust in the sense that they do not depend on some basic types of electron interactions and some quantum coherence effects. This chapter is based on the publication [13].

5.1 Introduction

Fluctuation theorems [108–112] are fundamental results in the nonequilibrium statistical mechanics. Their discovery led to optimism that they might serve as universal laws that had long been missing from the study of nonequilibrium systems. Fluctuation relations for currents [113–119] play a special role in the physics of non-equilibrium transport. Measurements of statistics of heat

production generally involve tracing stochastic trajectories of the complete system. This is often an experimentally challenging problem. Measurements of currents are relatively simple. Formally, a current can be found just from the knowledge about an initial and a final state of a system, and no separation of the measured system from the heat bath is required. Moreover, experimental studies of fluctuation theorems typically need large statistics of events because any Gaussian distribution of any variable trivially satisfies a standard fluctuation relation. Hence, nontrivial fluctuation relations can be identified only if statistics of events are obtained beyond the domain of Gaussian fluctuations. Non-Gaussian statistics in nanoscale conductors is due to the shot noise of electrons at non-equilibrium conditions [120, 121]. Recently, it became possible to experimentally study such non-Gaussian fluctuations in mesoscopic electric circuits [122, 123]. In application to an electric circuit with two lead contacts, the Fluctuation Theorem predicts that the probability distribution $P[q]$ of observing a charge q passed between two lead contacts with a voltage difference V satisfies the law [113]:

$$P[q]/P[-q] = e^{Fq}, \tag{5.1}$$

where $F = V/k_{\mathrm{B}}T$. Here T is the temperature, and k_{B} is Boltzmann's constant. Eq. (5.1) is expected to be universal, i.e. it should be valid independently of the type of electron interactions in a conductor. Surprisingly, recent experimental work [12] has shown that the law (5.1) can fail in an electric circuit, but could be salvaged under the experimental conditions of [12] if the parameter F is suitably renormalized by a factor $\sim 10^{-1}$.

The need to modify (5.1) was qualitatively explained in [12] by the presence of a feedback between measured and measuring circuits. For example, in the experiment [12], the nanoscale circuit was connected to a read-out circuit made of an additional tunnel junction, which was coupled to its own leads. When interactions between measured and measuring currents are involved, the fluctuation theorem is applicable only to the *total system* that includes both the studied circuit and the measuring one but this does not imply (5.1) for a single current component any more.

This argument only partly explains the experimental result in [12] because it makes unclear why, after considerable renormalization of parameters, an individual current through a specific lead contact again satisfies (5.1). For example, according to Crook's equality, the heat W, dissipated by a complete system, satisfies the relation

$$P[W]/P[-W] = \exp\left(W/k_{\mathrm{B}}T\right). \tag{5.2}$$

We can introduce the vectors, $\boldsymbol{q}$ and $\boldsymbol{V}$, whose components are, respectively, the numbers of electrons passed through individual lead contacts, and individual voltages at corresponding leads, whereby the number of vector components is equal to the number of independent lead contacts in the circuit. The dissipated heat can then be expressed as $W = \boldsymbol{V}\cdot\boldsymbol{q}$, which corresponds to the standard fluctuation relation for multicomponent current [113–119]:

$$P[\boldsymbol{q}]/P[-\boldsymbol{q}] = \exp\left(\boldsymbol{V}\cdot\boldsymbol{q}/k_{\mathrm{B}}T\right). \tag{5.3}$$

Apparently, a specific current component q_k is not proportional to the dissipation function W because the latter depends on all current components. Consequently, although the full vector of currents satisfies Eq.(5.3) there seems to be no reason why an individual current through a specific lead contact should satisfy a fluctuation relation (5.1) in a multicomponent system.

The appearance of fluctuation relations (5.1) for specific current components at renormalized values of parameters remains poorly understood. Recent studies [124] showed that *Fluctuation Relations for Current Components* (FRCC)s, i.e. for currents through specific links of a circuit, can appear in some limits of a model that corresponds to a 4-state Markov chain kinetics. However, generalizations of this result have been unknown. Another possibility to explain experimentally observed FRCC was based on a separation of time scales [12], i.e. if one current component is macroscopic in comparison to another one, the former can be considered as part of environment so that one can introduce an effective dissipation function for the second, microscopic, current component. Such an explanation, however, can be justified only in very

specific limits and for relatively simple circuit geometries.

In this chapter, we prove that there are, in fact, general conditions under which FRCCs should hold for currents through certain links in complex mesoscopic electric circuits coupled to multiple lead contacts. Unlike standard fluctuation theorems, there is no direct relation between FRCCs and the dissipated heat in a system. Instead, we will show that FRCCs follow from the observation that statistics of particle currents depends only on the probabilities of single-particle *geometric trajectories* while the information about time moments, at which particles make transitions along such trajectories, is irrelevant. Then, there can be purely topological constraints on contributions of geometric trajectories to currents through some links of a circuit. For example, if a link does not belong to any loop of a graph, and if transitions through this link in opposite directions are counted with opposite signs, then any geometric trajectory can make only ± 1 or 0 valued currents through such a link. We will show that this restricts the statistics of currents through this link to satisfy Eq. (5.1) even when there are no detailed balance constraints on kinetic rates. Another interesting topological constraint appears when there is only one reservoir that supplies/absorbs particles to/from the system. Then all single particle geometric trajectories have to be cyclic, and one can make a correspondence between currents through links and independent cycles that a trajectory makes. Probabilities of independent cycles are known to satisfy relations of type (5.1) [113–119], which eventually results in FRCCs in such a circuit. We will also show that FRCCs are robust against adding important many-body interactions because the latter influence timing but do not change relative probabilities of geometric trajectories.

The structure of this chapter is as follows. In Section 2, we will illustrate FRCCs in the model of a chaotic cavity, shown in Fig. 5.1, which frequently appears in studies of counting statistics [125, 126]. In Section 3, we will increase the complexity of the electric circuit geometry to demonstrate the ubiquity of FRCCs in mesoscopic electronics. Sections 4 and 5 play a supplementary role. They explore both the presence and absence of FRCCs in specific models, which statistics of currents can be studied in detail. They demonstrate that exactly solvable models produce results in agreement with the more general

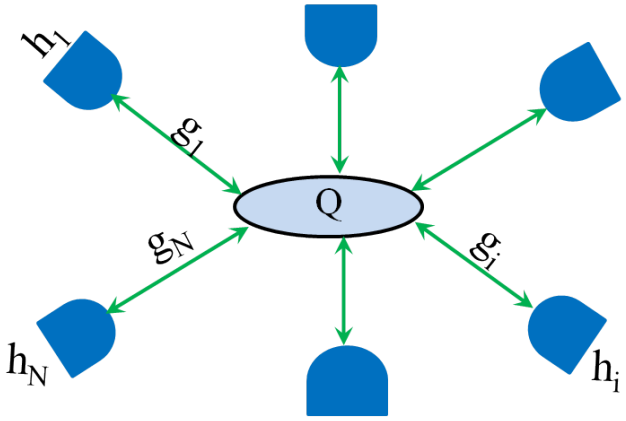

Figure 5.1: Chaotic cavity coupled to N electron reservoirs at different potentials and temperatures.

theory developed in Sections 2 and 3.

5.2 The model of chaotic cavity coupled to N lead contacts

The model assumes that N large reservoirs at different potentials exchange electrons with a mesoscopic conducting region (cavity), in which the electron motion is randomized and is influenced by exclusion interactions due to the Pauli principle and Coulomb interactions [125, 126]. The model also assumes that time-scales for self-averaging are much faster than the time-scale at which the number of electrons in a cavity changes with time so that we can treat interactions within a mean field approximation. Electrons enter the cavity through the lead contacts with kinetic rates, $k_i^{\rm in}(Q) = h_i g_i f_1(Q)$, and leave the cavity with rates $k_i^{\rm out}(Q) = g_i f_2(Q)$, where $i = 1, \ldots, N$. The parameter h_i depends on thermal equilibrium conditions in the i-th reservoir, g_i is a strength of the cavity coupling to the i-th contact, and Q is the instantaneous number of electrons in the cavity. The functions $f_1(Q)$ and $f_2(Q)$ describe the effect of many-body interactions on kinetic rates.

We assume that all parameters, as well as functions f_1 and f_2, may de-

pend on constant temperatures and potentials at reservoirs. As an example, first consider that the cavity is small (the quantum dot limit), so that it has only a single electron level at energy E. Coulomb interactions forbid to have more than one electron inside. The kinetic rate of escape of electron from this cavity into the ith contact can be estimated by the golden rule: $k_i^{\rm out} = 2\pi Q\rho_i(E)|T_i(E)|^2(1 - 1/[1 + e^{(E-V_i)/(k_{\rm B}T)}])$, where $Q = 1$ or $Q = 0$ depending on the presence or absence of an electron inside the quantum dot. $T_i(E)$ is the element of the scattering matrix between the state inside the quantum dot and a state in the reservoir at the same energy E, $\rho_i(E)$ is the density of energy levels inside the ith contact near energy E, and the factor $1 - 1/[1 + e^{(E-V_i)/(k_{\rm B}T)}]$ is due to the Pauli principle that forbids transitions into the filled states of the reservoir. Similarly, the kinetic rate of transitions from the ith reservoir into the quantum dot can be estimated as $k_i^{\rm out} = 2\pi(1 - Q)\rho_i(E)|T_i(E)|^2(1/[1 + e^{(E-V_i)/(k_{\rm B}T)}])$. We can then identify $g_i = 2\pi\rho_i(E)|T_i(E)|^2(1 - 1/[1 + e^{(E-V_i)/(k_{\rm B}T)}])$, $h_i = e^{-(E-V_i)/(k_{\rm B}T)}$, $f_1 = (1 - Q)$, and $f_2 = Q$. Another limit of the cavity model corresponds to a large cavity with kinetic rates induced by thermal over-barrier transitions and number of states inside the cavity that is much larger than the number of electrons. In such a classical limit, kinetic rates are given by the Arrhenius form $k_i^{\rm in} \sim e^{(V_i-W_i)/k_{\rm B}T}$, and $k_i^{\rm out} \sim e^{(\mu(Q)-W_i)/k_{\rm B}T}$, where W_i is the size of the barrier that separates the cavity from the ith reservoir and $\mu(Q)$ is the chemical potential of electrons inside the cavity. Then we can identify $g_i = e^{-W_i/k_{\rm B}T}$, $h_i = e^{V_i/k_{\rm B}T}$, $f_1 = 1$ and $f_2 = e^{\mu(Q)/k_{\rm B}T}$. Note that, in both cases, at constant temperature, the parameters h_i satisfy the relation

$$h_i/h_j = \exp\{(V_i - V_j)/k_{\rm B}T\}, \tag{5.4}$$

which guarantees the presence of the standard fluctuation relation (5.3). This restriction, however, will not play any role in our following discussion.

Let

$$Z(\boldsymbol{\chi}) \equiv e^{S(\boldsymbol{\chi})} = \sum_{\boldsymbol{q}} P(\boldsymbol{q}) e^{\boldsymbol{q}\cdot\boldsymbol{\chi}} \tag{5.5}$$

be the generating function of currents through all leads. Here components

of the N-vector, $\boldsymbol{q}$, are the number of electrons that pass through the corresponding contacts during the observation time. In the rest of the chapter, all introduced vectors will correspond to sets of elements indexed by the indices of the corresponding reservoirs, e.g. $\boldsymbol{\chi} = (\chi_1, \ldots \chi_N)$ is the vector of *counting parameters*. $S(\boldsymbol{\chi})$ is called the *cumulant generating function* because its knowledge corresponds to the knowledge of all cumulants of the current distribution, e.g.

$$\langle q_i \rangle = (\partial S/\partial \chi_i)_{\boldsymbol{\chi}=0}, \;\; \mathrm{var}(q_i) = (\partial^2 S/\partial \chi_i^2)_{\boldsymbol{\chi}=0}, \;\; \text{etc.} \tag{5.6}$$

We will detect FRCCs by setting all χ_i, where $i \neq k$ for some $k \in 1, \ldots, N$, to zero and observing the symmetry,

$$S(0, ..., 0, \chi_k, 0, ..., 0) = S(0, ..., 0, -\chi_k + F_k, 0, ..., 0), \tag{5.7}$$

where F_k, for a given k, is a constant parameter. By applying the inverse Legendre transform, one can verify that (5.7) leads to the FRCC,

$$P(q_k)/P(-q_k) = \exp(q_k F_k). \tag{5.8}$$

Let us calculate the probability, p_{ij}, of that the nearest entering electron will have a geometric trajectory that enters the cavity via the contact i and leaves the cavity via the contact j. Kinetic rates for this particle depend on Q, which may change with time arbitrarily, however, the *ratio* of either two in-going or two outgoing kinetic rates for the given particle remains constant, which means that the probability of the geometric trajectory for this particle can be found explicitly:

$$p_{ij} = \frac{h_i g_i}{\sum_{k=1}^{N} h_k g_k} \times \frac{g_j}{\sum_{r=1}^{N} g_r}. \tag{5.9}$$

Let $P(n)$ be the probability that during a large observation time exactly n electrons enter the cavity via any node. The probability of a geometric trajectory in (5.9) is independent of n and of other particle's trajectories, such that

the generating function $Z(\boldsymbol{\chi})$ is given by

$$Z(\boldsymbol{\chi}) = \sum_{n=0}^{\infty} P(n) \left(\sum_{i,j=1}^{N} p_{ij} e^{\chi_i - \chi_j} \right)^n . \tag{5.10}$$

Although it is impossible to derive an explicit expression for $P(n)$, one can check that the symmetry (5.7) is the symmetry of each term in (5.10) with

$$F_k = \ln \left(\frac{\sum_{i \neq k}^{N} g_i h_i}{h_k \sum_{i \neq k}^{N} g_i} \right), \quad k = 1, \ldots, N, \tag{5.11}$$

which proves the FRCC for the cavity model.

Note that the parameters $\boldsymbol{F}$ depend not only on the lead characteristics $\boldsymbol{h}$, which can be externally controlled, but also on the coupling parameters $\boldsymbol{g}$. The latter may nontrivially depend on voltages due to appearance of screening charges in the vicinity of components of the nanoscale circuit at nonequilibrium conditions [127]. Estimation of parameters $\boldsymbol{g}$ from knowledge of lowest current cumulants may be difficult because functions $f_1(Q)$ and $f_2(Q)$ influence lowest current cumulants. Surprisingly, the FRCCs do not depend on interactions encoded in functions $f_1(Q)$ and $f_2(Q)$ at all. Hence measurements of FRCCs can provide us with a unique approach to measure the vector $\boldsymbol{g}$ in a nonequilibrium regime irrespective of many-body interactions inside the cavity.

We also note that our derivation of the generating function is valid only for a very large observation time, so that we could disregard the trajectories of electrons that entered but did not leave the cavity. Thus, FRCCs must be understood only in the sense of the dominating exponent (also known as the Large Deviation Function) of the probability distribution of a current.

5.3 Stochastic transport on networks

To explore general principles that lead to FRCCs, we consider a generalization of the cavity model to a network of chaotic cavities coupled to lead contacts and to each other, e.g. as shown in Fig. 5.2. Electrons enter cavities through

the reservoirs (with the rate $h_i g_i$ for the i-th cavity). If two cavities (graph nodes) i and j are connected, each electron in the node i can make a transition to node j with rate g_{ij}; generally, $g_{ij} \neq g_{ji}$. Eventually, electrons leave the network through one of the contacts. The physics of incoherent effects due to the shot noise and thermal Johnson-Nyquist noise in continuous conductors can be obtained from the continuous limit of such network models [128, 129].

For simplicity, we assume that all electrons are non-interacting, i.e. $f_1^i = 1$ and $f_2^i = Q_i$ for all cavities, although generalizations to local interactions ($f_2^i(Q_i) \neq Q_i$) are possible because such interactions do not change the relative probabilities of the geometric trajectories [130]. It was shown in [130] that finding statistics of currents in such a model reduces to solving a finite set of coupled linear algebraic equations. Although explicit solutions are bulky and not illuminating, we used them to check the presence/absence of an FRCC for any link of a network numerically, as we explain in Section 5. As expected, we *did not* find an FRCC when there was no previously mentioned topological constraints on geometric trajectories. However, FRCCs were obtained in two wide classes of links with such constraints.

5.3.1 Links that do not belong to any loop of the network

These links represent lead contacts and also internal links of the network that on removal break the network into disjoint components. We marked such links by green color in Fig. 5.2. Suppose that we can trace the geometric trajectory of a single electron. When the electron enters the network, it makes a single transition through a lead contact in the positive direction and then makes one transition through one of the leads in the negative direction when it leaves the network. Let p_{kj} be the probability that the electron that enters through the contact k leaves the network through the contact j. If an electron enters through the contact k, then the moment-generating function of currents through the contact k that this electron produces during its life-time is given

by

$$Z_k(\chi_k) = p_{kk} + \sum_{j \neq k} p_{kj} e^{\chi_k}. \tag{5.12}$$

The generating function of currents in the contact k, which is produced by an electron that enters from contact j, $j \neq k$, is given by

$$Z_j(\chi_k) = \sum_{j' \neq k} p_{jj'} + p_{jk} e^{-\chi_k}. \tag{5.13}$$

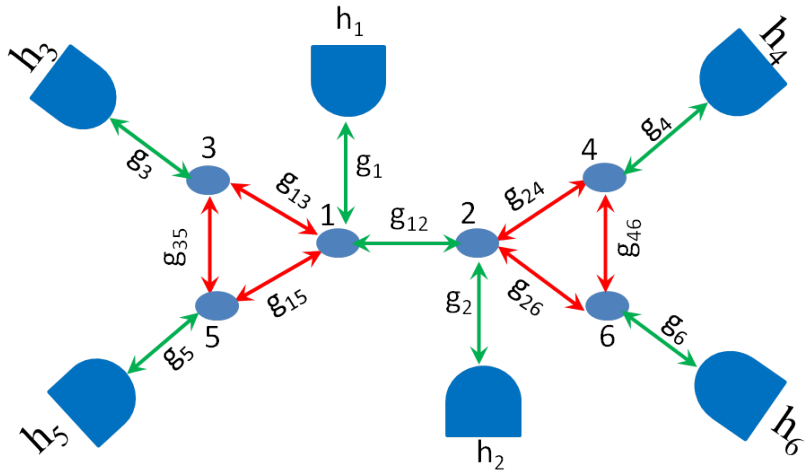

Figure 5.2: Circuit of coupled chaotic cavities and electron reservoirs. the green color marks links that carry currents that satisfy FRCCs. The red color marks links with currents that violate FRCCs.

Let $P_{q_1,\ldots,q_N}(t)$ be the probability that during time t exactly $q_1, \ldots, q_N$ particles enter the network through the contacts $1, \ldots, N$. Since particles enter independently, this distribution is, in fact, Poissonian, and its generating function is given by

$$Z_P(\boldsymbol{s}) \equiv \sum_{\boldsymbol{q}} P_{\boldsymbol{q}} e^{\boldsymbol{sq}} = \exp\left(\sum_{i=1}^{N} h_i g_i t (e^{s_i} - 1) \right). \tag{5.14}$$

Since electrons do not interact,the probabilities $P_{q_1,\ldots,q_N}(t)$ and p_{kj} are not correlated. The statistics of currents through the contact k during the whole

process is then given by

$$Z(\chi_k) = \sum_{\boldsymbol{q}} P_{q_1,\ldots,q_N} Z_1^{q_1} \cdot \ldots \cdot Z_N^{q_N}, \tag{5.15}$$

where we used the fact that the generating function of a sum of independent processes is the product of generating functions of the individual processes. The latter expression shows that $Z(\chi_k)$ coincides with $Z_P(\boldsymbol{s})$ up to a change of variables $e^{s_i} \to Z_i(\chi_k)$ for any i. This fact and the explicit expressions for $Z_P(\boldsymbol{s})$ and $Z_i(\chi_k)$ lead us to the conclusion that the total generating function of currents depends on χ_k only through the combination, $h_k g_k \sum_{j\neq k} p_{kj} e^{\chi_k} + \sum_{j\neq k} h_j g_j p_{jk} e^{-\chi_k}$, which has the symmetry under the change of variables, $\chi_k \to -\chi_k + F_k$, where

$$F_k = \ln\left(\frac{\sum_{j\neq k} h_j g_j p_{jk}}{h_k g_k \sum_{j\neq k} p_{kj}}\right). \tag{5.16}$$

The case with a link that connects two otherwise disjoint components, α and γ, is proved similarly: Let p_α be the probability that a given particle that enters the network in the components α leaves the network through some contact in another graph component γ. The generating function of currents through the link that connects such components is $Z_\alpha(\chi) = (1 - p_\alpha) + p_\alpha e^{\chi}$. The rest of the proof is the same as for the currents through lead contacts, where instead of contact indices k and j we write component indices α and γ.

5.3.2 Quantum coherence among trajectories

So far we assumed the lack of quantum interference among particle trajectories. The arguments leading to (5.7) and (5.16) for a particle's motion on a network, however, do not refer to any classical or thermodynamic reason. For example, one can imagine that the distribution of electrons in the leads is not at equilibrium and that the probabilities p_{ij} are influenced by the quantum interference of different trajectories that connect nodes i and j. We just should assume that (a) events of particle's escapes into reservoirs destroy coherence, (b) particles enter the network according to the Poisson statistics, and

(c) the transition probabilities p_{ij} are constant. Such conditions are realized in the quantum regime when the single-electron scattering amplitude, $s_{ij}(E)$, between any pair of different reservoirs i and j in a channel with any energy E, is small, i.e. $|s_{ij}(E)| \ll 1$. In this limit, we can disregard simultaneous multi-electron scattering processes, although purely quantum effects, such as quantum interference of trajectories, can still influence s_{ij}.

The generating function for N terminals and non-interacting fermions was derived by Levitov and Lesovik [11]. In their determinant formula for the generating function, we can set only a single counting parameter, χ_k, to be non-zero. Then, for an arbitrary scattering matrix, the cumulant generating function of a current through a corresponding reservoir is given by

$$S(\chi_k) = \ln\left(\prod_E (C_k(E) + A_k(E)e^{\chi_k} + B_k(E)e^{-\chi_k})\right), \tag{5.17}$$

where A_k, B_k, and C_k are constants that depend on multielectron scattering amplitudes and channel populations. According to the golden rule, in the limit of weak transmission, coefficients A_k and B_k can be approximated to first order in $|s_{jk}|^2$ as

$$A_k(E) = \sum_{j\neq k} n_k(E)(1 - n_j(E))|s_{kj}|^2 \tag{5.18}$$

and

$$B_k(E) = \sum_{j\neq k} (1 - n_k(E))n_j(E)|s_{jk}|^2. \tag{5.19}$$

Here $n_i(E)$ is population of the channel with energy E in the i-th contact. Moreover, in this limit, we can use $\ln(1 + x) \approx x$ to approximate

$$\begin{aligned} S(\chi_k) \approx \sum_{j\neq k}\sum_E |s_{kj}|^2(1 - n_k)n_j(e^{-\chi_k} - 1) + \\ \sum_{j\neq k}\sum_E |s_{kj}|^2 n_k(1 - n_j)(e^{\chi_k} - 1). \end{aligned} \tag{5.20}$$

Hence, the counting statistics of individual contact currents of non-interacting

electrons is equivalent to a sum of two Poisson processes,

$$S(\chi_k) = A_k(e^{\chi_k} - 1) + B_k(e^{-\chi_k} - 1). \tag{5.21}$$

This generating function is symmetric under exchange $\chi_k \to -\chi_k + F_k$ and leads to an FRCC with

$$F_k = \ln\left(\frac{\sum_E (1 - n_k(E)) \sum_{j\neq k} |s_{kj}(E)|^2 n_j(E)}{\sum_E n_k(E) \sum_{j\neq k} |s_{kj}(E)|^2 (1 - n_j(E))}\right). \tag{5.22}$$

5.3.3 Networks connected to a single reservoir

A circuit that is coupled to a single particle reservoir, such as shown in Fig. 5.3(a,b), is another class of systems that show FRCCs for currents through some links that, in contrast to the previous case, belong to loops of the graph. Such networks can be used to describe the statistics of single molecule events [131]. For example, the graph in Fig. 5.3(a) corresponds to the kinetics of a biological enzyme [131] where the external link corresponds to the process of enzyme creation/degradation [130]. The probabilities of geometric trajectories in such open networks depend only on kinetic rates and not on time moments of individual transitions through links [130]. Consider, for example, the model

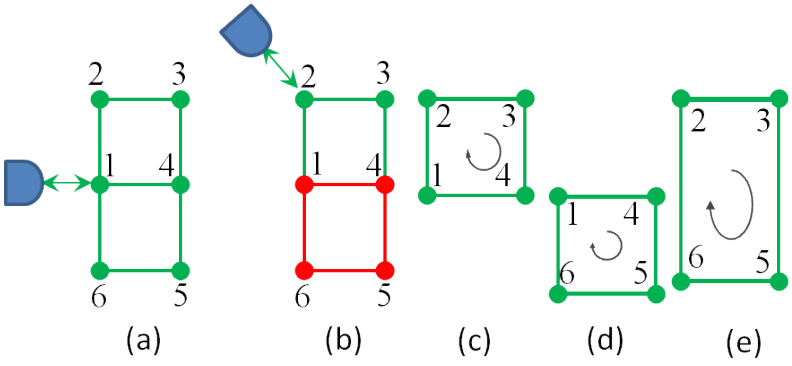

Figure 5.3: (a) and (b): Networks coupled to a single reservoir. Green links carry currents that satisfy FRCC and red links carry currents that generally do not satisfy FRCC. (c), (d) and (e): Distinct cycles of the graph. Cyclic arrows define "+" directions of cycles.

in Fig. 5.3(a) where we will be interested in currents through the link that

connects nodes 4 and 1. The arguments in Section 3A lead for this model to a conclusion that it is sufficient to prove the FRCC for currents produced by a single particle during its life-time because the symmetry of a single particle generating function becomes the symmetry of the full counting statistics of currents when there is only one external particle reservoir. Consider a particle that just appeared on the node 1 on a graph in Fig. 5.3(a). Let r be the kinetic rate of the transition of this particle from node 1 to the reservoir and let k_{ij} be kinetic rates of transitions between a pair of nodes, i and j. From the node 1, the particle can return to the reservoir with probability

$$p_{\rm esc} = r/(r + k_{12} + k_{16} + k_{14}), \tag{5.23}$$

producing no currents in the system, or it can move into another node. In the latter case, we know that the particle must eventually return to the node 1 because it is the only place from which it can escape from the network, and our measurement time is assumed to be much larger than the particle's life-time on the graph.

Each particle's return to node 1 corresponds either to making none or one of three possible cycles [131], shown in Fig. 5.3(c,d,e). Each cycle can be passed in two directions, that we will mark "+" or "−". Let p_0, $\eta_{1\pm}$, $\eta_{2\pm}$, and $\eta_{3\pm}$ be probabilities of such return events, where indices $1, 2, 3$ correspond to cycles in Fig. 5.3, respectively, (c), (d), and (e). These probabilities depend only on kinetic rates, i.e. they are constants [130]. The generating function of currents through the link $(4, 1)$, produced by all geometric trajectories that make exactly one return to node 1 is then given by

$$\begin{aligned} Z_1(\chi_{41}) = (1 - p_{\rm esc})p_{\rm esc}[p_0 + \eta_3 + \eta_{-3} + \\ (\eta_1 + \eta_{-2})e^{\chi_{41}} + (\eta_{-1} + \eta_2)e^{-\chi_{41}}]. \end{aligned} \tag{5.24}$$

After each return to the node 1 the process starts over. Hence the generating function produced by all trajectories that make exactly n returns to the node

1 is given by

$$Z_n(\chi_{41}) = p_{\rm esc}[(1-p_{\rm esc})(p_0+\eta_3+\eta_{-3}+ \\ (\eta_1+\eta_{-2})e^{\chi_{41}}+(\eta_{-1}+\eta_2)e^{-\chi_{41}})]^n. \tag{5.25}$$

The total single particle generating function is the sum over current generating functions, induced by all geometric trajectories, i.e.

$$Z(\chi_{41}) = \sum_{n=0}^{\infty} Z_n(\chi_{41}), \tag{5.26}$$

which explicitly can be written in a form

$$Z(\chi_{41}) = p_{\rm esc}/[1-(1-p_{\rm esc})(Ae^{\chi_{41}}+Be^{-\chi_{41}}+C)], \tag{5.27}$$

where $A=\eta_1+\eta_{-2}$, $B=\eta_{-1}+\eta_2$, $C=p_0+\eta_3+\eta_{-3}$. Eq. (5.27) is invariant under change of variables, $\chi_{41}\to-\chi_{41}+F_{41}$, where

$$F_{41} = \ln([\eta_{-1}+\eta_2]/[\eta_1+\eta_{-2}]), \tag{5.28}$$

which completes our derivation of the FRCC for the link $(4,1)$. One can easily extend our arguments to all green links in Figs. 5.3(a,b).

5.4 Exactly solvable models

In this section, we derive an explicit expression for the generating function of currents in the cavity model in several important limits and check the presence of FRCC explicitly. We show that the results are in full agreement with the symmetry described by (5.7) and (5.11).

5.4.1 Stochastic path integral solution of the chaotic cavity model

To derive FRCCs for the model in Fig. 5.1, we will employ the stochastic path integral technique [125, 126, 132, 133] that was previously applied to calculations of current cumulants and studies of standard fluctuation theorems in the cavity model. This approach is applied to the case of a cavity with mesoscopic size so that typically we have $Q \gg 1$. Following this approach, the counting statistics at a steady state is $S(\boldsymbol{\chi}) = Ht$, where $H = H(\boldsymbol{\chi}, Q_c(\boldsymbol{\chi}), \chi_c(\boldsymbol{\chi}))$ is given by

$$H = \sum_{i=1}^{N} k_i^{\text{in}}(Q_c)(e^{\chi_i+\chi_c} - 1) + k_i^{\text{out}}(Q_c)(e^{-\chi_i-\chi_c} - 1), \tag{5.29}$$

where Q_c and χ_c are expressed through $\boldsymbol{\chi}$ by solving steady state "Hamiltonian equations",

$$\partial H/\partial Q_c = 0, \quad \partial H/\partial \chi_c = 0. \tag{5.30}$$

To explore those equations, it is convenient to introduce combinations of parameters,

$$a(\boldsymbol{\chi}) = \sum_{i=1}^{N} h_i g_i \exp(\chi_i), \tag{5.31}$$

$$b(\boldsymbol{\chi}) = \sum_{i=1}^{N} g_i \exp(-\chi_i). \tag{5.32}$$

The Hamiltonian equations then explicitly lead to the relations

$$\exp(\chi_c) = [bf_2/af_1]^{1/2}, \tag{5.33}$$

$$f_1'(\sqrt{ab}\sqrt{f_2/f_1} - a(\mathbf{0})) + f_2'(\sqrt{ab}\sqrt{f_1/f_2} - b(\mathbf{0})) = 0, \tag{5.34}$$

where the functions f_1 and f_2 were defined in Section 2. Generally, such nonlinear equations cannot be solved explicitly to determine Q_c and χ_c, but they do imply that Q_c, as well as combinations ae^{χ_c} and $be^{-\chi_c}$, and hence H and S depend on counting parameters only via the product, $a(\boldsymbol{\chi})b(\boldsymbol{\chi})$.

It is then straightforward to verify that the symmetry, $S(0,\ldots,\chi_k,\ldots,0) = S(0,\ldots,-\chi_k+F_k,0,\ldots)$, is also the symmetry of $a(\boldsymbol{\chi})b(\boldsymbol{\chi})$ with

$$F_k = \ln\left(\frac{\sum_{i\neq k}^{N} g_i h_i}{h_k \sum_{i\neq k}^{N} g_i}\right), \quad k = 1,\ldots,N, \tag{5.35}$$

which proves the FRCC for the cavity model in the limit of mesoscopic cavity size.

The scope of the path integral technique is limited to mesoscopic systems. However, we could explicitly verify that the FRCC holds true in two exactly solvable limits. In the following subsections, we show exactly that Eq. (5.11) is satisfied for a cavity with exclusion interactions ($f_1 = Q_{\max} - Q$, $f_2 = Q$), and in the classical limit in which the number of available states in the cavity is much larger than the number of electrons so that in-going rates are not influenced by the Pauli principle ($f_1 = 1$ and arbitrary $f_2(Q)$).

5.4.2 Exact solution of cavity model with exclusion interactions

Here we consider the cavity model with N lead contacts. Electrons do not interact with each other except via the exclusion interactions due to the Pauli principle. Electrons enter the cavity through a lead contact i ($i = 1,\ldots,N$) with a kinetic rate, $k_i^{\text{in}}(Q_c) = h_i g_i (Q_{\max} - Q_c)$, and leave the cavity with a rate $k_i^{\text{out}}(Q_c) = g_i Q_c$. The latter rate is proportional to the number of electrons Q_c in the cavity. This corresponds to non-interacting case. We are interested in the statistics of currents through a specific lead contact, k. Our exact solution of this model is based on the observation that the model is equivalent to the model of independent currents through $Q_{\max}$ quantum dots [133, 134]. Each dot can have either zero or maximum one electron inside. If there is no electron in the dot then with rates $h_i g_i$, where $i = 1,\ldots,N$, an electron jumps into the dot. If the dot has an electron inside, then with rates g_i, $i = 1,\ldots,N$, it leaves to one of the leads. The calculation of the cumulant generating function at steady state in such a two-state model is straightforward and was discussed

in a number of publications, e.g. [135–138] with a minor difference that here, we assume many lead contacts. Following e.g. [137], the cumulant generating function is given by the larger eigenvalue of the matrix

$$H = \begin{pmatrix} -\sum_{i=1}^{N} h_i g_i & \left(\sum_{i\neq k}^{N} g_i\right) + g_k e^{-\chi_k} \\ \left(\sum_{i\neq k}^{N} h_i g_i\right) + h_k g_k e^{\chi_k} & -\sum_{i=1}^{N} g_i \end{pmatrix}. \tag{5.36}$$

Its eigenvalue, λ_0, can be explicitly written as

$$\lambda_0 = \frac{1}{2}(-K + \sqrt{K^2 + 4g_k(h_k g_k + e^{-\chi_k} A + e^{\chi_k} h_k B)}, \tag{5.37}$$

where $A = \sum_{i\neq k}^{N} h_i g_i$, $B = \sum_{i\neq k}^{N} g_i$, and K is independent of χ_k constant. Since the model of the cavity with exclusion interactions is equivalent to $Q_{\max}$ independent processes, each having counting statistics $\lambda_0(\chi)t$, the cumulant generating function for the complete model is given by

$$S(\chi_k) = Q_{\max}\lambda_0(\chi_k)t. \tag{5.38}$$

Obviously, $\lambda_0(\chi)$ is symmetric under exchange $\chi_k \to -\chi_k + F_k$, where F_k is given by

$$F_k = \ln\left(\frac{\sum_{i\neq k}^{N} g_i h_i}{h_k \sum_{i\neq k}^{N} g_i}\right), \tag{5.39}$$

in agreement with (5.11).

5.4.3 Exact solution of the cavity model for stochastic transitions with local interactions

Another exactly solvable model corresponds to a system of locally interacting particles performing stochastic transitions through a cavity connected to N reservoirs (See Fig. 5.1) with constant in-going kinetic rates. Let a state vector, $|Q_c\rangle$, be determined by an occupation number Q_c, associated with the

cavity. Kinetic rates for transitions from the cavity to the i-th reservoir is given by

$$k_i^{\text{out}} = Q_c f_c(t, Q_c) g_i, \tag{5.40}$$

where $f_c(Q_c)$ describes arbitrary local repulsive interactions inside the cavity that influence the out-going kinetic rates by renormalizing the single electron free energy in the mean field approximation. The in-going kinetic rate through the i-th reservoir is

$$k_i^{\text{in}} = h_i g_i. \tag{5.41}$$

Here, for generality, we can also allow an arbitrarily prescribed explicit periodic time-dependence of $\boldsymbol{h} = (h_1, h_2, \ldots h_N)$ with period τ, keeping the other parameters constant. A particle distribution function $P(Q_c)$ can be written as a state vector

$$\Psi = \sum_{Q_c} P(Q_c)|Q_c\rangle \tag{5.42}$$

that satisfies the master equation

$$\partial\Psi/\partial t = \hat{\mathcal{L}}\Psi. \tag{5.43}$$

To derive the counting statistics of currents, we should consider an evolution with a *twisted master operator*, $\hat{\mathcal{L}}_{\boldsymbol{\chi}}$ that can be obtained from the operator $\hat{\mathcal{L}}$ by multiplying its off-diagonal elements by factors $e^{\pm\chi_i}$ to count transitions from/to reservoir i. For details see Refs. [130, 136]. Following those rules, for our cavity model, we obtain the form of the twisted master operator:

$$\hat{\mathcal{L}}_{\boldsymbol{\chi}} = -\sum_j g_j[\hat{a}_c^\dagger(f_c(\hat{Q}_c)\hat{a}_c - \quad h \quad {}_j e^{\chi_j}) \tag{5.44}$$

$$+h_j - f_c(\hat{Q}_c)\hat{a}_c \quad e \quad {}^{-\chi_j}], \quad \hat{Q}_c = \hat{a}_c^\dagger \hat{a}_c, \tag{5.45}$$

where we have used the "second quantized" version of the master equation with

$$\hat{a}_c^\dagger|Q_c\rangle = |Q_c + 1\rangle, \quad \hat{a}_c|Q_c\rangle = Q_c|Q_c - 1\rangle \tag{5.46}$$

being the creation/annihilation operators. Here we note that the operator $\hat{\mathcal{L}}_{\boldsymbol{\chi}}$ in (5.44) is generally non-quadratic in $\hat{a}_c^\dagger$ and $\hat{a}_c$, which is the result of many-body interactions inside the cavity. For the case with local particle interactions, it becomes easier to obtain the solutions for the master equation by looking not at evolutions of the ket-vector but rather at the backward in time evolution of the bra-vector $\langle\Psi_{\boldsymbol{\chi}}(t)|$ given by [130]

$$\frac{\partial\langle\Psi_{\boldsymbol{\chi}}|}{\partial t} = -\langle\Psi_{\boldsymbol{\chi}}|\hat{\mathcal{L}}_{\boldsymbol{\chi}}(t), \;\; \langle\Psi_{\boldsymbol{\chi}}(t+\tau)| = \langle\Psi_{\boldsymbol{\chi}}(t)|e^{-S(\tau)}. \tag{5.47}$$

According to [130, 136, 137], the largest $S(\tau)$ in (5.47) coincides with the cumulant generating function (CGF) of currents per period of the parameter evolution in the $t \to \infty$ limit. Following [130], we will search for the solution of (5.47) in the form of a coherent state bra-vector

$$\langle\Psi_{\boldsymbol{\chi}}(t)| = \langle 0|\exp(\zeta_c\hat{a}_c)e^{-S(t)}, \tag{5.48}$$

and substitute this ansatz in Eq. (5.47). Using the property that

$$\langle\Psi_{\boldsymbol{\chi}}(t)|\hat{a}_c^\dagger = \langle\Psi_{\boldsymbol{\chi}}(t)|\zeta_c, \tag{5.49}$$

and then grouping separately terms near $\langle\Psi_{\boldsymbol{\chi}}(t)|f_c(\hat{Q}_c)\hat{a}_c$ and separately the remaining functions that multiply $\langle\Psi_{\boldsymbol{\chi}}(t)|$, we find that Eq. (5.47) is satisfied if

$$\zeta_c = \frac{\sum_j g_j e^{-\chi_j}}{\sum_j g_j}, \tag{5.50}$$

$$dS/dt = \sum_j g_j h_j(t)(e^{\chi_j}\zeta_c - 1). \tag{5.51}$$

Only the parameters h_j in (5.51) are time-dependent. It is then trivial to integrate (5.51) to find

$$S(\tau, \boldsymbol{\chi}) = \sum_j g_j \bar{h}_j(e^{\chi_j}\zeta_c - 1), \tag{5.52}$$

where we defined $\bar{h}_j \equiv \int_0^\tau h(t')dt'$. We can now write $S(\tau, \boldsymbol{\chi})$ explicitly as

$$S(\tau, \chi_k) = \frac{\sum_{jk} \bar{h}_k g_k g_j (e^{-\chi_j + \chi_k} - 1)}{\sum_j g_j}. \tag{5.53}$$

To illustrate the presence of the FRCC, we write $S(\tau, \boldsymbol{\chi})$ for individual counting fields by setting $\chi_j = 0$ for $j \neq k$, then

$$S(\tau, \chi_k) = C + B_k e^{-\chi_k} + A_k e^{\chi_k}, \tag{5.54}$$

where $C = \frac{\sum_{jk} \bar{h}_j g_k g_j}{\sum_j g_j}$, and

$$A_k = \frac{\bar{h}_k g_k \sum_{j \neq k} g_j}{\sum_j g_j},\ B_k = \frac{g_k \sum_{j \neq k} \bar{h}_j g_j}{\sum_j g_j}. \tag{5.55}$$

The form of CGF in Eq. (5.54) has the symmetry under the exchange of $\chi_k \to -\chi_k + F_k$, where F_k is given by

$$F_k = \ln \left(\frac{\sum_{j \neq k}^N g_j \bar{h}_j}{\bar{h}_k \sum_{j \neq k}^N g_j} \right). \tag{5.56}$$

This expression for F_k is the same as (5.11).

5.5 Numerical Check of the FRCC for Networks

In this section, we consider more complex networks and analyze the validity of the FRCC for any particular link numerically.

5.5.1 Network with loops and backbone link

Consider a graph that is coupled to external particle reservoirs and has loops and a backbone link as shown in Fig. 5.2. For numerical check we restrict ourselves to models with only one reservoir per node. Generalizing the cavity model we define additional parameters that are the kinetic rates of transitions

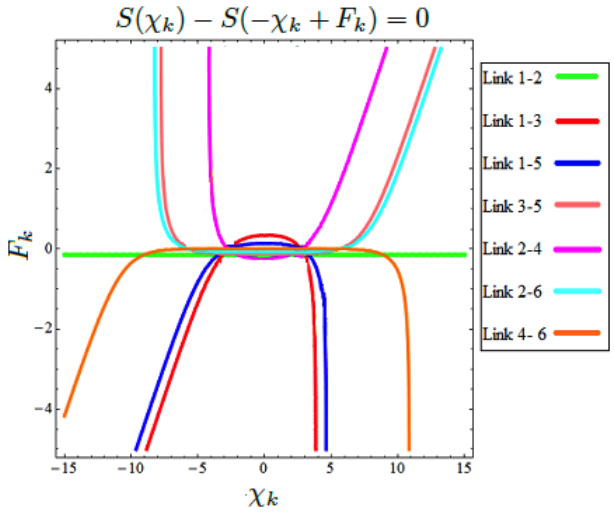

Figure 5.4: Numerical plots for the solution contours of $S(\chi) - S(-\chi + F) = 0$ for currents in geometry of Fig. 5.2. Parameters were set to numerical values: $g_{12} = 0.3854$, $g_{13} = 0.6631$, $g_{15} = 0.5112$, $g_{35} = 0.6253$, $g_{24} = 0.17483$, $g_{26} = 0.02597$, $g_{46} = 0.931946$, $g_{ij} = g_{ji}$, $g_1 = 0.5379$, $g_2 = 0.004217$, $g_3 = 0.8144$, $g_4 = 0.8396$, $g_5 = 0.1765$, $g_6 = 0.8137$, $h_1 = 8.7139$, $h_2 = 8.8668$, $h_3 = 4.6144$, $h_4 = 8.1632$, $h_5 = 7.6564$, and $h_6 = 8.01407$.

from node i to node j, given by $k_{ij} = Q_i f_i g_{ij}$. The twisted master operator for this case can be written as [130]

$$\begin{aligned} \hat{\mathcal{L}}_{\boldsymbol{\chi}} &= \sum_{jk} g_{jk} \hat{a}_j^\dagger (e^{\chi_{jk}} f_k \hat{a}_k - f_j \hat{a}_j) \\ &- \sum_j g_j [\hat{a}_j^\dagger (f_j \hat{a}_j - h_j e^{\chi_j}) + h_j - f_j \hat{a}_j e^{-\chi_j}], \end{aligned} \tag{5.57}$$

where we introduced additional parameters χ_{ij} to count currents through internal links (i, j). Following the prescription for the case of the single cavity (node) model we obtain the CGF, $S(\chi_{jk}, \chi_k)$, which reads:

$$S(\tau, \boldsymbol{\chi}) = \sum_j g_j \bar{h}_j (e^{\chi_j} \zeta_j - 1), \tag{5.58}$$

where parameters $\zeta_j' s$ can be obtained by the solving following set of linear equations:

$$\sum_j g_{jk}(e^{\chi_{jk}}\zeta_j - \zeta_k) - g_k(\zeta_k - e^{-\chi_k}) = 0. \tag{5.59}$$

Explicit functional form of S, even for a circuit of a moderate size in Fig. 5.2, is quite bulky to be shown here. In any case, it is difficult to observe the presence of an FRCC just by looking at an analytical expression for a generating function. To demonstrate the presence of an FRCC, we resort to a numerical solution of (5.58), (5.59). We set all but one counting parameters in (5.58) and (5.59) to be zero. The presence of an FRCC can be checked by looking at the solution contours of the equation $S(\chi) - S(-\chi + F) = 0$ plotted as a function, $F(\chi)$. An FRCC occurs for the link k if there exists a solution contour for which F_k is independent of χ_k. In other words, if we plot all pairs, (χ_k, F_k), that satisfy equation, $S(\chi_k) - S(-\chi_k + F_k) = 0$, in plane with axes χ_k and F_k, then if an FRCC holds, the curve must be a horizontal line, which is parallel to the χ_k-axis.

The plot in Fig. 5.4 shows a solution $F_{ij}(\chi_{ij})$, where (i, j) runs through all internal links of the network in Fig. 5.2. It clearly shows that only for the link $(1, 2)$ we have $F_{12} = \text{const}$. For all other links, solution contours are nontrivial functions ($F_{ij}(\chi_{ij}) \neq \text{const}$). The FRCC is upheld by the links that do not belong to any loop. Such a link in our example is the $(1, 2)$ link, and this is the only link that supports FRCC, which is in agreement with our discussion in the main text.

5.5.2 Numerical check for networks coupled to a single reservoir

In this subsection, we numerically analyze the class of networks with loops. Particles can enter and leave only via a single reservoir. Figs. 5.3(a,b) show networks, in which all internal links belong to some loops of a graph. Detailed balance on kinetic rates is not assumed. The twisted master operator for this

case is

$$\begin{aligned}\hat{\mathcal{L}}_{\boldsymbol{\chi}} &= \sum_{jk} g_{jk}\hat{a}_j^\dagger(e^{\chi_{jk}}f_k\hat{a}_k - f_j\hat{a}_j) \\ &- g_n[\hat{a}_n^\dagger(f_n\hat{a}_n - h_n e^{\chi_n}) + h_n - f_n\hat{a}_n e^{-\chi_n}].\end{aligned} \tag{5.60}$$

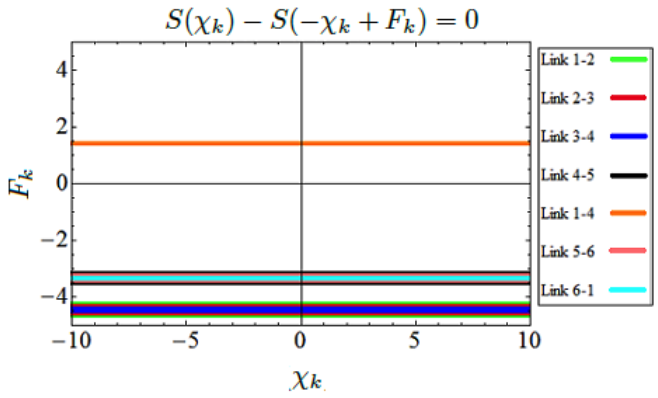

Figure 5.5: Numerical plots for the solution contours of $S(\chi) - S(-\chi + F) = 0$ for all internal links in Fig. 5.3(a). We consider parameters having the following values: $g_{12} = 0.4557$, $g_{21} = 0.6282$, $g_{23} = 0.97782$, $g_{32} = 0.04859$, $g_{34} = 0.9432$, $g_{43} = 0.7787$, $g_{45} = 0.9622$, $g_{54} = 0.4298$, $g_{56} = 0.3023$, $g_{65} = 0.3856$, $g_{61} = 0.4667$, $g_{16} = 0.06163$, $g_{41} = 0.2779$, $g_{14} = 0.09021$, $g_1 = 4.7019$, $h_1 = 8.7658$.

To account for the lack of a detailed balance condition we simply allow $g_{ij} \neq g_{ji}$. In Eq. (5.60) the index "n" corresponds to the only node in the cyclic network that is connected to the reservoir. Similarly to the previous example, we obtain the following cumulant generating function for the case of the networks in Figs. 5.3(a,b),

$$S(\tau, \boldsymbol{\chi}) = g_n\bar{h}_n(e^{\chi_n}\zeta_n - 1), \tag{5.61}$$

where the average occupation number of the node ζ_j can be obtained by solving the following set of linear equations,

$$\sum_j g_{jk}(e^{\chi_{jk}}\zeta_j - \zeta_k) - \delta_{k,n}g_k(\zeta_k - e^{-\chi_k}) = 0. \tag{5.62}$$

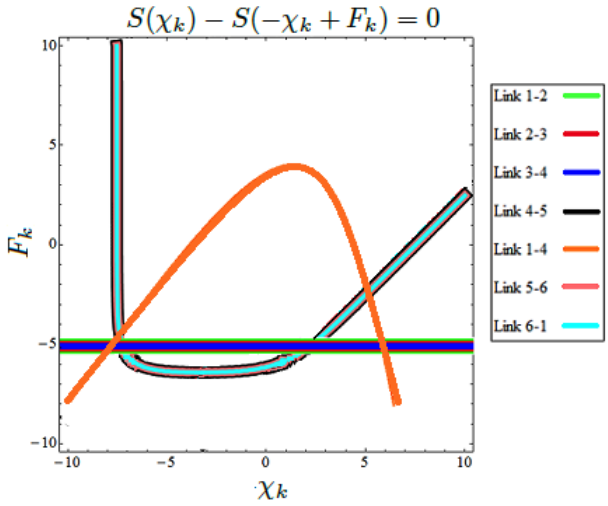

Figure 5.6: Numerical plots for the solution contours of $S(\chi) - S(-\chi + F) = 0$ for all internal links in Fig. 5.3(b). The network parameters for this case are: $g_{12} = 4.5654$, $g_{21} = 7.83$, $g_{23} = 8.6823$, $g_{32} = 0.6629$, $g_{34} = 7.0427$, $g_{43} = 7.4394$, $g_{45} = 7.95$, $g_{54} = 0.1431$, $g_{56} = 0.4052$, $g_{65} = 2.5126$, $g_{61} = 9.5782$, $g_{16} = 0.08372$,$g_{41} = 9.0737$, $g_{14} = 0.81007$, $g_2 = 5.5299$, and $h_2 = 8.2477$.

The numerical check for this case is done by inspecting the solution contours of $S(\chi) - S(-\chi + F) = 0$, as described in previous subsection.

We consider two different cases:

(a) when the reservoir is connected to the central node 1, and

(b) when the reservoir is connected to a non-central node (e.g. the node 2).

We first consider case (a). According to the plot (see Fig. 5.5), all the links have solution contours that are independent of χ. Hence the FRCC holds for all the links when the reservoir is attached to the three link junction 1. The degeneracies in the values of F are due to the charge conservation. Currents through the links $(1, 2)$, $(2, 3)$ and $(3, 4)$ are the same which leads to the same value of F. This degeneracy is also seen for the links $(4, 5)$, $(5, 6)$ and $(6, 1)$. Hence, in Fig. 5.5 we see only three sets of degenerate horizontal lines.

We perform a similar numerical analysis for the case (b) when the reservoir is connected to node 2. The solution contours for $S(\chi) - S(-\chi + F) = 0$ are shown in Fig. 5.6. For this case we obtain degenerate constant lines of $F = \text{const}$ for the links $(1, 2)$, $(2, 3)$ and $(3, 4)$, thereby satisfying an FRCC.

All the other links do not satisfy an FRCC.

5.6 Conclusion

We demonstrated that FRCCs appear in fundamental models of nanoscale electric circuits. Many-body electron interactions, including Coulomb interactions and exclusion interactions, do not break the FRCC prediction in the model of a chaotic cavity coupled to several leads. This robustness can be used to extract information about relative sizes of single particle tunnelling barriers independently of electron interactions. To the best of our knowledge this is a unique example in which measurements of fluctuation relations can provide quantitative information that cannot be easily obtained by measuring lowest current cumulants at given voltages. We also demonstrated that the FRCCs extend to the quantum regime of coherence among electron trajectories. FRCCs can be exacted even when generating functions cannot be derived. This reflects the fact that FRCCs follow from the properties of single particle geometric trajectories that separately show profound symmetries even when the complete stochastic evolution of a system is very complex.

An unusual property of FRCCs is that they are not directly related to the system's dissipation function. This distinguishes them from a vast number of previously found fluctuation relations for currents, entropy, heat and work. Instead, the fact that FRCCs follow from constraints on geometric trajectories relates them to the principle of Geometric Universality of Currents [130] and the class of exact results in non-equilibrium physics called "no-pumping theorems" [130, 139–143]. On the other hand, the similarity between FRCCs and standard fluctuation relations suggests that there can be a more fundamental theory in the background of both fluctuation and no-pumping relations.

Our results should stimulate further theoretical and experimental studies of fluctuation relations, including the search for unifying fundamental principles in non-equilibrium statistical mechanics and new measurement techniques that are enabled by FRCCs.

Recently, we have learned of another work that obtained a large class of FRCCs [144] that do not directly relate to the dissipation functional of the total

system. Unlike our results, their FRCCs apply to a closed network topology without external particle reservoirs.

Chapter 6

Additional Project II: Electrostatic interaction between a water molecule and an ideal metal surface

6.1 Introduction

In this work we study the role of the electrostatic interaction between a single water molecule and an ideal metal surface. Our aim is to understand how the water molecule orients itself under the constraint of the electrostatic interaction energy due to an infinite metal surface [145]. We calculate the electrostatic interaction energy of the water molecule on top of an infinite metal surface. We employ method of images of point charges [146] to calculate the electrostatic interaction energy as a function of different orientations of the molecule. For a set of three charges we use a round up number, based on the water molecule Mulliken atomic charges obtained with siesta (O=-1C,H=0.5C,H=0.5C). We define the initial position of the molecule to lie in the Y-Z plane with Hydrogen atoms facing up away from the image plane. We define $\theta = 0$ for the initial position see Fig. 6.1, this would be the so called vertical configuration in this main chapter. $\theta = \pi/2$ is the horizontal position of the water molecule parallel

to the metal surface. We rotate the water molecule about the Y-axis fixed at the center of charge of the water molecule. The center of charge coordinate $\vec{X_{CC}}$ is defined as $\vec{X}_{CC} = \sum q_i \vec{x}_{q_i} / \sum q_i$. The center of charge corresponds to the center of the point dipole obtained from any given charge distribution. This can be easily realized by the action of a rotation matrix about Y-axis followed by translation along Z-axis. We fix the center of charge to be at a height z above the metal surface.

$$\begin{pmatrix} x_o \\ y_o \\ z_o \end{pmatrix} = \begin{pmatrix} -\frac{r}{2}\cos\frac{\alpha}{2}\sin\theta \\ 0 \\ z - \frac{r}{2}\cos\frac{\alpha}{2}\cos\theta \end{pmatrix} \tag{6.1}$$

We can similarly obtain the most general coordinates of the hydrogen atoms

$$\begin{pmatrix} x_{h1} \\ y_{h1} \\ z_{h1} \end{pmatrix} = \begin{pmatrix} \frac{r}{2}\cos\frac{\alpha}{2}\sin\theta \\ r\sin\frac{\alpha}{2} \\ z + \frac{r}{2}\cos\frac{\alpha}{2}\cos\theta \end{pmatrix} \tag{6.2}$$

$$\begin{pmatrix} x_{h2} \\ y_{h2} \\ z_{h2} \end{pmatrix} = \begin{pmatrix} \frac{r}{2}\cos\frac{\alpha}{2}\sin\theta \\ -r\sin\frac{\alpha}{2} \\ z + \frac{r}{2}\cos\frac{\alpha}{2}\cos\theta \end{pmatrix} \tag{6.3}$$

The coordinates of the image of charges can be easily obtained by a reflection of the z coordinate through the x-y plane.

$$\begin{aligned} (xi_o, yi_o, zi_o) &= (-\frac{r}{2}\cos\frac{\alpha}{2}\sin\theta,\ 0\ ,-\ z + \frac{r}{2}\cos\frac{\alpha}{2}\cos\theta) \\ (xi_{h1}, yi_{h1}, zi_{h1}) &= (\frac{r}{2}\cos\frac{\alpha}{2}\sin\theta,\ r\sin\frac{\alpha}{2}\ ,-z - \frac{r}{2}\cos\frac{\alpha}{2}\cos\theta) \\ (xi_{h2}, yi_{h2}, zi_{h2}) &= (\frac{r}{2}\cos\frac{\alpha}{2}\sin\theta,\ -r\sin\frac{\alpha}{2}\ ,-z - \frac{r}{2}\cos\frac{\alpha}{2}\cos\theta) \end{aligned}$$

In the coordinates described in Fig. 6.1, α is the angle between the two arms of the water molecule and is a known constant ($\alpha = 105^o$). θ is the angle made by the plane containing the water molecule with the vertical. "z" is the distance between the metal surface and the center of charge of the water molecule. The X-Y plane is the reflecting metal surface about which we perform method of images.

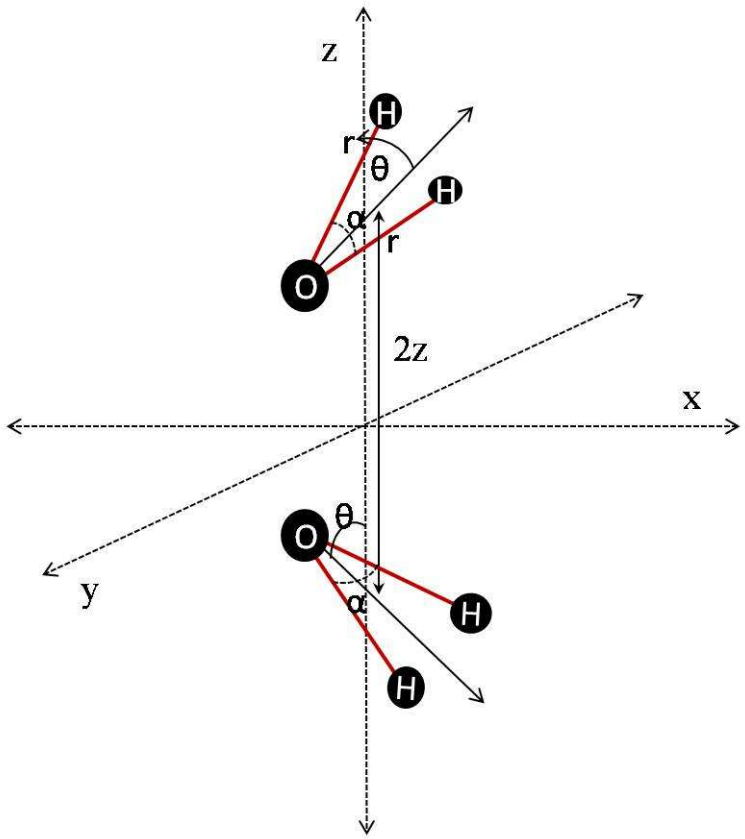

Figure 6.1: Schematics showing the water molecule and its image where the rotation of the molecule is described about center of charge. The molecule is rotated about the Y-axis fixed across its center of charge. θ is the angle of rotation as a function of which we calculate the total electrostatic energy of the system.

The total electrostatic energy of the system (metal +monomer) can be written as

$$U_{electrostatic} = U_{rr} + U_{ir} \tag{6.4}$$

where U_{rr} is the interaction energy of the real charges and U_{ir} is the interaction

energy of the real and image charges.

$$U_{rr} = \frac{1}{4\pi\epsilon_0}\sum_{i=1}^{3}\sum_{j\neq i=1}^{3}\frac{q_i q_j}{\sqrt{(x_i-x_j)^2+(y_i-y_j)^2+(z_i-z_j)^2}}$$

$$U_{ir}(\theta) = \frac{1}{4\pi\epsilon_0}\sum_{i=1}^{3}\sum_{j=1}^{3}\frac{q_i q_j^{image}}{\sqrt{(x_i-xi_j)^2+(y_i-yi_j)^2+(z_i-zi_j)^2}}$$

U_{rr} is the electrostatic self-energy of the molecule and is independent of the orientation of the molecule so the equilibrium configuration only depends on the interaction of the water molecule with its image. To obtain the most favorable configuration of the water molecule due to electrostatic interactions, we minimize $U_{ir}(\theta)$ with respect to the orientation angle θ. We plot the electrostatic potential energy landscape of $U_{ir}(\theta)$ for four distances z from the metal surface as a function of θ. On the basis of the total electrostatic interaction

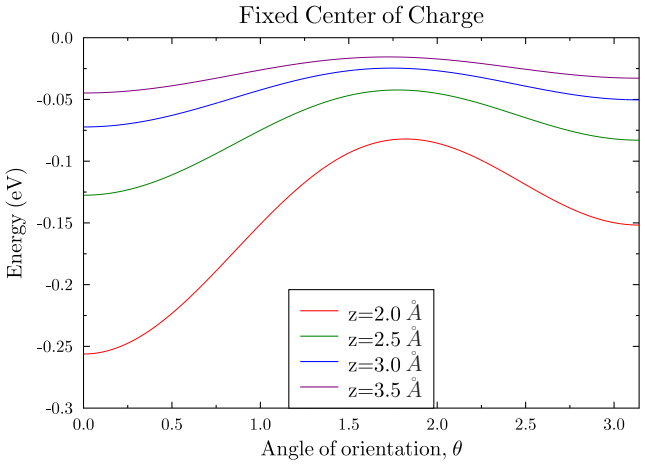

Figure 6.2: $U_{ir}(\theta)$ vs θ for four distances from the metal surface. For all the distances we see that the vertical configurations are more stable than the parallel configuration.

energy landscape for the water molecule as a function of orientation angle θ, we make the following observations.

- The absolute minimum energy configuration of the water molecule is when $\theta = 0$ with respect to the the vertical, when the molecule about

the center of charge and $\theta = \pi$ when the molecule is rotated about a fixed oxygen atom (for smaller distances) .

- $\theta = 0$ or the vertical configuration with Hydrogen atoms pointing up is more favored than the $\theta = \frac{\pi}{2}$ parallel configuration in both the cases.
- We see a clear asymmetry in the $\theta = 0$ and the $\theta = \pi$ configurations for distances $z = 2 - 2.5$Å which will not be seen if an extended dipole approximation of the water molecule is used to model the system.
- With increasing distance from the metal surface, the water molecule can be approximated as a point dipole for which all the orientations will have almost same energy value.

6.1.1 Validity of the dipole approximation.

Based on the above observations we emphasize the fact that a permanent dipole approximation does not distinguish between the cases where the hydrogen atoms point up or down. This picture yields the same energy for both the configurations due to the symmetry in the dipole. On the other hand, accounting for the full charge density distribution of the water molecule clearly distinguishes between the configuration where hydrogen atoms are pointing up or pointing down. Also the permanent dipole approximation of the water molecule is only valid for the case when the water molecule is sufficiently far away from the metal surface in comparison to the O-H bond length. The distance at which the water molecules are adsorbed on the metal surface is roughly 2.5Å, which is not much greater than the water molecule bond lengths (of the order of 1Å). The more realistic approach is to do a full electrostatic interactions of the water molecule .

6.1.2 Electrostatic energy for the full charge density of the water molecule.

Motivated by our previous calculations it will be worth calculating the metal-water molecule interaction energy using the full charge density function of the

water molecule. Our electronic charge distribution is obtained using the Kohn-Sham eigenstates of an isolated water molecule obtained from a previous DFT calculation using the SIESTA [147] code. These Kohn-Sham wave functions are linear combinations of atomic orbitals, we used a single-ζ polarized basis set. We obtain the linear combination coefficients from a self-consistent DFT calculation and use them to compute the Kohn-Sham wave functions of the water molecule and with them the analytical charge density distribution function. The charge density distribution depends the orientation angle θ. For the core and the nuclear charge we use highly localized Gaussian functions centered at the coordinate position of the atoms. These coordinates are defined in the same way as for the point charges which allow for the θ rotation about the Y-axis. We define the charge density in the following way

$$\rho(\overrightarrow{r}, R_i(z,\theta)) = q \left| \sum_{i\ \epsilon\ atom} \sum_{n=1}^{4} C_{nlm} Y_{lm}(\widehat{\overrightarrow{r} - R_i}) R(|\overrightarrow{r} - \overrightarrow{R_i}|) \right|^2 \tag{6.5}$$

Y_{lm} are the spherical harmonics and $R(|\overrightarrow{r} - \overrightarrow{R_i}|)$ is the radial function, which in our case is a set of truncated Gaussian functions we fitted to match the original, confined, SIESTA radial functions. The vector $\overrightarrow{R_i}$ gives the most general position for each atom as given in the equation 6.1, 6.2, and 6.3. q is the total charge in each eigenstate of the basis. C_{nlm} is the linear combination coefficients obtained from the SIESTA calculation. We can also write the core charge distribution using a localized Gaussian function

$$\rho_{core}(\overrightarrow{r}, R_i(z,\theta)) = \sum_{i\ \epsilon\ atom} q_i\ \mid e^{-\kappa(|\overrightarrow{r} - \overrightarrow{R_i}|^2)} \mid^2 \tag{6.6}$$

where $\kappa = \frac{1}{R_c^2}$. R_c is the radius of the core ($R_c = 0.61\mathring{A}$ for oxygen and $R_c = 0.21\mathring{A}$ for hydrogen). Since we have chosen localized atomic orbitals as the basis set for the full wave function, we can rigid-rotate the full charge distribution by rotating the water molecule as described for the point charge case. The atomic orbitals rotate with its atomic center. Hence we can calculate the electrostatic energy between the full charge distribution of the water molecule and the full image charge distribution as a function of orientation angle θ and z (distance of the center of charge from the image plane). We define the full

charge distribution of the water molecule and its image in the following way

$$\rho_{total}(\overrightarrow{r}, R_i(z,\theta)) = \rho_{core}(\overrightarrow{r}, R_i(z,\theta)) + \rho(\overrightarrow{r}, R_i(z,\theta)) \quad (6.7)$$

$$\rho_{image}(\overrightarrow{r}, R_i(z,\theta)) = \rho_{total}(\overrightarrow{r}, R_i(-z,\pi-\theta)) \quad (6.8)$$

Once we establish a charge distribution as a function of atomic positions we can easily rotate the water molecule about the Y-axis fixed at the center of charge and calculate the electrostatic interaction energy [146] with the image charge distribution as a function of orientation angle θ.

$$U_{ir}(z,\theta) = \frac{-1}{8\pi\epsilon_0} \iint \frac{\rho_{total}(\overrightarrow{r}, R_i(z,\theta))\rho_{image}(\overrightarrow{r}, R_i(z,\theta))}{\mid \overrightarrow{r} - \overrightarrow{r'} \mid} \overrightarrow{dr}\ \overrightarrow{dr'} \quad (6.9)$$

We plot the electrostatic energy for the full charge distribution and its image as a function of θ (see Fig. 6.3) for $z = 3.12\mathring{A}$. We compare it to the plot for the three point charge model. According to the plot we observe that $\theta = 0$ (vertical) is the most stable configuration. We also observe that the electrostatic energy for the full charge distribution increases compared to the three-point charge model. It is very interesting to notice how the energy dependence of the full charge distribution is much more complex than a simple dipole or the three point charges model. In particular, we can see that there is an inflection point at $\theta = \frac{\pi}{4}$, which coincides with the angular direction of the O lone pairs. In conclusion, we were able to calculate the electrostatic energy between the water molecule with metal for three point charge model, and full charge distribution calculated from SIESTA. We were able to identify vertical alignment (with hydrogen atoms facing up) as the most stable configuration of the water molecule under the constraint of electrostatic interactions with the metal surface. we also have shown that the full charge distribution provides a much more complex interaction energy landscape, where the lone pairs of the oxygen contribute to minimize the interaction energy for an intermediate alignment.

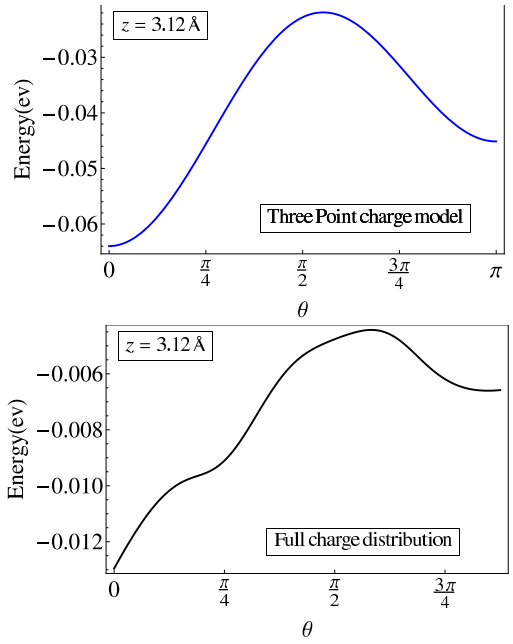

Figure 6.3: $U_{ir}(\theta)$ vs θ for $3.12\mathring{A}$ from the metal surface (Top) For three point charge model. (Bottom) For full charge distribution of water molecule.

Bibliography

[1] M. Kulkarni, S. Ganeshan, and Adam C. Durst. *Phys. Rev. B*, 84:064502, 2011.

[2] M. Ceriotti and M. Parrinello. *Proc. Comp. Sci.*, 1:1601, 2010.

[3] Shuichi Nosé. A unified formulation of the constant temperature molecular dynamics methods. *The Journal of Chemical Physics*, 81(1):511–519, 1984.

[4] Glenn J. Martyna, Michael L. Klein, and Mark Tuckerman. Nose–hoover chains: The canonical ensemble via continuous dynamics. *The Journal of Chemical Physics*, 97(4):2635–2643, 1992.

[5] Scott Habershon, Thomas E. Markland, and David E. Manolopoulos. Competing quantum effects in the dynamics of a flexible water model. *The Journal of Chemical Physics*, 131(2):024501, 2009.

[6] J. R. Kirtley. *Nature*, 373:225, 1995.

[7] Y. Zhang, N.P. Ong, P. W. Anderson, D. A. Bonn, R. X. Liang, and W. N. Hardy. *Phys. Rev. Lett.*, 86:890, 2001.

[8] K. Krishana, J. M. Harris, and N. P. Ong. *Phys. Rev. Lett.*, 75:3529, 1995.

[9] Eun-Ah Kim and Eduardo Fradkin. Double point contact in quantum hall line junctions. *Phys. Rev. Lett.*, 91:156801, Oct 2003.

[10] A M Polyakov. *Gauge Fields and Strings*, volume 455. CRC, 1987.

[11] L. Levitov and G. B. Lesovik. *JETP Lett.*, 58:230, 1993.

[12] Y. Utsumi, D. S. Golubev, M. Marthaler, K. Saito, T. Fujisawa, and Gerd Schön. Bidirectional single-electron counting and the fluctuation theorem. *Phys. Rev. B*, 81:125331, Mar 2010.

[13] Sriram Ganeshan and N. A. Sinitsyn. Fluctuation relations for current components in mesoscopic electric circuits. *Phys. Rev. B*, 84:245405, Dec 2011.

[14] Adrien Poissier, Sriram Ganeshan, and M. V. Fernandez-Serra. The role of hydrogen bonding in water-metal interactions. *Phys. Chem. Chem. Phys.*, 13:3375–3384, 2011.

[15] R. Ramírez and C. P. Herrero. Quantum path integral simulation of isotope effects in the melting temperature of ice ih. *The Journal of Chemical Physics*, 133(14):144511, 2010.

[16] Joseph A. Morrone and Roberto Car. Nuclear quantum effects in water. *Phys. Rev. Lett.*, 101:017801, Jul 2008.

[17] Carlos P. Herrero and Rafael Ramírez. Isotope effects in ice ih: A path-integral simulation. *The Journal of Chemical Physics*, 134(9):094510, 2011.

[18] B. Pamuk, J. M. Soler, R. Ramírez, C. P. Herrero, P. W. Stephens, P. B. Allen, and M.-V. Fernández-Serra. Anomalous nuclear quantum effects in ice. *Phys. Rev. Lett.*, 108:193003, May 2012.

[19] Lin Lin, Joseph A. Morrone, Roberto Car, and Michele Parrinello. Displaced path integral formulation for the momentum distribution of quantum particles. *Phys. Rev. Lett.*, 105:110602, Sep 2010.

[20] M. V. Fernández-Serra and Emilio Artacho. Electrons and hydrogen-bond connectivity in liquid water. *Phys. Rev. Lett.*, 96:016404, Jan 2006.

[21] Eugen Libowitzky. Correlation of o-h stretching frequencies and o-h o hydrogen bond lengths in minerals. *Monatshefte fr Chemie / Chemical Monthly*, 130:1047–1059, 1999.

[22] M. Ceriotti, G. Bussi, and M. Parrinello. *Phys. Rev. Lett.*, 102:020601, 2009.

[23] M. Ceriotti, G. Bussi, and M. Parrinello. *Phys. Rev. Lett.*, 103:030603, 2009.

[24] M. Ceriotti, G. Bussi, and M. Parrinello. *J. Chem. Theory Comput.*, 6:1170, 2010.

[25] M. Ceriotti, M. Parrinello, T. E. Markland, and D. E. Manolopoulos. *J. Chem. Phys*, 133:124104, 2010.

[26] J. A. Morrone, T. E. Markland, M. Ceriotti, and B. J. Berne. *J. Chem. Phys*, 134:084104, 2011.

[27] Rajamani Raghunathan, P. Alex Greaney, and Jeffrey C. Grossman. Phonostat: Thermostatting phonons in molecular dynamics simulations. *The Journal of Chemical Physics*, 134(21):214117, 2011.

[28] G. W. Ford, M. Kac, and P. Mazur. Statistical mechanics of assemblies of coupled oscillators. *Journal of Mathematical Physics*, 6(4):504–515, 1965.

[29] Robert Zwanzig. Nonlinear generalized langevin equations. *Journal of Statistical Physics*, 9:215–220, 1973. 10.1007/BF01008729.

[30] Giovanni Bussi and Michele Parrinello. Accurate sampling using langevin dynamics. *Phys. Rev. E*, 75:056707, May 2007.

[31] M. Tuckerman, B. J. Berne, and G. J. Martyna. Reversible multiple time scale molecular dynamics. *The Journal of Chemical Physics*, 97(3):1990–2001, 1992.

[32] M. V. Fernandez-Serra R. Ramírez, N. Neuerburg and C. Herrero. Quasi-harmonic approximation of thermodynamic properties of ice ih, ii and iii. *The Journal of Chemical Physics, in press*, 137(5), 2012.

[33] Scott Habershon, George S. Fanourgakis, and David E. Manolopoulos. Comparison of path integral molecular dynamics methods for the infrared absorption spectrum of liquid water. *The Journal of Chemical Physics*, 129(7):074501, 2008.

[34] Scott Habershon and David E. Manolopoulos. Zero point energy leakage in condensed phase dynamics: An assessment of quantum simulation methods for liquid water. *The Journal of Chemical Physics*, 131(24):244518, 2009.

[35] P. A. Lee. *Phys. Rev. Lett*, 71:1887, 1993.

[36] M. J. Graf, S-K. Yip, J. A. Sauls, and D. Rainer. *Phys. Rev. B*, 53:15147, 1996.

[37] A. C. Durst and P. A. Lee. *Phys. Rev. B*, 62:1270, 2000.

[38] G. E. Volovik. *JETP Lett.*, 58:469, 1993.

[39] N. B. Kopnin and G. E. Volovik. *JETP Lett.*, 64:690, 1996.

[40] G. E. Volovik. *JETP Lett.*, 65:491, 1997.

[41] M. Franz. *Phys. Rev. Lett*, 82:1760, 1999.

[42] I. Vekhter and A. Houghton. *Phys. Rev. Lett*, 83:4626, 1999.

[43] A. Vishwanath. *Phys. Rev. Lett*, 87:217004, 2001.

[44] O. Vafek, A. Melikyan, and Z. Tesanovic. *Phys. Rev. B*, 64:224508, 2001.

[45] J. Ye. *Phys. Rev. Lett.*, 86:316, 2001.

[46] Adam C. Durst, Ashvin Vishwanath, and Patrick A. Lee. *Phys. Rev. Lett*, 90:187002, 2003.

[47] A. S. Mel'nikov. *Phys. Rev. Lett*, 86:18, 2000.

[48] Jinwu Ye. *Phys. Rev. Lett*, 86:2, 2001.

[49] A. S. Mel'nikov. *J. Phys.: Condens. Matter*, 11:4219, 1999.

[50] M. Franz and Z. Tesanovic. *Phys. Rev. Lett*, 84:554, 2000.

[51] Y. Morita, M. Kohmoto, and K. Maki. *Europhys. lett.*, 40:207, 1997.

[52] Yu. S. Barash. *Phys. Rev. Lett*, 100:1770, 2008.

[53] Vladimir Juricic, Igor F. Herbut, and Zlatko Tesanovic. *Phys. Rev. Lett*, 100:1870, 2008.

[54] A. Melikyan and Z. Tesanovic. *Phys. Rev. B.*, 76:94509, 2007.

[55] Victor M. Villalba. *J.Math Phys.*, 31:11, 1990.

[56] Alan H. Cook. *Proceedings of the Royal Society of London. Series A, Mathematical and Physical Sciences*, 383(1785):247–228, 1982.

[57] Victor M. Villalba. *J. Phys. A: Math. Gen*, 24:3781, 1991.

[58] K. M. Urwin and F. M. Arscott. *Proc. Roy. Soc. Edinburgh*, Sect. A 69:28–44, 1970-71.

[59] F. M. Arscott. The whittakerhill equation and the wave equation in paraboloidal coordinates. *Proc. R. Soc. Edinb.*, A 67:265, 1967.

[60] F. M. Arscott. *Periodic Differential Equations.* (Oxford: Pergamon), 1964.

[61] Bartolomeu D B Figueiredo. *J. Math. Phys. A*, 35:2877, 2002.

[62] Bartolomeu D B Figueiredo. *J. Math. Phys.*, 46:113503, 2005.

[63] Bartolomeu D B Figueiredo. *J. Math. Phys.*, 48:013503, 2007.

[64] E. W. Leaver. Solutions to a generalized spheroidal wave equation: Teukolsky equations in general relativity, and the two-center problem in molecular quantum mechanics. *J. Phys. A*, 27:1238, 1986.

[65] E. L. Ince. *Proceedings of London Mathematical Society*, 23:56–74, 1923.

[66] A. Ronveaux. *Heuns Differential Equations*. Oxford: Oxford University Press, 1995.

[67] Adam C. Durst. *PHD thesis (MIT)*, 2002.

[68] S. H. Simon and P. A. Lee. *Phys. Rev. Lett.*, 78:1548, 1997.

[69] O. Vafek, A. Melikyan, M. Franz, and Z. Tesanovic. *Phys. Rev. B.*, 63:134509, 2001.

[70] P. G. de Gennes. *Superconductivity of Metals and Alloys*. Perseus Books, 1966.

[71] L. P. Gor'kov and J. R. Schrieffer. *Phys. Rev. Lett.*, 80:3360, 1998.

[72] N. B. Kopnin and V. M. Vinokur. *Phys. Rev. B.*, 62:9770, 2000.

[73] Nikolai B. Kopnin. *Theory of Nonequilibrium superconductivity*. Oxford University Press, 2001.

[74] Y. Aharonov and D. Bohm. *Phys. Rev.*, 115:485, 1959.

[75] S. Olariu and I. Popescu. *Rev. Mod. Phys.*, 57:339, 1985.

[76] D. Stelitano. *Phys. Rev. D*, 51:5876, 1995.

[77] N. W. McLachlan. *Theory and application of Mathieu functions*. New York: Dover, 1962.

[78] Gradshteyn and Ryzhik. *Table of Integrals, Series, and Products*. Alan Jeffrey and Daniel Zwillinger (eds.), 2000.

[79] T. Ando, Nakanishi Takeshi, and Saito Riichiro. Berry's phase and absence of back scattering in carbon nanotube. *Journal of the Physical Society of Japan*, 67, Issue 8:2857, 1998.

[80] Samuel Bieri and J. Frohlich. Physical principles underlying the quantum hall effect. *Comptes Rendus Physique*, 12(4):332 – 346, 2011. Quantum Hall Effect and Metrology.

[81] S. Deser, R. Jackiw, and S. Templeton. Topologically massive gauge theories. *Ann. Phys.*, 140:372, 1982.

[82] X. G. Wen. Chiral luttinger liquid and the edge excitations in the fractional quantum hall states. *Phys. Rev. B*, 41:12838–12844, Jun 1990.

[83] J.Frohlich and T. Kerler. Universality in quantum hall systems. *Nuclear Physics B*, 354(23):369 – 417, 1991.

[84] A. M. Chang. Chiral luttinger liquids at the fractional quantum hall edge. *Rev. Mod. Phys.*, 75:1449–1505, Nov 2003.

[85] P. Fendley, A. W. W. Ludwig, and H. Saleur. Exact conductance through point contacts in the $\nu = 1/3$ fractional quantum hall effect. *Phys. Rev. Lett.*, 74:3005–3008, Apr 1995.

[86] C. de C. Chamon, D. E. Freed, and Xiao-Gang Wen. *Phys. Rev. B*, 53:4033, 1996.

[87] C. de C. Chamon, D. E. Freed, and X. G. Wen. Tunneling and quantum noise in one-dimensional luttinger liquids. *Phys. Rev. B*, 51:2363–2379, Jan 1995.

[88] C. de C. Chamon, D. E. Freed, S. A. Kivelson, S. L. Sondhi, and X. G. Wen. Two point-contact interferometer for quantum hall systems. *Phys. Rev. B*, 55:2331–2343, Jan 1997.

[89] A. V. Shytov, L. S. Levitov, and B. I. Halperin. Tunneling into the edge of a compressible quantum hall state. *Phys. Rev. Lett.*, 80:141–144, Jan 1998.

[90] L. S. Levitov, A. V. Shytov, and B. I. Halperin. Effective action of a compressible quantum hall state edge: Application to tunneling. *Phys. Rev. B*, 64:075322, Jul 2001.

[91] Ana Lopez and Eduardo Fradkin. Universal structure of the edge states of the fractional quantum hall states. *Phys. Rev. B*, 59:15323–15331, Jun 1999.

[92] V. Ponomarenko and D. Averin. Two-terminal conductance of a fractional quantum hall edge. *JETP Letters*, 74:87–90, 2001. 10.1134/1.1405891.

[93] V. V. Ponomarenko and D. V. Averin. Splitting electrons into quasiparticles with a fractional edge-state mach-zehnder interferometer. *Phys. Rev. B*, 79:045303, Jan 2009.

[94] V. V. Ponomarenko and D. V. Averin. Antidot tunneling between quantum hall liquids with different filling factors. *Phys. Rev. B*, 71:241308, Jun 2005.

[95] Vadim V. Ponomarenko and Dmitri V. Averin. Mach-zehnder interferometer in the fractional quantum hall regime. *Phys. Rev. Lett.*, 99:066803, Aug 2007.

[96] V. V. Ponomarenko and D. V. Averin. Quantum coherent equilibration in multipoint electron tunneling into a fractional quantum hall edge. *Phys. Rev. B*, 67:035314, Jan 2003.

[97] V. V. Ponomarenko and D. V. Averin. Charge transfer statistics in symmetric fractional edge-state mach-zehnder interferometer. *Phys. Rev. B*, 80:201313, Nov 2009.

[98] Vadim V. Ponomarenko and Dmitri V. Averin. Braiding of anyonic quasiparticles in charge transfer statistics of a symmetric fractional edge-state mach-zehnder interferometer. *Phys. Rev. B*, 82:205411, Nov 2010.

[99] K. T. Law, D. E. Feldman, and Yuval Gefen. Electronic mach-zehnder interferometer as a tool to probe fractional statistics. *Phys. Rev. B*, 74:045319, Jul 2006.

[100] Ivan P. Levkivskyi, Alexey Boyarsky, Jürg Fröhlich, and Eugene V. Sukhorukov. Mach-zehnder interferometry of fractional quantum hall edge states. *Phys. Rev. B*, 80:045319, Jul 2009.

[101] D. L. Kovrizhin and J. T. Chalker. Exactly solved model for an electronic mach-zehnder interferometer. *Phys. Rev. B*, 80:161306, Oct 2009.

[102] D. L. Kovrizhin and J. T. Chalker. Multiparticle interference in electronic mach-zehnder interferometers. *Phys. Rev. B*, 81:155318, Apr 2010.

[103] C. L. Kane and Matthew P. A. Fisher. Impurity scattering and transport of fractional quantum hall edge states. *Phys. Rev. B*, 51:13449–13466, May 1995.

[104] Here we talk about the anomaly cancellation, definition of Φ_j etc. a_σ ($\partial_t a_\sigma = E_\sigma$) is the gauge potential that acts along the edge σ. The second term in Eq. (4.35) comes from the anomaly cancellation of bulk Chern-Simons.

[105] V. V. Ponomarenko and D. V. Averin. Strong-coupling branching between edges of fractional quantum hall liquids. *Phys. Rev. B*, 70:195316, Nov 2004.

[106] A. O. Caldeira and A. J. Leggett. Influence of dissipation on quantum tunneling in macroscopic systems. *Phys. Rev. Lett.*, 46:211–214, Jan 1981.

[107] J. Rammer and H. Smith. Quantum field-theoretical methods in transport theory of metals. *Rev. Mod. Phys.*, 58:323–359, Apr 1986.

[108] G.N. Bochkov and Yu.E. Kuzovlev. Nonlinear fluctuation-dissipation relations and stochastic models in nonequilibrium thermodynamics: I. generalized fluctuation-dissipation theorem. *Physica A: Statistical Mechanics and its Applications*, 106(3):443 – 479, 1981.

[109] Denis J. Evans, E. G. D. Cohen, and G. P. Morriss. Probability of second law violations in shearing steady states. *Phys. Rev. Lett.*, 71:2401–2404, Oct 1993.

[110] C. Jarzynski. Nonequilibrium equality for free energy differences. *Phys. Rev. Lett.*, 78:2690–2693, Apr 1997.

[111] Massimiliano Esposito, Upendra Harbola, and Shaul Mukamel. Nonequilibrium fluctuations, fluctuation theorems, and counting statistics in quantum systems. *Rev. Mod. Phys.*, 81:1665–1702, Dec 2009.

[112] Peter Hänggi and Fabio Marchesoni. Artificial brownian motors: Controlling transport on the nanoscale. *Rev. Mod. Phys.*, 81:387–442, Mar 2009.

[113] David Andrieux and Pierre Gaspard. Fluctuation theorem for currents and schnakenberg network theory. *Journal of Statistical Physics*, 127:107–131, 2007. 10.1007/s10955-006-9233-5.

[114] H. Förster and M. Büttiker. Fluctuation relations without microreversibility in nonlinear transport. *Phys. Rev. Lett.*, 101:136805, Sep 2008.

[115] David Andrieux and Pierre Gaspard. Stochastic approach and fluctuation theorem for ion transport. *Journal of Statistical Mechanics: Theory and Experiment*, 2009(02):P02057, 2009.

[116] Nikolai A. Sinitsyn, Alexei Akimov, and Vladimir Y. Chernyak. Supersymmetry and fluctuation relations for currents in closed networks. *Phys. Rev. E*, 83:021107, Feb 2011.

[117] Jie Ren, V Y Chernyak, and N A Sinitsyn. Duality and fluctuation relations for statistics of currents on cyclic graphs. *Journal of Statistical Mechanics: Theory and Experiment*, 2011(05):P05011, 2011.

[118] Rafael Sánchez, Rosa López, David Sánchez, and Markus Büttiker. Mesoscopic coulomb drag, broken detailed balance, and fluctuation relations. *Phys. Rev. Lett.*, 104:076801, Feb 2010.

[119] A Rkos and R J Harris. On the range of validity of the fluctuation theorem for stochastic markovian dynamics. *Journal of Statistical Mechanics: Theory and Experiment*, 2008(05):P05005, 2008.

[120] Massimiliano Esposito, Upendra Harbola, and Shaul Mukamel. Fluctuation theorem for counting statistics in electron transport through quantum junctions. *Phys. Rev. B*, 75:155316, Apr 2007.

[121] Y. V. Nazarov and Y. M. Blanter. *Quantum Transport*. Cambridge University Press, 2009.

[122] S. Gustavsson, R. Leturcq, B. Simovič, R. Schleser, T. Ihn, P. Studerus, K. Ensslin, D. C. Driscoll, and A. C. Gossard. Counting statistics of single electron transport in a quantum dot. *Phys. Rev. Lett.*, 96:076605, Feb 2006.

[123] Sukhorukov et al. *Nature Phys.*, 3:243, 2007.

[124] Gregory Bulnes Cuetara, Massimiliano Esposito, and Pierre Gaspard. Fluctuation theorems for capacitively coupled electronic currents. *Phys. Rev. B*, 84:165114, Oct 2011.

[125] S. Pilgram, A. N. Jordan, E. V. Sukhorukov, and M. Büttiker. Stochastic path integral formulation of full counting statistics. *Phys. Rev. Lett.*, 90:206801, May 2003.

[126] Alexander Altland, Alessandro De Martino, Reinhold Egger, and Boris Narozhny. Fluctuation relations and rare realizations of transport observables. *Phys. Rev. Lett.*, 105:170601, Oct 2010.

[127] P. W. Brouwer. Rectification of displacement currents in an adiabatic electron pump. *Phys. Rev. B*, 63:121303, Mar 2001.

[128] P.-E. Roche, B. Derrida, and B. Douot. Mesoscopic full counting statistics and exclusion models. *The European Physical Journal B - Condensed Matter and Complex Systems*, 43:529–541, 2005. 10.1140/epjb/e2005-00087-5.

[129] Andrew N. Jordan, Eugene V. Sukhorukov, and Sebastian Pilgram. Fluctuation statistics in networks: A stochastic path integral approach. *Journal of Mathematical Physics*, 45(11):4386–4417, 2004.

[130] V Y Chernyak, M Chertkov, and N A Sinitsyn. The geometric universality of currents. *Journal of Statistical Mechanics: Theory and Experiment*, 2011(09):P09006, 2011.

[131] R. Dean Astumian. Stochastic conformational pumping: A mechanism for free-energy transduction by molecules. *Annual Review of Biophysics*, 40(1):289–313, 2011.

[132] N. Hengartner N. A. Sinitsyn and I. Nemenman. *PNAS*, 106:10546, 2009.

[133] N. A. Sinitsyn and Ilya Nemenman. Universal geometric theory of mesoscopic stochastic pumps and reversible ratchets. *Phys. Rev. Lett.*, 99:220408, Nov 2007.

[134] Jun Ohkubo. Variational principle of counting statistics in master equations. *Phys. Rev. E*, 80:012101, Jul 2009.

[135] Bernard Derrida and Joel L. Lebowitz. Exact large deviation function in the asymmetric exclusion process. *Phys. Rev. Lett.*, 80:209–213, Jan 1998.

[136] D. A. Bagrets and Yu. V. Nazarov. Full counting statistics of charge transfer in coulomb blockade systems. *Phys. Rev. B*, 67:085316, Feb 2003.

[137] Irina V. Gopich and Attila Szabo. Theory of the statistics of kinetic transitions with application to single-molecule enzyme catalysis. *The Journal of Chemical Physics*, 124(15):154712, 2006.

[138] N. A. Sinitsyn and I. Nemenman. The berry phase and the pump flux in stochastic chemical kinetics. *EPL (Europhysics Letters)*, 77(5):58001, 2007.

[139] D. Astumian. *PNAS*, 104:19715, 2007.

[140] Saar Rahav, Jordan Horowitz, and Christopher Jarzynski. Directed flow in nonadiabatic stochastic pumps. *Phys. Rev. Lett.*, 101:140602, Oct 2008.

[141] Jordan Horowitz and Christopher Jarzynski. Exact formula for currents instrongly pumped diffusive systems. *Journal of Statistical Physics*, 136:917–925, 2009. 10.1007/s10955-009-9818-x.

[142] V. Y. Chernyak and N. A. Sinitsyn. Pumping restriction theorem for stochastic networks. *Phys. Rev. Lett.*, 101:160601, Oct 2008.

[143] Christian Maes, Karel Netočný, and Simi R. Thomas. General no-go condition for stochastic pumping. *The Journal of Chemical Physics*, 132(23):234116, 2010.

[144] Andre Barato, Raphal Chetrite, Haye Hinrichsen, and David Mukamel. A gallavotti-cohen-evans-morriss like symmetry for a class of markov jump processes. *Journal of Statistical Physics*, 146:294–313, 2012. 10.1007/s10955-011-0389-2.

[145] Javier Carrasco, Angelos Michaelides, and Matthias Scheffler. Insight from first principles into the nature of the bonding between water molecules and 4d metal surfaces. *The Journal of Chemical Physics*, 130(18):184707, 2009.

[146] J. D. Jackson. *Classical Electrodynamics*. Willey, 1998.

[147] Jos M Soler, Emilio Artacho, Julian D Gale, Alberto Garca, Javier Junquera, Pablo Ordejn, and Daniel Snchez-Portal. The siesta method for ab initio order- n materials simulation. *Journal of Physics: Condensed Matter*, 14(11):2745, 2002.

[148] Samuel Bieri and Jrg Frhlich. Effective field theory and tunneling currents in the fractional quantum hall effect. *Annals of Physics*, 327(4):959 – 993, 2012.

Appendix A

Appendix for chapter 3

A.1 Separation of Variables for massless spin-1/2 2D Dirac equation in elliptical coordinates

We present here the details of the steps (see Sec. 3.5) leading to the separation of variables in elliptical coordinates of a two-dimensional Dirac equation for massless spin-1/2 fermions. This calculation is in the spirit of work done in Ref. [55]. An alternate method can also be found in Ref. [56]. The 2-D Dirac equation is given by

$$[\gamma^0\partial_t + \gamma^1\partial_x + \gamma^2\partial_y]\psi = 0 \tag{A.1}$$

where the γ's satisfy the following anticommutation relations

$$\{\gamma^\alpha, \gamma^\beta\} = 2g^{\alpha\beta} \tag{A.2}$$

with Minkowski metric given by $g = diag(1, -1, -1)$. In order to rewrite the Dirac equation in curved coordinates, let us introduce the following coordinate transformation

$$x = f(\mu, \nu), \quad y = g(\mu, \nu), \quad t = t. \tag{A.3}$$

The reader should note that the transformations are kept general and the choice of elliptical coordinates will be made when required. The general trans-

formations given by $f(\mu,\nu)$ and $g(\mu,\nu)$ must satisfy the condition that $f+ig$ is holomorphic or complex differentiable in the $u+iv$ plane which leads to the following Cauchy-Riemann equations,

$$f_\mu = g_\nu, \quad g_\mu = -f_\nu \tag{A.4}$$

Using Eq. (A.3) and Eq. (A.4) in Eq. (A.1), one can easily write the dirac equation in curved coordinates as

$$[\gamma^0\partial_t + \frac{\widetilde{\gamma}^1}{h}\partial_\mu + \frac{\widetilde{\gamma}^2}{h}\partial_\nu]\psi = 0 \tag{A.5}$$

where

$$\widetilde{\gamma}^1 = \frac{1}{h}(f_\mu\gamma^1 - f_\nu\gamma^2) \tag{A.6}$$

$$\widetilde{\gamma}^2 = \frac{1}{h}(f_\nu\gamma^1 + f_\mu\gamma^2) \tag{A.7}$$

with the Lame Metric given by $h = \sqrt{f_\mu^2 + g_\mu^2}$. We introduce the following transformation matrices:

$$S = \frac{1}{\sqrt{h}}(e^{\frac{\phi}{2}\gamma^1\gamma^2}), \quad S^{-1} = \sqrt{h}(e^{-\frac{\phi}{2}\gamma^1\gamma^2}) \tag{A.8}$$

with $\phi = \arctan(\frac{g_\mu}{f_\mu})$. We use Eq. (A.8) in transforming the Dirac equation, That is we perform

$$S^{-1}[\gamma^0\partial_t + \frac{\widetilde{\gamma}^1}{h}\partial_\mu + \frac{\widetilde{\gamma}^2}{h}\partial_\nu]SS^{-1}\psi = 0 \tag{A.9}$$

which results in

$$[\partial_t + \frac{\gamma^0\gamma^1}{h}\partial_\mu + \frac{\gamma^0\gamma^2}{h}\partial_\nu]\Phi = 0 \tag{A.10}$$

where the transformed spinor satisfies

$$\Phi = S^{-1}\psi \tag{A.11}$$

To separate the time variable we introduce the following operator definitions.

$$\widehat{k_2} \equiv \partial_t, \quad \widehat{k_1} \equiv (\frac{\gamma^0\gamma^1}{h}\partial_\mu + \frac{\gamma^0\gamma^2}{h}\partial_\nu) \tag{A.12}$$

The Hamiltonian Eq. (A.10) will read

$$[\widehat{k_2} + \widehat{k_1}]\Phi = 0 \tag{A.13}$$

with $\widehat{k_1}$ and $\widehat{k_2}$ satisfying the commutation relation

$$[\widehat{k_2}, \widehat{k_1}] = 0 \tag{A.14}$$

To separate the time variable, we introduce k such that

$$\widehat{k_2}\Phi = -ik\Phi \tag{A.15}$$

which immediately gives

$$\widehat{k_1}\Phi = ik\Phi \tag{A.16}$$

Here, we make the following choice for a two-dimensional representation of the Dirac matrices,

$$\gamma^0 = \tau_2, \quad \gamma^1 = i\tau_1 \quad , \gamma^2 = -i\tau_3 \tag{A.17}$$

In this representation, Eq. (A.16) reads

$$[\tau_3\partial_\mu + \tau_1\partial_\nu - ikh]\Phi = 0 \tag{A.18}$$

The presence of h in Eq. (A.18) forbids us to write Eq. (A.18) as sum of two commuting differential operators. Therefore we will introduce a similarity transformation $T(\mu, \nu)$ acting on the Dirac operator and the spinor.

$$T = e^{\beta}e^{i\alpha\tau_2} \tag{A.19}$$

with

$$\alpha_\mu = -\beta_\nu, \quad \alpha_\nu = \beta_\mu \tag{A.20}$$

To be more explicit, we do the T-transformation on Eq. (A.18) in the following way

$$T[\tau_3\partial_\mu + \tau_1\partial_\nu - ikh]TT^{-1}\Phi = 0 \tag{A.21}$$

which after some algebra gives,

$$[\tau_3\partial_\mu + \tau_1\partial_\nu - ikhe^{i2\alpha\tau_2}]Y = 0 \tag{A.22}$$

with

$$Y = T^{-1}\Phi \tag{A.23}$$

It should be noted that because $\alpha(\mu,\nu)$ in Eq. (A.19) is arbitrary we choose it to be of the following structure,

$$e^{i2\alpha\tau_2} = \frac{[a(\mu) + ib(\nu)\tau_2]}{h} \tag{A.24}$$

This specific form of the transformation matrix T cancels the factor h (Lame metric) in the Dirac equation which mixes the μ and ν variables. It is trivial to check that $a(\mu)^2 + b(\nu)^2 = h^2$ and the structure for $\beta(\mu,\nu)$ can be obtained using Eq. (A.20). At this point we move to elliptical coordinates with Eq. (A.3) taking the form

$$x = f(\mu,\nu) = R\,\cosh\mu\,\cos\nu \tag{A.25}$$

$$y = g(\mu,\nu) = R\,\sinh\mu\,\sin\nu \tag{A.26}$$

From (A.25, A.26) we get

$$h^2 = R^2\sinh^2\mu + R^2\sin^2\nu \tag{A.27}$$

Using above (A.27) along with the fact that $a(\mu)^2 + b(\nu)^2 = h^2$ gives us by comparison the following

$$a(\mu) = R\,\sinh\mu, \quad b(\nu) = R\,\sin\nu \tag{A.28}$$

Now we introduce the following operators

$$\widehat{L_1} = \tau_3 \partial_\mu - ika(\mu) \tag{A.29}$$

$$\widehat{L_2} = \tau_3 \partial_\nu - ikb(\nu) \tag{A.30}$$

$$Y = [\widehat{L_2} + i\tau_2 \widehat{L_1}]Z \tag{A.31}$$

Using Eqs. (A.29), (A.30), and (A.31) we can finally express the Dirac equation Eq. (A.22) as

$$[(\partial_\mu^2 - ik\tau_3 a_\mu + k^2 a^2) + (\partial_\nu^2 - ik\tau_3 b_\nu + k^2 b^2)]Z = 0 \tag{A.32}$$

Defining

$$Z = \begin{pmatrix} \alpha(\mu)A(\nu) \\ \beta(\mu)B(\nu) \end{pmatrix} \tag{A.33}$$

and introducing a separation constant λ gives us four 2nd order ordinary differential equations.

$$(\partial_\mu^2 - ika_\mu + k^2 a^2 - \lambda^2)\alpha(\mu) = 0 \tag{A.34}$$

$$(\partial_\mu^2 + ika_\mu + k^2 a^2 - \lambda^2)\beta(\mu) = 0 \tag{A.35}$$

$$(\partial_\nu^2 - ikb_\nu + k^2 b^2 + \lambda^2)A(\nu) = 0 \tag{A.36}$$

$$(\partial_\nu^2 + ikb_\nu + k^2 b^2 + \lambda^2)B(\nu) = 0 \tag{A.37}$$

After putting back $a = R\sinh\mu$, $a_\mu = R\cosh\mu$, $b = R\sin\nu$, and $b_\nu = R\cos\nu$ we obtain

$$(\partial_\nu^2 - ikR\cos\nu + k^2 R^2 \sin^2\nu + \lambda^2)A(\nu) = 0 \tag{A.38}$$

$$(\partial_\nu^2 + ikR\cos\nu + k^2 R^2 \sin^2\nu + \lambda^2)B(\nu) = 0 \tag{A.39}$$

$$(\partial_\mu^2 - ikR\cosh\mu + k^2 R^2 \sinh^2\mu - \lambda^2)\alpha(\mu) = 0 \tag{A.40}$$

$$(\partial_\mu^2 + ikR\cosh\mu + k^2 R^2 \sinh^2\mu - \lambda^2)\beta(\mu) = 0 \tag{A.41}$$

which are equivalent to 4 coupled first order equations that connect the upper and lower components of the wave function spinor

$$
\begin{aligned}
(\partial_\nu - ikR\sin\nu)A(\nu) &= i\lambda B(\nu) && \text{(A.42)}\\
(\partial_\nu + ikR\sin\nu)B(\nu) &= i\lambda A(\nu) && \text{(A.43)}\\
(\partial_\mu - ikR\sinh\mu)\alpha(\mu) &= \lambda\beta(\mu) && \text{(A.44)}\\
(\partial_\mu + ikR\sinh\mu)\beta(\mu) &= \lambda\alpha(\mu) && \text{(A.45)}
\end{aligned}
$$

Thus we have reduced the 2D massless Dirac equation in elliptical coordinates to a problem of four decoupled ordinary differential equations. These separated radial and angular equations are known as the Whittaker Hill equations (WHE).

The explicit form of the transformation matrices can be evaluated. Using Eq. (A.31) we have

$$
Y = \begin{pmatrix} \alpha(\mu)B(\nu) \\ i\beta(\mu)A(\nu) \end{pmatrix} \qquad \text{(A.46)}
$$

We write below a more transparent and dimensionless form for S (Eq. (A.8)) and T (Eq. (A.19))

$$
\begin{aligned}
S &= \frac{\sqrt{R}}{\sqrt{h}} \begin{pmatrix} \cos\frac{\phi}{2} & -\sin\frac{\phi}{2} \\ \sin\frac{\phi}{2} & \cos\frac{\phi}{2} \end{pmatrix} && \text{(A.47)}\\
T &= e^{\beta} \begin{pmatrix} \cos\alpha & \sin\alpha \\ -\sin\alpha & \cos\alpha \end{pmatrix} && \text{(A.48)}
\end{aligned}
$$

which immediately gives ST as

$$
ST = \sqrt{R}\frac{e^{\beta}}{\sqrt{h}} \begin{pmatrix} \cos(\alpha-\phi/2) & \sin(\alpha-\phi/2) \\ -\sin(\alpha-\phi/2) & \cos(\alpha-\phi/2) \end{pmatrix} \qquad \text{(A.49)}
$$

In elliptical coordinates, α, β, and ϕ take the following form,

$$\alpha = \frac{1}{2}\tan^{-1}(\frac{\sin\,\nu}{\sinh\,\mu}) \tag{A.50}$$

$$\beta = -\frac{1}{2}\tanh^{-1}(\frac{\cos\,\nu}{\cosh\,\mu}) \tag{A.51}$$

$$\phi = \tan^{-1}(\coth\,\mu\,\tan\,\nu) \tag{A.52}$$

$$\tag{A.53}$$

and we can rewrite β using the log formula for $\tanh^{-1}$.

$$\beta = \ln(\frac{\cosh\,\mu+\cos\,\nu}{\cosh\,\mu-\cos\,\nu})^{-1/4} \tag{A.54}$$

$$\frac{e^{\beta}}{\sqrt{h}} = \frac{1}{\sqrt{(\cosh\,\mu+\cos\,\nu)}} \tag{A.55}$$

$$\tag{A.56}$$

After using some trigonometric identities, these expressions for α and ϕ satisfy the following relations

$$\alpha-\frac{\phi}{2} = \frac{\tan^{-1}(\frac{\sin\,\nu}{\sinh\,\mu})-\tan^{-1}(\coth\,\mu\,\tan\,\nu)}{2} \tag{A.57}$$

$$2(\alpha-\frac{\phi}{2}) = \tan^{-1}(\frac{-\sin\,\nu\,\sinh\,\mu}{\cos\,\nu\,\cosh\,\mu+1}) \tag{A.58}$$

To evaluate ST we need to calculate its components in terms of elliptical coordinate variables. Tangent, sine and cosine of the double angle can be evaluated as

$$\tan(2(\alpha-\frac{\phi}{2})) = \frac{-\sin\,\nu\,\sinh\,\mu}{\cos\,\nu\,\cosh\,\mu+1}$$

$$\sin(2(\alpha-\frac{\phi}{2})) = \frac{-\sin\,\nu\,\sinh\,\mu}{\cos\,\nu+\cosh\,\mu}$$

$$\cos(2(\alpha-\frac{\phi}{2})) = \frac{\cos\,\nu\cosh\,\mu+1}{\cos\,\nu+\cosh\,\mu}$$

Using the half angle formulae we can finally evaluate the components of the

transformation matrix in terms of the coordinate variables. While reducing the components to half angle there is arbitrariness in the choice of the sign of the trigonometric functions in each quadrant. We make a choice of signs such that our final transformation matrix is 4π periodic in angular coordinate ν. We could as well make a choice which would result in 2π periodicity of transformation matrix. Any choice can be compensated by choosing the periodicity of the angular solutions accordingly. For example, we choose 4π periodic eigenstates for the angular WHE (see Sec. 3.6).

$$\sin(\alpha - \frac{\phi}{2}) = -\frac{\sin\,\frac{\nu}{2}\,\sinh\,\frac{\mu}{2}}{\sqrt{\cos\,\nu + \cosh\,\mu}} \tag{A.59}$$

$$\cos(\alpha - \frac{\phi}{2}) = \frac{\cos\,\frac{\nu}{2}\cosh\,\frac{\mu}{2}}{\sqrt{\cos\,\nu + \cosh\,\mu}} \tag{A.60}$$

$$\tag{A.61}$$

Using Eqs. (A.49, (A.55), (A.59), and (A.60) along with the fact that $\psi = ST\,Y$, we have

$$\psi = \frac{1}{(\cosh\,\mu + \cos\,\nu)} \begin{pmatrix} \cos\,\frac{\nu}{2}\cosh\,\frac{\mu}{2} & -\sin\,\frac{\nu}{2}\sinh\,\frac{\mu}{2} \\ \sin\,\frac{\nu}{2}\sinh\,\frac{\mu}{2} & \cos\,\frac{\nu}{2}\cosh\,\frac{\mu}{2} \end{pmatrix} \begin{pmatrix} \alpha(\mu)B(\nu) \\ i\beta(\mu)A(\nu) \end{pmatrix}$$

A.2 Asymptotic form for radial solutions

To study the scattering cross section, we have to calculate the phase shifts of the scattered wave function at large radial distances where the detector is placed. Hence, the asymptotic form of the radial solutions is an important piece of information in setting up the scattering cross section. In this section we give the asymptotic form of the first and second radial solutions to WHE. In the Sec. 3.6.2 we expand radial solutions in terms of confluent hypergeometric functions (CHF) (see Eqs. (3.88) and (3.89)). We now write the asymptotic form of these solutions. As $\mu \to \infty$ in the series of CHF, only the leading term

in the sum contributes

$$Jo_m(\mu) \approx e^{ikR\cosh\mu}\ \cosh\frac{\mu}{2}\ M(\frac{1}{2},2,-4ikR\cosh^2\frac{\mu}{2}) \quad \text{(A.62)}$$

$$Je_m(\mu) \approx e^{ikR\cosh\mu}\ \sinh\frac{\mu}{2}\ M(\frac{1}{2},2,-4ikR\cosh^2\frac{\mu}{2}) \quad \text{(A.63)}$$

The asymptotic form of the CHF is well known [78] and is given as

$$M(\frac{1}{2},2,-4ikR\cosh^2\frac{\mu}{2}) \approx \frac{1}{\Gamma(\frac{1}{2})}\sqrt{\frac{1}{4ikR\cosh^2\frac{\mu}{2}}} \quad \text{(A.64)}$$

At large distances, we have $\cosh\mu \sim \sinh\mu \sim e^{\mu} = \frac{2r}{R}$, the elliptic coordinate ν is reduced to the ordinary polar angle ϕ, and therefore the full asymptotic form of the solutions become

$$Jo_m(r) \approx \sqrt{\frac{1}{\pi kR}}e^{i(kr-\frac{\pi}{4})} \quad \text{(A.65)}$$

$$Je_m(r) \approx \sqrt{\frac{1}{\pi kR}}e^{i(kr-\frac{\pi}{4})} \quad \text{(A.66)}$$

From inspection of the large μ behavior of the second solutions we find the asymptotic form to be

$$Fey_m(r) \approx \sqrt{\frac{1}{\pi kR}}e^{i(kr+\frac{\pi}{4})} \quad \text{(A.67)}$$

$$Gey_m(r) \approx \sqrt{\frac{1}{\pi kR}}e^{i(kr+\frac{\pi}{4})} \quad \text{(A.68)}$$

Similarly we can also determine the asymptotic forms for the lower component radial solutions

$$Jo_m^{'}(r) \approx \sqrt{\frac{1}{\pi kR}} e^{-im\pi} e^{-i(kr+\frac{\pi}{4})} \tag{A.69}$$

$$Je_m^{'}(r) \approx \sqrt{\frac{1}{\pi kR}} e^{-im\pi} e^{-i(kr+\frac{\pi}{4})} \tag{A.70}$$

$$Fey_m^{'}(r) \approx \sqrt{\frac{1}{\pi kR}} e^{-im\pi} e^{-i(kr-\frac{\pi}{4})} \tag{A.71}$$

$$Gey_m^{'}(r) \approx \sqrt{\frac{1}{\pi kR}} e^{-im\pi} e^{-i(kr-\frac{\pi}{4})} \tag{A.72}$$

A.3 Plane wave expansion coefficients

In this section we calculate the plane wave expansion coefficients n_m^e and n_m^o appearing in Eq. (3.113).

$$\begin{aligned} e^{i\,\vec{k}\cdot\vec{r}} \begin{pmatrix} \cos\frac{\theta}{2} \\ \sin\frac{\theta}{2} \end{pmatrix} &= (ST)\Bigg\{ \sum_m n_m^e Be_m(\theta) \begin{pmatrix} Je_m Be_m \\ i\,Je_m^{'} Ae_m \end{pmatrix} \\ &+ \sum_m n_m^o Bo_m(\theta) \begin{pmatrix} Jo_m Bo_m \\ i\,Jo_m^{'} Ao_m \end{pmatrix} \Bigg\} \end{aligned} \tag{A.73}$$

In elliptical coordinates a unidirectional plane wave is described in terms of the incident direction θ in the following way,

$$\vec{k} = (\cos\theta\hat{x} + \sin\theta\hat{y}),\ \vec{r} = R(\cosh\mu\cos\nu\ \hat{x} + \sinh\mu\sin\nu\ \hat{y}) \tag{A.74}$$

$$\vec{k}\cdot\vec{r} = kR(\cosh\mu\cos\nu\cos\theta + \sinh\mu\sin\nu\sin\theta) \tag{A.75}$$

Multiplying both sides by the transformation matrix $(ST)^{-1}$,

$$e^{i\,\vec{k}\cdot\vec{r}}(ST)^{-1}\begin{pmatrix}\cos\frac{\theta}{2}\\ \sin\frac{\theta}{2}\end{pmatrix} = \left\{\sum_m n_m^e Be_m(\theta)\begin{pmatrix} Je_m Be_m \\ i\,Je_m^{'}Ae_m\end{pmatrix} + \sum_m n_m^o Bo_m(\theta)\begin{pmatrix} Jo_m Bo_m \\ i\,Jo_m^{'}Ao_m\end{pmatrix}\right\} \tag{A.76}$$

$$e^{i\,\vec{k}\cdot\vec{r}}\begin{pmatrix}\cos\frac{\nu}{2}\cosh\frac{\mu}{2}\cos\frac{\theta}{2}+\sin\frac{\nu}{2}\sinh\frac{\mu}{2}\sin\frac{\theta}{2}\\ \cos\frac{\nu}{2}\cosh\frac{\mu}{2}\sin\frac{\theta}{2}-\sin\frac{\nu}{2}\sinh\frac{\mu}{2}\cos\frac{\theta}{2}\end{pmatrix} = \left\{\sum_m n_m^e Be_m(\theta)\begin{pmatrix} Je_m Be_m \\ i\,Je_m^{'}Ae_m\end{pmatrix} + \sum_m n_m^o Bo_m(\theta)\begin{pmatrix} Jo_m Bo_m \\ i\,Jo_m^{'}Ao_m\end{pmatrix}\right\} \tag{A.77}$$

For brevity of notation, we write

$$\begin{pmatrix}\cos\frac{\nu}{2}\cosh\frac{\mu}{2}\cos\frac{\theta}{2}+\sin\frac{\nu}{2}\sinh\frac{\mu}{2}\sin\frac{\theta}{2}\\ \cos\frac{\nu}{2}\cosh\frac{\mu}{2}\sin\frac{\theta}{2}-\sin\frac{\nu}{2}\sinh\frac{\mu}{2}\cos\frac{\theta}{2}\end{pmatrix} \equiv \begin{pmatrix} f_{up}(\mu,\nu,\theta)\\ f_d(\mu,\nu,\theta)\end{pmatrix} \tag{A.78}$$

We also have the following bi-orthogonal properties for the angular Whittaker Hill functions.

$$\int_0^{2\pi} Ao_s^* Be_m d\nu = k_m\delta_{ms}\ ,\quad \int_0^{2\pi} Ae_s^* Bo_m d\nu = k_m^*\delta_{ms} \tag{A.79}$$

$$\int_0^{2\pi} Ae_s^* Be_m d\nu = 0,\quad \int_0^{2\pi} Ao_s^* Bo_m d\nu = 0 \tag{A.80}$$

where k_m is the normalization constant. Operating on both sides with row vector $\begin{pmatrix} Ao_s^*(\theta)Ao_s^*(\nu), & Ao_s^*(\theta)Bo_s^*(\nu)\end{pmatrix}$, integrating over ν and θ from 0 to 2π, and applying the bi-orthogonality relations, we get

$$\int_0^{2\pi}\int_0^{2\pi} e^{i\,kR(\cosh\mu\cos\nu\cos\theta+\sinh\mu\sin\nu\sin\theta)} Ao_s^*(\theta)(Ao_s^*(\nu)f_{up}(\mu,\nu,\theta) + Bo_s^*(\nu)f_d(\mu,\nu,\theta))d\nu\ d\theta = \Big\{ n_s^e\ k_s^2(Je_s + iJe_s^{'}) \Big\} \tag{A.81}$$

Putting $\mu = \mu_0$ in the above expression yields

$$n_s^e = \Big(\int_0^{2\pi}\int_0^{2\pi} e^{i\,kR(\cosh\mu_0\cos\nu\cos\theta+\sinh\mu_0\sin\nu\sin\theta)} Ao_s^*(\theta)(Ao_s^*(\nu)f_{up}(\mu_0,\nu,\theta) + Bo_s^*(\nu)f_d(\mu_0,\nu,\theta))d\nu\ d\theta \Big) \Big/ k_s^2(Je_s(\mu_0) + iJe_s^{'}(\mu_0)) \tag{A.82}$$

Similarly, we can calculate n_s^o by operating on both sides with row vector $\Big(\ Ae_s^*(\theta)Ae_s^*(\nu),\quad Ae_s^*(\theta)Be_s^*(\nu)\ \Big)$

$$n_s^o = \Big(\int_0^{2\pi}\int_0^{2\pi} e^{i\,kR(\cosh\mu_0\cos\nu\cos\theta+\sinh\mu_0\sin\nu\sin\theta)} Ae_s^*(\theta)(Ae_s^*(\nu)f_{up}(\mu_0,\nu,\theta) + Be_s^*(\nu)f_d(\mu_0,\nu,\theta))d\nu d\theta \Big) \Big/ (k_s^*)^2(Jo_s(\mu_0) + iJo_s^{'}(\mu_0)) \tag{A.83}$$

We have checked that n_s^e and n_s^o are independent of the value of μ_0.

Appendix B

Appendix for chapter 4

B.1 Chiral Bosons Coupled to Gauge Fields from non-Chiral Bosons

In this section we derive a gauge invariant action for chiral bosons coupled to gauge fields. Our starting point is non-chiral bosonic theory in the presence of gauge fields. This exercise is another way to derive chiral bosons coupled to gauge fields and how is coupled to the original non-chiral boson.

$$Z[\tilde{a}_\mu] = \int D\phi e^{i\int dxdt\left[(\frac{1}{v}(\dot{\phi})^2 - v\phi_x^2) + \kappa\epsilon^{\mu\nu}\tilde{a}_\mu\partial_\mu\phi\right]} \tag{B.1}$$

Now we add auxiliary θ fields in the partition function in the following form,

$$Z[\tilde{a}_\mu] = \int D\phi D\theta e^{iS[\phi,\theta,\tilde{a}_\mu]} \tag{B.2}$$

$$\begin{aligned} S &= \int dxdt\big[\dot{\phi}(\theta_x + 2\kappa\tilde{a}_1) - \frac{v}{2}(\theta_x + 2\kappa\tilde{a}_1)^2 \\ &- \frac{v}{2}\phi_x^2 + 2\kappa(\tilde{a}_0\phi_x - \tilde{a}_1\dot{\phi})\big] \end{aligned} \tag{B.3}$$

In the above action we make the following change of variables,

$$\theta = \phi^R - \phi^L,\ \phi = \phi^R + \phi^L \tag{B.4}$$

The new action in terms of $\phi^R,\ \phi^L$ takes the form,

$$\begin{aligned} S &= \sum_i^{R,L} \int dxdt \Big[-\phi^i(\gamma_i \partial_x \partial_t - v\partial_x^2)\phi^i - v\kappa^2 a_1^2 \\ &+ 2\kappa \phi_x^i(\tilde{a}_0 - \gamma_i v \tilde{a}_1)\Big] \end{aligned} \tag{B.5}$$

Now we aim to perform a gauge transformation on the action in Eq. (B.5). In order to do this we use the parametrization introduced in .

$$\tilde{a}_0 = \dot{\alpha} - v\beta_x,\ \tilde{a}_1 = \alpha_x - \frac{1}{v}\dot{\beta} \tag{B.6}$$

We now write the action in terms of these new parameters,

$$\begin{aligned} S &= \sum_i^{R,L} \int dxdt \Big[-\phi^i(\gamma_i \partial_x \partial_t - v\partial_x^2)\phi^i \\ &- 2\gamma_i \kappa \phi^i(\gamma_i \partial_x \partial_t - v\partial_x^2)(\alpha + \gamma_i \beta) - v\kappa^2(\alpha_x - \frac{1}{v}\dot{\beta})^2\Big] \end{aligned} \tag{B.7}$$

In the action given in B.7 we make the following shift,

$$\phi^i = \phi^i - \gamma_i \kappa(\alpha + \gamma_i \beta) \tag{B.8}$$

We obtain the new action as,

$$S = \sum_i^{R,L} \int dxdt \Big[-\phi^i(\gamma_i \partial_x \partial_t - v\partial_x^2)\phi^i + \kappa^2 \beta \Box \beta \Big], \tag{B.9}$$

where we define the D' Alembertian operator as $\Box = \frac{1}{v}\partial_t^2 - v\partial_t^2$. The last term in the action can be identified as the term coming from the chiral anomaly between the two edges. Following the calculations in the previous section we

can obtain the expression for β in the gauge $\tilde{a}_0 = 0$ and $\partial_t \tilde{a}_1 = E(x,t)$:

$$S = \sum_i^{R,L} \int dx dt \Big[-\phi^i (\gamma_i \partial_x \partial_t - v\partial_x^2)\phi^i + v\kappa^2 \frac{(\partial_t \tilde{a}_1)^2}{\Box} \Big] \qquad \text{(B.10)}$$

Now we can calculate the current between the edges and along the edges for the interferometer model. Following a similar procedure as in Sec. (4.2.1) we get the same result for the current between the edges through point contact. Notice that we get different result for current along the edge. Current at any point on the ith edge is given by,

$$\begin{aligned} I^i(x,t) &= \frac{\delta S[\phi_1, \phi_2, a_1, a_2, \tilde{a}_1]}{\delta \tilde{a}_1} \\ &= \frac{v_i\ \nu_i}{2\pi} \int_{-\infty}^{0} dt' [E^i(x + \gamma_i v_i t', t) + E^i(x - \gamma_i v_i t', t)] \\ &+ \sum_j \theta(\gamma_i (x - x_j)) I_j(t) \end{aligned} \qquad \text{(B.11)}$$

Hence we see that the current at any point on the edge depends on response due both the chiral components. This was expected since we did not completely decouple the two edges and they are connected together by the anomaly term.

B.2 Integrals Involved in the Calculation of the Current

In this Appendix we solve the integral in Eq. (B.12).

$$f_V(\xi^1, \xi^2, \kappa_{12}) = (\pi T)^{\frac{2}{\nu}} P.V. \int_{-\infty}^{\infty} \frac{e^{i(Vt + \kappa_{21})} \sin\left[\frac{\pi}{2}\left(\frac{sgn(\xi^1 - t)}{\nu_1} + \frac{sgn(\xi^2 - t)}{\nu_2}\right)\right]}{[\sinh(\pi T|\xi^1 - t|)]^{\frac{1}{\nu_1}} [\sinh(\pi T|\xi^2 - t|)]^{\frac{1}{\nu_2}}} \qquad \text{(B.12)}$$

Note that the principal value in front of the integral is taken into account using by analytically continuing the filling factors to complex plane. The integrals correspond to Beta functions and their generalizations defined on a complex contour [148]. We split the interval of integration in three parts.

$$
\begin{aligned}
f_V &= f_1 + f_2 + f_3 \\
f &= \left\{ \Big[\int_{-\infty}^{\xi^1} dt - \int_{\xi^2}^{\infty} dt \Big] \sin\Big(\frac{\pi 1}{\nu}\Big) + \int_{\xi^1}^{\xi^2} dt \sin\Big(\frac{\pi\lambda_-^2}{2}\Big) \right\} \\
&\times \frac{(\pi T)^{\frac{2}{\nu}} \sin(Vt - \kappa)}{[\sinh(\pi T|\xi^1 - t|)]^{\frac{1}{\nu_1}} [\sinh(\pi T|\xi^2 - t|)]^{\frac{1}{\nu_2}}}
\end{aligned} \tag{B.13}
$$

Here we have defined parameter $\lambda_- = \sqrt{\frac{\nu_1 - \nu_2}{\nu_1 \nu_2}}$. Consider the first integral (call it f_1) in the above expression. We make the shift $t = \xi^1 - t$.

$$
f_1 = Im\Bigg\{ \int_0^{\infty} dt \frac{e^{i(V\xi^1 - \kappa)} e^{-iVt} (\pi T)^{\frac{2}{\nu}} \sin\Big(\frac{\pi}{\nu}\Big)}{[\sinh(\pi T t)]^{\frac{1}{\nu_1}} [\sinh(\pi T|t + \xi^2 - \xi^1|)]^{\frac{1}{\nu_2}}} \Bigg\} \tag{B.14}
$$

We make the transformation $s = e^{-2\pi T t}$ and $z = e^{-2\pi T|\xi^2 - \xi^1|}$ in the above integral. The resulting expression can be written as

$$
f_1 = (2\pi T)^{\frac{2}{\nu}-1} \sin\Big(\frac{\pi}{\nu}\Big) z^{1/\nu_2} Im\Bigg\{ \int_0^1 du \frac{e^{i(V\xi^1 - \kappa)} u^{\frac{1}{\nu} + \frac{iV}{2\pi T} - 1}}{[1-u]^{\frac{1}{\nu_1}} [1 - zu]^{\frac{1}{\nu_2}}} \Bigg\} \tag{B.15}
$$

using the definition of Hypergeometric functions, we can write,

$$
\begin{aligned}
f_1 &= (2\pi T)^{\frac{2}{\nu}-1} z^{\frac{1}{2\nu_2}} Im\Big\{ e^{i(V\xi^1 - \kappa)} \frac{\Gamma(\frac{1}{\nu} + \frac{iV}{2\pi T})}{2\Gamma(1 - \frac{\lambda_-^2}{2} + \frac{iV}{2\pi T})\Gamma(\frac{1}{\nu_1})} \\
&\times 2F1(\frac{1}{\nu} + \frac{iV}{2\pi T}, \frac{1}{\nu_2}, 1 - \frac{\lambda_-^2}{2} + \frac{iV}{2\pi T}; z)\Big\} \qquad \text{(B.16)} \\
& \qquad \text{(B.17)}
\end{aligned}
$$

Similarly, the second term in the integral (f_2) can be written as

$$
f_2 = (2\pi T)^{\frac{2}{\nu}-1} \sin\Big(\frac{\pi}{\nu}\Big) z^{1/\nu_1} Im\Bigg\{ \int_0^1 du \frac{e^{-i(V\xi^2 - \kappa)} u^{\frac{1}{\nu} + \frac{iV}{2\pi T} - 1}}{[1-u]^{\frac{1}{\nu_2}} [1 - zu]^{\frac{1}{\nu_1}}} \Bigg\} \tag{B.18}
$$

$$
\begin{aligned}
f_2 &= (2\pi T)^{\frac{2}{\nu}-1} z^{\frac{1}{2\nu_1}} Im\Big\{ e^{-i(V\xi^2-\kappa)} \frac{\Gamma(\frac{1}{\nu}+\frac{iV}{2\pi T})}{2\Gamma(1+\frac{\lambda_-^2}{2}+\frac{iV}{2\pi T})\Gamma(\frac{1}{\nu_2})} \\
&\times \; 2F1(\frac{1}{\nu}+\frac{iV}{2\pi T}, \frac{1}{\nu_2}, 1+\frac{\lambda_-^2}{2}+\frac{iV}{2\pi T}; z)\Big\}
\end{aligned}
\tag{B.19}
$$

The third term in the integral can be written as,

$$
f_3 = -Im\left\{ \int_0^{\xi^1-\xi^2} dt \frac{e^{i(V\xi^1-\kappa)} e^{-iVt} (\pi T)^{\frac{2}{\nu}} \sin\left(\frac{\pi\lambda_-^2}{2}\right)}{[\sinh(\pi T t)]^{\frac{1}{\nu_1}} [\sinh(\pi T|t+\xi^2-\xi^1|)]^{\frac{1}{\nu_2}}} \right\}
$$

We make the following transformation to integral f_3, $u = \frac{e^{2\pi T t}-1}{e^{2\pi T|\xi^2-\xi^2|}-1}$, to obtain

$$
\begin{aligned}
f_3 &= -Im\Bigg\{ \frac{e^{i(V\xi^1-\kappa)} (2\pi T)^{\frac{2}{\nu}-1} e^{\pi\frac{T}{\nu_2}|\xi^2-\xi^1|}}{(e^{\pi\frac{T}{\nu_2}|\xi^2-\xi^1|}-1)^{\frac{2}{\nu}-1}} \\
&\times \; \widetilde{F_1}(1-\frac{1}{\nu_1}; \frac{1}{2\nu_2}; 1-\frac{1}{\nu}+\frac{iV}{2\pi}T; 2-\frac{2}{\nu}-\frac{1}{\nu_2}; 1; 1-e^{\pi T|\xi^2-\xi^1|})\Bigg\}
\end{aligned}
\tag{B.20}
$$